

https://dspace.org/

Optical characterization of ion implanted carbon thin films for energy application

Ismaila, Abdulsalam

2020
https://hdl.handle.net/10539/31997

Downloaded from a DSpace repository. https://dspace.org/

Optical Characterization of Ion Implanted Carbon Thin Films for Energy Application

By

Abdulsalam Ismaila

A thesis submitted to the Faculty of Science, University of the Witwatersrand, Johannesburg, in fulfillment of the requirements for the degree of Doctor of Philosophy

Johannesburg, April, 2020

DECLARATION

I declare that this thesis is my own unaided work. It is being submitted for the Degree of Doctor of Philosophy to the University of the Witwatersrand, Johannesburg. It has not been submitted before for any degree or examination to any other University.



……..
(Signature of Candidate)

14th day of April, 2020.

ABSTRACT

This work involves the preparation of amorphous carbon-based active nanocomposites with good antireflectance property, ability to support the generation of charge carriers and potentials for intermediate band application. Amorphous carbon thin films (~ 500 nm thickness) were purchased from YISSUM Research Development Company, Hebrew University Jerusalem, Israel and implanted with 25 keV silver (Ag) ions at varying fluence ranging from 2.5-3.4 x 10^{16} ions/cm^2 using accelerator-based ion implantation. The Ag:a-C nanocomposites were characterized for microstructural and morphological properties via Raman spectroscopy, scanning electron microscopy (SEM), transmission electron microscopy (TEM), atomic force microscopy (AFM) and energy dispersive x-ray spectroscopy (EDS). All samples exhibit Raman fingerprints typical of carbon with G- and D-peaks shifts, broadening as well as intensity variations that were found to depend on the fluence of irradiation. A relative increase in structural disorder, sp^2 cluster aggregation and cluster size attenuation were recorded due to increasing fluence of irradiation. SEM analysis revealed agglomerated Ag particles in sphere-like shapes with average particle diameters in the range ~ 5 nm to ~ 20 nm respectively. TEM micrographs depicted many silver-rich micro grains in the non-reactive phase of the Ag:a-C nanocomposites for all samples and emerging silver oxide (AgO) phase at higher fluence due to tarnishing. AFM analysis shows grain size increase from ~ 5 nm to ~ 21 nm with surface roughness of 1.76 nm for pristine film to 4.92 nm for highest irradiation fluence. EDS spectroscopy confirmed a dominant carbon phase and high oxygen presence largely due to oxides of silicon and silver from supporting substrate and surface tarnishing. Optical characterization, via UV-Visible spectrophotometry, revealed a clear surface plasmon resonance peak (SPR) of Ag nanoparticles at ~ 428 nm with blue shifting in the range ~ 418 nm to ~ 396 nm for irradiated samples. Optical band gap energies, $\boldsymbol{E_g}$ decreases from 1.71 eV to 1.41 eV while Urbach energy, $\boldsymbol{E_u}$ increases from 9.70 eV to 12.00 eV. Other essential optical parameters such as refractive index ($\boldsymbol{n}$), static refractive index ($\boldsymbol{n_0}$), extinction coefficient ($\boldsymbol{k}$), dispersion energy ($\boldsymbol{E_d}$) and oscillator energy ($\boldsymbol{E_o}$) were all found to vary with fluence and in favour of the material potentials. To explore energy potentials, respective nanocomposites were directly incorporated (in series), as surface coatings, in a silicon-based solar cell with reference output parameters ($\boldsymbol{I_{SC}}$ = 5 mA,

$\boldsymbol{V_{OC}}$ = 0.51 V and efficiency, ɳ = 15.11) revealed interesting photovoltaic potentials by improving short-circuit current, $\boldsymbol{I_{SC}}$ from 1.90 mA to 3.00 mA and open-circuit voltage, $\boldsymbol{V_{OC}}$ to as high as 0.576 V. Low efficiencies were recorded but improved appreciably, from 5.68 to 8.97, with increasing fluence of irradiation. As active layers of photovoltaic Schottky barrier devices, respective I-V characteristics of the nanocomposites were found to be ohmic possibly due to mismatch at the interface and the eventual suppressing of silicon layers by the Ag:a-C nanocomposites thereby rendering them passive rather than active. The observed tunable optical band gap, coupled with the plasmonic activities of Ag atoms in the carbon matrix, posed the nanocomposites in great advantages of being used as surface coatings and as functional materials for solar cell efficiency enhancement.

DEDICATION

This work is dedicated to my late father Malam Ismaila Galadima, my mother Khadijah Ismaila Galadima, my wife Zulaihat Muhammad and to my children Ismail Abba, Muhammad Sultan, Fatima Afrah and Abdulsalam Fayyad.

ACKNOWLEDGEMENT

My most sincere thanks to The Almighty for sparing my life and the gift of health and strength to undertake this study.

I would like to, first and foremost, express my profound heartfelt gratitude and appreciation to my able supervisor Professor S.R. Naidoo for his guidance, support and patience throughout the course of the research and the development of this thesis. His concerted efforts and contributions were the secret behind the success of this thesis.

I am also highly indebted to my employers, Ahmadu Bello University, Zaria, Nigeria for funding my studies through the NEEDS Assessment Intervention Funds (2014).

I also owe special appreciation to the University of the Witwatersrand, the School of Physics, Materials Physics Research Institute (MPRI) and the iThemba-LABS (Gauteng) for giving me opportunity to grab a share of excellence of this great citadel of learning. To the following personalities; my supervisor, once again, for supplying/providing all the varieties of carbon samples utilized for this study, Mr. Anthony Miller of iThemba-LABS (Gauteng) for the ion implantation training, Dr. F. Cummings of the electron microscope unit, University of the Western Cape (UWC), Dr. R. Erasmus of the optical spectroscopy laboratories at Wits University for his assistance and training on optical absorption measurements and Raman spectroscopy, Professor D. Wamwangi for his useful discussions and training on sputtering technique of thin film deposition, the entire staff of Wits Microscopy and Microanalysis Unit (MMU). Their expertise and contributions toward the success of this study are highly acknowledged.

Special mention must be made of my colleagues and friends Engr. (Dr.) Nura Jafar Shanono, Dr. Abdu Barde, Dr. Khaled Mohamed, Dr. M. Wilfred, Mr. M. Othmane, Mr. K. Sandile, all Abakwa Youth Association members and the entire Galadima and Gamagira families for their support and encouragement. Lastly, my sincere appreciation goes to my beloved brothers/mentors; Engr. Abdurrahman Samaila and Mohammed Auwal Ibrahim (Yaroson). You will forever remain appreciated.

LIST OF PUBLICATIONS

i. S. R. Naidoo & A. Ismaila: (2019) "Fluence Enhanced Optical Response of Ag Implanted Carbon Thin Films". *Journal of Carbon Research (C)*, 5(45): pp. 1-12. doi:10.3390/c5030045.

ii. A. Ismaila & S. R. Naidoo: "Effect of Irradiation Energy and Fluence on the Optical Absorbance of Silver Implanted Amorphous Carbon Thin Films". South African Institute of Physics (SAIP) held at the Stellenbosch University, Western Cape, South Africa. From 3rd to 8th July, 2017.

iii. A. Ismaila & S. R. Naidoo: (2019) "Ion Implantation of Carbon-based Thin Films: An Overview". Under review.

LIST OF ABBREVIATIONS

a-C	Amorphous carbon
a-C:H	Hydrogenated amorphous carbon
Ag	Silver
NMs	Nanomaterials
NSMs	Nanostructured materials
NPs	Nanoparticles
NCPs	Nanocomposites
CVD	Chemical vapour deposition
MSIBD	Mass selected ion beam deposition
PLD	Pulsed laser deposition
PECVD	Plasma enhanced chemical vapour deposition
SPR	Surface plasmon resonance
UV	Ultraviolet
CNTs	Carbon nanotubes
IUPAC	International Union of Pure and Applied Chemistry
FCVA	Filtered cathodic vacuum arc
DLC	Diamond-like carbon
DLCH	Diamond-like hydrogenated amorphous carbon
PLC	Polymer-like carbon
PLCH	Polymer-like hydrogenated amorphous carbon
ECR	Electron cyclotron resonance
PBS	Plasma beam source
ECWR	Electron cyclotron wave resonance
SRIM	Stopping and Range of Ions in Matter

TRIM	Transport of Ions in Matter
SEM	Scanning electron microscopy
TEM	Transmission electron microscopy
STEM	Scanning Transmission/tunnelling electron microscopy
EDS/EDX	Energy dispersive X-ray spectroscopy
AFM	Atomic force microscopy
TM-AFM	Taping mode atomic force microscopy
MEMS	Microelectromechanical systems
RF	Radio frequency
DC	Direct current
AC	Alternating current
Cu	Copper
Au	Gold
eV	Electron-volt
keV	Kiloelectron-volt
MeV	Megaelectron-volt
GeV	Gigaelectron-volt
MPRI	Material physics research institute
CCC	Charge-coupled device
SAD	Selected area diffraction
CBED	Convergent-beam electron diffraction
EFM	Electric force microscopy
NFOM	Near field optical microscopy
MCA	Multiple channel analyzer
FWHM	Full width at half maximum

ta-C	Tetrahedral amorphous carbon
ta-C:H	Tetrahedral hydrogenated amorphous carbon
ITO	Indium titanium oxide
I_{sc}	Short circuit current
V_{oc}	Open circuit voltage
FF	Fill factor
$\boldsymbol{R_S}$	Series resistance
$\boldsymbol{R_{SH}}$	Shunt resistance

TABLE OF CONTENTS

TITLE PAGE ..... **i**
DECLARATION ..... **ii**
ABSTRACT ..... **iii**
DEDICATION ..... **v**
ACKNOWLEDGEMENT ..... **vi**
LIST OF PUBLICATIONS ..... **vii**
LIST OF ABBREVIATIONS ..... **viii**
TABLE OF CONTENTS ..... **xi**
LIST OF FIGURES ..... **xv**
LIST OF TABLES ..... **xix**
CHAPTER ONE **1**
1.0 INTRODUCTION **1**
1.1 Background of the Study **1**
1.2 Motivation and rationale of the study **2**
1.3 Problem statement **3**
1.4 Research aims and objectives **4**
1.5 Overview of the Thesis **5**
CHAPTER TWO **6**
2.0 Theoretical Background **6**
2.1 Carbon's uniqueness and polymorphism **6**
2.2 Amorphous carbon **8**
2.2.1 Classification of amorphous carbon **9**
2.2.2 Properties of diamond-like amorphous carbon **11**
2.3 Ion implantation **13**
2.3.1 Introduction **13**
2.3.2 Implantation process **15**
2.3.3 Ion stopping and range **16**
2.3.3.1 Range of implanted ions **19**

2.3.4 Ion stopping in amorphous medium 20
2.3.5 Implant energetics 21
2.4 Carbon based thin films 23
2.4.1 Noble metal nanoparticles 24
2.4.2 Surface plasmon resonance 25
2.4.3 Noble metal carbon based nanomaterials 25
2.4.4 Intermediate band prospects 28
2.5 Optical Properties of Solids 28
2.5.1 Interaction of light with matter 29
2.5.2 Optical properties of amorphous carbon 30
2.5.3 Optical band gap 31
2.5.4 Urbach energy 32
2.5.5 Refractive index, n 33
2.6 Application to solar cell photoconductivity enhancement 34
2.6.1 Solar cell current-voltage (I-V) relationship 35
2.6.2 Short-circuit current (ISC) 35
2.6.3 Open-circuit voltage (V_{oc}) 37
2.6.4 Solar cell fill factor (FF) and efficiency (η) 38
2.6.5 Series and shunt resistances of a solar cell 39
CHAPTER THREE 41
3.0 Experimental Techniques 41
3.1 Amorphous carbon film preparation 41
3.2 Ion implantation of carbon films 43
3.2.1 Introduction 43
3.2.2 Silver implantation 46

3.3 Characterization techniques 48
3.3.1 UV-visible spectroscopy 48
3.3.1.1 Instrumentation 51
3.3.2 Raman Spectroscopy 53
3.3.2.1 Principles of Raman 54
3.3.2.2 Theory of the Raman effect 55
3.3.3 Instrumentation 59
3.3.4 Scanning Electron Microscopy 62
3.3.4.1 Basic scanning electron microscopy principle 62
3.3.5 Transmission Electron Microscopy 64
3.3.5.1 Basic TEM microscopy principle 64
3.3.5.2 Instrumentation 66
3.3.5.3 Bright field and dark field images 68
3.3.6 Energy Dispersive X-ray Spectroscopy 69
3.3.6.1 Nomenclature of Characteristic X-rays 70
3.3.6.2 Instrumentation 72
3.3.7 Atomic Force Microscopy 74
3.3.7.1 Instrumentation 75
3.3.8 RF magnetron sputtering 75
3.3.8.1 Instrumentation 76
3.3.8.2 Sputtering of silicon (Si) layers 78
3.3.9 Photovoltaic potentials of Ag:a-C nanocomposites 79
3.3.9.1 Ag:a-C nanocomposites as surface antireflection coatings 79
3.3.9.2 Ag:a-C nanocomposites as base layers for photovoltaic devices 81
CHAPTER FOUR 84
4.0 Results and Discussion 84
4.1 Simulation of ion implantation 84
4.2 Microstructural studies 85
4.3.1 Raman spectroscopy 86

4.2.2 Scanning electron microscopy (SEM) 92
4.2.3 Transmission electron microscopy (TEM) 95
4.2.4 Atomic force microscopy (AFM) 97
4.2.5 Energy dispersive x-ray spectroscopy (EDS) 100
4.3 UV-visible absorption spectroscopy 101
4.3.1 Optical band gap 104
4.3.2 Urbach energy 108
4.3.3 Refractive index 110
4.4 Application of Ag:a-C nanocomposites in photovoltaic devices 113
4.4.1 Ag:a-C nanocomposites as antireflectance coatings 113
4.4.2 Ag:a-C nanocomposites as base layers for photovoltaic devices 116
CHAPTER FIVE 118
5.0 Summary and Conclusions 118
5.1 Summary 118
5.2 Conclusion 120
5.3 Recommendation 120
REFERENCES 121

LIST OF FIGURES

Figure 2.1: Diverse representation of carbon allotropes reprinted from [17]. 7

Figure 2.2: Further representing carbon materials: a) graphite, b) diamond, c) buckminsterfullerene, d) carbon nanotube, and e) graphene. Reprinted from [2]. 8

Figure 2.3: The sp^3, sp^2, and sp^1 hybridized bonding, adapted according to [54] with the open and shaded loops denoting strong and weak bonds respectively. 8

Figure 2.4: Ternary phase diagram of amorphous carbon with vertices corresponding to; diamond-like (sp^3), graphitic (sp^2) and hydrocarbons (H) [77]. 12

Figure 2.5: A schematic view of model 350D serial ion implanter, similar to the 200-20A2F implanter used in this work, with no automated wafer feed-through [5]. 15

Figure 2.6: Dependency of the nuclear and electronic stopping powers on the on the projectile energy, E [6]. 19

Figure 2.7: (a) SEM image of pristine a-C film deposited at 200 ^{0}C on silicon substrate as adopted from [130]; and (b) TEM micrograph of 25 keV Ag implanted a-C at 1 x 10^{16} ion/cm^2 fluence as adopted from [131]. 22

Figure 2.8: Schematic representation of the electronic band structure of amorphous carbon as adopted from [9]. 31

Figure 2.9: I-V curve of a solar cell showing the short-circuit current, I_{SC} [10]. 36

Figure 2.10: I-V curve of a solar cell showing the open-circuit voltage, V_{oc} [10]. 37

Figure 2.11: Schematic of series and shunt resistances in a solar cell [25]. 39

Figure 3.1: Carbon thin film floating set up. 42

Figure 3.2: Mounting carbon film on metal sheet or other substrates; (a) direct mounting and (b) trapped film mounting. 43

Figure 3.3: Front view of the modified 200-20A2F Varian ion implanter. 45

Figure 3.4: Modified 200-20A2F Varian/Extrion ion implanter sputter source. 45

Figure 3.5: Schematic representation of implantation stages for the various fluence. 47

Figure 3.6: The electromagnetic spectrum, [11]. 49

Figure 3.7: A schematic diagram of a typical ultraviolet/visible spectrophotometer [12]. 52

Figure 3.8: Diatomic molecule as a mass on a spring. 55

Figure 3.9: Jablonski representation of Rayleigh and Raman scatterings, adopted from [208]. 59

Figure 3.10: Schematic diagram of the Raman Spectrograph showing beam trajectory from [13]. 60

Figure 3.11: Schematic diagram of a typical scanning electron microscope [208]. 63

Figure 3.12: Block diagram of a Transmission Electron Microscope [217]. 67

Figure 3.13: Typical TEM images of a tissue paper sample in (a) bright filed mode and (b) in dark field mode [14]. 68

Figure 3.14: Mechanism for X-ray generation [15]. 70

Figure 3.15: Nomenclature procedure for characteristic X-rays classification [225]. 71

Figure 3.16: Schematic representation of an energy dispersive X-ray spectrometer [214]. 73

Figure 3.17: Schematic diagram of an atomic force microscope, from [200]. 74

Figure 3.18: Schematic diagram of a typical magnetron sputtering system [16]. 77

Figure 3.19: Experimental set up for the RF magnetron sputtering. 78

Figure 3.20: Schematic diagram of the Ag:a-C/solar cell system. 80

Figure 3.21: Experimental set up for the photoconductivity measurement. 80

Figure 3.22: TRIM simulation of depth profile and damage distribution for the 6 keV phosphorous ions in a silicon layer. 82

Figure 3.23: Schematic diagram of the Ag-a-C photovoltaic device with the nanocomposite as base (active) layer. 83

Figure 4.1: Typical SRIM-2008 simulation of depth profile for 25 keV silver ions in a carbon target layer. 85

Figure 4.2: Raman fit for the pristine a-C film showing D and G peaks. 87

Figure 4.3: Raman fits for lower fluence Ag:a-C nanocomposites (i.e. C1-C4) showing gradual variations in the D and G peaks' positions, intensities and widths with increasing fluence of Ag nanoparticles. 88

Figure 4.4: Raman fits for higher fluence Ag:a-C nanocomposites (i.e. films containing 3.2 and 3.4 x 10^{16} ions/cm^2 of Ag nanoparticles) showing similar variations with the lower fluence sample but with emerging AgO and SiO_2 phases due to Ag tarnishing and supporting glass substrate respectively. 89

Figure 4.5: SEM image of pristine a-C thin film on glass substrate. 93

Figure 4.6: SEM images of a-C thin films irradiated with 25 keV Ag with 2.5 to 3.4 × 10^{16} ions/cm^2 fluences. 94

Figure 4.7: Bright mode TEM micrographs of Ag:a-C thin films with varying fluence (2.5 x 10^{16} ions/cm^2 to 3.4 x 10^{16} ions/cm^2) for samples C1 to C6. 96

Figure 4.8: 2D AFM image of pristine a-C thin film. 97

Figure 4.9: 2D AFM image of 25 keV ion irradiated a-C thin films with varying fluence. 98

Figure 4.10: Surface roughness for pristine and Ag irradiated a-C thin films. 99

Figure 4.11: EDS spectra for Ag:a-C nanocomposite at a fluence of 3.4 x 10^{16} ions/cm^2 (C6). 100

Figure 4.12: Optical absorption spectrum of stand-alone pristine a-C film. 101

Figure 4.13: Optical absorption of Ag nanoparticles on glass substrate. 102

Figure 4.14: Optical absorption spectra of Ag:a-C nanocomposites. 102

Figure 4.15: Fluence dependence of the SPR peak shifting. 104

Figure 4.16: Tauc's plot of $(\alpha h\upsilon)^{\frac{1}{2}}$ as a function of photon (hυ) energy for pristine a-C film. 105

Figure 4.17: Tauc's plot of $(\alpha h\upsilon)^{\frac{1}{2}}$ as function of photon (hυ) energy for the various Ag implanted a-C nanomaterials. 106

Figure 4.18: Variation of optical band gap energy with fluence. 108

Figure 4.19: Graph of ln α as a function of photon energy for pristine a-C film. 109

Figure 4.20: Combined graph of ln α as a function of photon energy for the Ag:a-C nanocomposites. 109

Figure 4.21: Dependence of Urbach parameter on fluence. 110

Figure 4.22: Variation of refractive index (n) with fluence. 111

Figure 4.23: Plot of $(n^2-1)^{-1}$ versus E^2 used in estimating the dispersion and oscillator energies. 112

Figure 4.24: Combined I-V characteristic of Ag-a-C/solar cell systems with the nanocomposites as surface coatings. 114

Figure 4.25: Fluence dependence of photocurrent on the combined (series arrangement) of Ag:a-C/solar cell systems. 115

Figure 4.26: Combined I-V relationship for the fabricated devices with the nanocomposites C1, C2, C3 and C5 as base active layers. 117

LIST OF TABLES

Table 2.1: Comparison of the major properties for the different forms of amorphous carbon with those of some reference materials as adapted from [3]. 13

Table 3.1: Irradiation steps for the relevant fluence requirements. 48

Table 4.1: Summary of some structural fingerprints of pristine and Ag irradiated amorphous carbon films extracted from Raman spectra. 91

Table 4.2: Summary of particle dimensions as determined from SEM and AFM analyses. 99

Table 4.3: Variation of SPR peak values with irradiation fluence. 104

Table 4.4: Optical parameters of Ag irradiated amorphous carbon films. 113

Table 4.5: Summary of combined systems' parameters (series arrangement). 115

Table 4.6: Summary of parameters for the Ag:a-C based devices. 117

CHAPTER ONE

1.0 INTRODUCTION

1.1 Background of the Study

It is over half a century now that Richard Feynman enthusiastically addressed the fact that *there is plenty of room at the bottom* [1], a lecture that heralded an entirely new interesting field of physics. Remarkable progress followed this revolutionary talk leading to numerous scientific discoveries in a new field that was later, in the 1970's, termed as *nanotechnology* [2]. Subsequent advancements in the new field had opened up new frontiers in materials science and engineering which paved ways for in-depth approaches to materials research and appreciation with the view of addressing, to a larger degree, the global technological challenges such as those of energy; amongst others. This is evident, according to Dai et al. [3], by the creation of new materials, often referred to as nanostructured materials (NSMs), for efficient energy conversion and storage. A significant aspect of our modern society relies largely on such technologies from carbon nanostructured materials for continued energy supply which, over the past several decades, has seen significant progress in the harvesting of an alternative but clean and sustainable energy, including that from solar cells [4]. However, the adequate utilization of solar energy offers a great challenge in materials research. Although there was tremendous success in attaining theoretical efficiencies as high as 63.2% in the so-called intermediate band photovoltaic devices; compared to the maximum of 40.7% in the single band gap silicon cells, practical realization of the theoretical high efficiency is faced with challenges of producing high density quantum dots with homogeneous shapes and sizes as well as a perfect system without defects [5]. Furthermore, apart from high material cost, the intermittent nature of the energy source (the sun) also made it difficult for a modest and aspired conversion efficiency which, according to the Stanford University Global Climate and Energy Project [6], make them poorly competitive in a large scale energy market already dominated by fossil fuels.

Adequate development of new technologies with higher conversion efficiencies and low production costs is a key scientific/technical as well as economic requirement for enabling the deployment of solar energy at larger scales. It is in view of the above requirement that energy production and storage become critical research endeavors. According to Cott et al. [7], carbon-based nanostructured materials in the form of thin

films with high surface area, resistance to oxidation and high electrical conductivity are interesting candidates for a host of future energy storage and technological applications. The interest in these materials is due largely to the unique and favorable properties they demonstrated which, by and large, depend upon certain distinct microstructural attributes as; fine grain size/size distribution (<100 nm), chemical composition of the constituent phase, presence of interfaces, and interaction between the constituent domains [8].

1.2 Motivation and rationale of the study

The uniqueness and abundance of carbon enabled its diverse significant roles in the advancement of nanostructured materials. It is so unique that it can, by simply changing its bonding, exist in different forms such as graphite, diamond, fullerene, carbon nanotube, graphene and amorphous carbon (a-C) [9]. Of the various forms of carbon, amorphous carbon stood outstanding and found wide range of applications due to its extreme but favorable properties like high hardness, high electrical resistivity, high thermal conductivity, high dielectric strength and infrared transparency [10]. These interesting properties made carbon a suitable research candidate in creating new materials with adequate size/surface-dependent (e.g. morphological, electrical, optical, and mechanical) properties useful for a cadre of applications and in enhancing energy-conversion and storage performances [3]. Furthermore, amorphous carbon exhibits optical band gap values (0.2-3.0 eV), in between the two extremes for insulating diamond (~5.5 eV) and metallic graphite (~0.0 eV) [11] which placed it in a good position for optical characterization. The light absorption rate due to its amorphous nature (higher, compared to crystalline structures), also gives it an edge over other materials as a suitable alternative for application in conventional solar cells for efficiency enhancement [12].

In the last few decades, research in carbon and carbon related materials has focused on optimization of applications through combining carbon or its related materials with other elements or particles of other elements as inclusions, both in micro and nanoscales, in order to achieve certain improved properties [13, 14]. Of particular interest in this context are the metal-containing carbon nanomaterials. These materials, mostly in the form of thin films, had been extensively studied for prospective engineering, electronics, optics and other applications in energy-related fields. Of the variety of metallic nanoparticles used in doping carbon films, silver (Ag) attracts

specific interest of researchers as it does not form carbide but revealed a remarkable increase in the overall film hardness as well as a decrease in the film optical transparency which consequently caused a decrease in the optical band gap of the resulting nanomaterial [15].

It is pertinent to state here that, deposition of quality carbon films with appropriate required physical and chemical characteristics, determines the suitability of carbon-based nanostructured materials for either laboratory or large scale industrial applications. Different techniques were employed for the deposition of carbon based materials including the first laboratory preparation of diamond-like amorphous carbon film using ion beam deposition by Aisenberg & Chabot [16] in 1971. Several other deposition techniques like; mass selected ion beam-MSIB [17, 18], sputtering [19, 20], cathodic arc [21, 22], pulse laser deposition-PLD [23-26], and the popular plasma enhanced chemical vapour deposition-PECVD [27-34] were later developed and applied for various applications.

The above mentioned chemical methods had encountered severe drawbacks especially when doping of metal nanoparticles is required at deposition stages. Some of these limitations include attaining certain experimental conditions, fabrication challenges inhibiting the use of heat at manufacturing stages, and the inability to employ certain desirable coatings either due to high temperature requirement or changes in materials dimension by their additional thickness [35]. Although the deposition processes have the advantages of batch fabrication and present no damages to the doped materials [36], accelerator-based ion implantation offers greater advantages of low temperature process, precise dose, junction depth control, implantations through thin layers, implantation of different ions at different depths, and short process times [37, 38].

1.3 Problem statement

Despite the diverse interests in the application of noble metals as inclusions in carbon nanomaterials as well as their versatility in a range of favorable and applicable end results [39], little or no efforts had been made towards tailoring their applications in efficiency enhancement of conventional solar cells even with the challenges identified. To this end, our research envisaged the integration of the various identified favorable properties of metal containing amorphous carbon nanomaterials, and particularly from the optical absorption points of view, into addressing these militating efficiency challenges. The non-reactivity of silver atoms with carbon (non-carbide forming) [30],

their clear-cut surface plasmon resonance (SPR) wavelength within the visible range of the electromagnetic spectrum [40], as well as the antireflectance property of their carbon based nanocomposites [41] motivated the interest for this research.

1.4 Research aims and objectives

It is in the light of addressing such challenges, as those of efficiency in silicon based conventional solar cells that we aimed at coming up with an active material that;

- Can provide good antireflectance property for improved light retention,
- Will support the generation of charge carriers due to enhanced light absorbance, and
- Has potentials for active device applications.

The objectives include amongst others;

- To deposit and/or identify a suitable and floatable amorphous carbon film,
- To establish its pristine optical properties via preliminary investigation,
- To irradiate the a-C film with 25 keV Ag ions at varying fluences via accelerator-based ion implantation,
- To conduct comprehensive microstructural and optical characterizations of the resulting nanocomposites,
- To investigate the efficiency enhancement potentials of respective nanocomposites, as surface coatings, in a reference silicon-based solar cell,
- To explore the Schottky effect of respective nanocomposites, as stand-alone active layers, in metal-semiconductor devices.

The choice of amorphous carbon is critical here due to its remarkable prospect in light absorbance and antireflectance property [42]. Silver on its own constitutes a good candidate for the formation of metal-semiconductor interface for Schottky devices. This work seeks to explore the application of Ag containing nanocomposites in the fabrication of metal-semiconductor Schottky interfaces in relation to their anticipated light retention property. Intermediate band property can be achieved typically by the implantation of metal atoms into the pristine material of interest (amorphous carbon in this case) and avoiding the complexities of quantum confinement effects [43]. In this way, the dopant atoms would modify the electronic energy band structure thereby creating an additional intermediate energy band in the host matrix in addition to its intrinsic bandgap [5, 41, 44-46].

1.5 Overview of the Thesis

Chapter one of the thesis presents the research motivation of the work. Chapter two provides the literature guide as well as the general overview of the theoretical background for the study. Chapter three depicts the experimental details involved; these include a comprehensive description of samples' preparation, the theories and principles of accelerator-based ion implantation, UV-Visible spectrophotometry, Raman spectroscopy, scanning and transmission electron microscopies, atomic force microscopy and energy dispersive x-ray spectroscopy. Chapter four dwells on the analysis discussion of the results obtained from the combined techniques used as well as prospective application(s) of the nanocomposites. Lastly, chapter five summarizes the conclusion and offer recommendations for future works(s).

CHAPTER TWO

2.0 Theoretical Background

2.1 Carbon's uniqueness and polymorphism

Carbon as a unique material generally exist in two main isotopes (^{12}C and ^{13}C) and is, under normal conditions, highly unreactive despite its versatility in compound formation. Among its unique properties are its ability to form long chains with other carbon atoms, form isomers in many different compounds, and to exist in different stand-alone allotropes [47]. The two major allotropes of carbon, diamond and graphite, provided an unusually interesting but distinct features observed in no other materials. This is evident in the fact that while diamond is optically transparent, abrasive, and can be a good electrical insulator and thermal conductor; graphite is conversely opaque, a good lubricating agent as well as a good electrical conductor and a thermal insulator [48]. In addition to the well-known diamond and graphite, the discoveries of buckminsterfullerene C_{60} in 1985 by Kroto and co-workers as well as carbon nanotubes (CNTs) by Ijima in 1991, added to the family of carbon allotropes and opened up an entirely new era in the field of material science and technology [3]. Much later in 2004, the most recent allotrope was discovered. This new material, called graphene, is a single sheet extract of a three-dimensional graphite obtained via micromechanical cleavage technique [49]. Pictorial representations of the diversity of carbon allotropes are shown in Figures 2.1 and 2.2 respectively. Moreover, the ability to exist in three different hybridizations; sp^3, sp^2, and sp^1, makes it possible for carbon to form a large variety of crystalline and amorphous structures. In the sp^3 configuration, just like in diamond, each of the four valence electrons is assigned to an sp^3 orbital which is directed tetrahedrally and hence making a strong σ bond with an adjacent atom [50]. In the sp^2 configuration however, three of the four valence electrons enter trigonally directed sp^2 orbitals thereby forming σ bonds in a plane. The remaining electron lies in a π orbital which lies normal to the σ bonding plane and a weaker π bond is formed by this π orbital with one or more adjacent atoms [51].

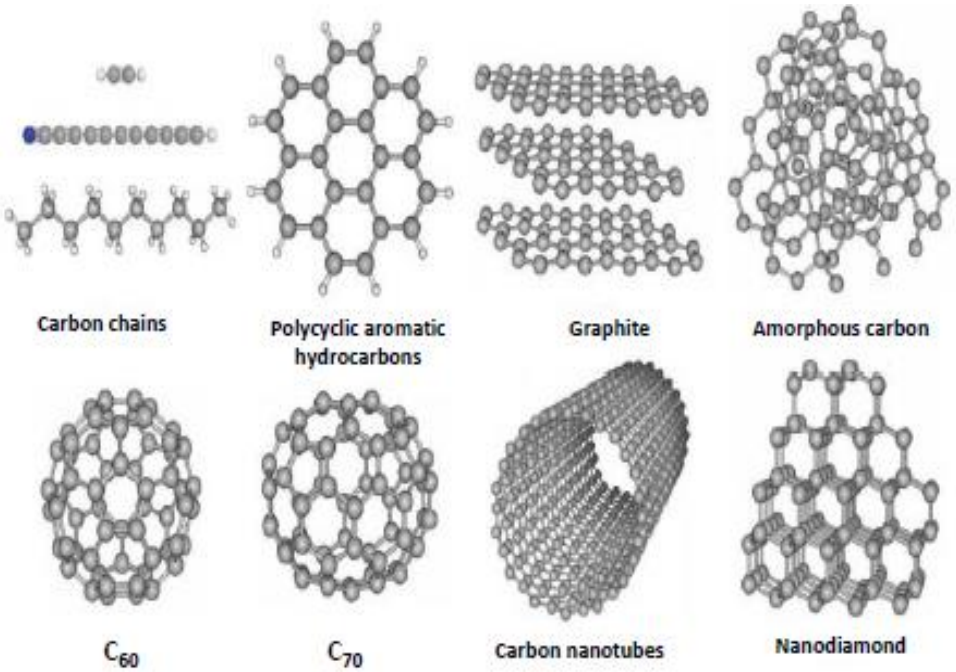


Figure 2.1: Diverse representation of carbon allotropes reprinted from [17].

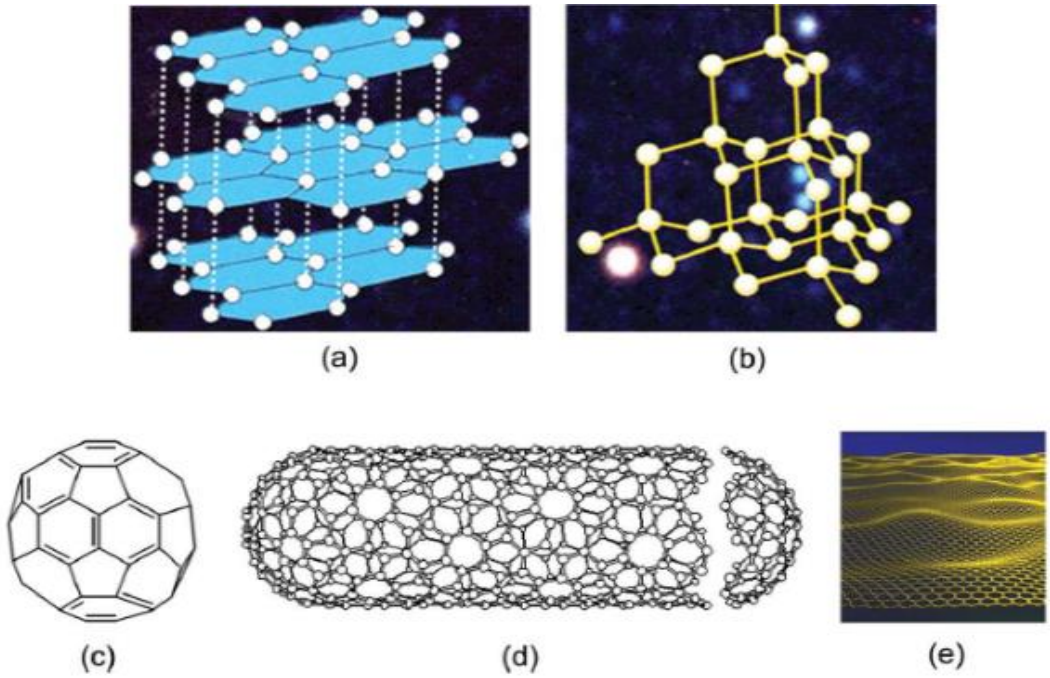


Figure 2.2: Further representing carbon materials: a) graphite, b) diamond, c) buckminsterfullerene, d) carbon nanotube, and e) graphene. Reprinted from [2].

In the last configuration (sp^1), two of the valence electrons enter σ orbital with each forming a σ bond in the ±x-axis while the remaining two valence electrons enter π orbitals in the y and z directions respectively [54], as depicted in Figure 2.3.

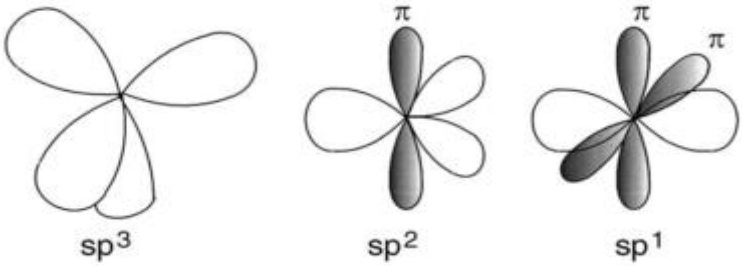


Figure 2.3: The sp^3, sp^2, and sp^1 hybridised bonding, adapted according to [54] with the open and shaded loops denoting strong and weak bonds respectively.

2.2 Amorphous carbon

According to the International Union of Pure and Applied Chemistry (IUPAC), amorphous carbon is a carbon material without long-range crystalline order but with short range order whose interatomic distances as well as interbonding angles deviate from those of graphite and diamond lattices. It can as well be considered as a non-

organized, cross-linked carbon matrix characterized by a mixture of hybridized sp^2 and sp^3 bonds [55]. Although, carbon bonding and hydrogen content are the two parameters that define the short-range order in an amorphous carbon, they do not actually define its entire structure. This is evident from the fact that many amorphous (disordered) form of carbon exhibit structures based on graphite's lattice due to its stable nature as an allotrope of carbon [53]. Adequate understanding of the structure of amorphous carbon is of great importance especially in relation to its closely related alloys such as glassy carbon and hydrogenated amorphous carbon (a-C:H). Furthermore, a major challenge in dealing with amorphous carbon is the understanding of the exact form of the material under consideration from the numerous generic terms/names applied. Because, unlike in the case of carbon nanotubes where there are easy classifying indexes [56], films with entirely different properties are often called or described by the same generic names. The general consensus was that; the glassy form of carbon has approximately 100% sp^2 sites, the regular (evaporated) amorphous carbon (a-C) has 1-10% sp^3 sites, while the hydrogenated amorphous carbon (a-C:H) may contain up to 30-60% hydrogen atoms with perhaps 30% of the carbon sites having an sp^2 configuration depending on heat treatment [57]. In principle, and with respect to the variation in its atomic hybridization, the percentages of the sp^2 and sp^3 hybridization sites as well as hydrogen in a carbon material give an insight on the type of carbon under consideration. Thus, it becomes necessary to adequately identify each member in the amorphous carbon family with respect to its atomic composition and the deposition technique(s) that best produce(s) it. It is pertinent to mention that amorphous carbon films had, over the past three decades, captivated extensive experimental, theoretical, as well as computational interests. A range of application prospects in the electronic, mechanical, chemical and aerospace fields have been studied due to their low friction coefficient, chemical inertness, good wear resistance and high optical transmittance in a wide range from infrared to ultraviolet [58].

2.2.1 Classification of amorphous carbon

Amorphous carbon can be classified into hydrogen free, also known as tetrahedral amorphous carbon (ta-C), and hydrogenated amorphous carbon. The tetrahedral amorphous carbon (ta-C), also called diamond-like carbon, is characterized by the

highest or maximum C-C sp^3 content often greater than 60%. The C-C sp^3 bonds , in addition to controlling the elastic constants of these materials [72], give these films a relatively high strength such that growth techniques involving energetic ions are required for their deposition. Techniques such as filtered cathodic vacuum arc (FCVA), mass selected ion beam deposition (MSIBD), and pulsed laser deposition (PLD) are usually employed in this regard [21, 22, 17, 18, 23, 24, 25, 26].

In the case of the hydrogenated amorphous carbon (a-C:H), four different types had been identified [60] with respect to hydrogen content.

1. a-C:H with 40-60% H content;

This is a soft and low density amorphous carbon film containing up to 70% sp^3 that are mostly H terminated and with a band gap of 2-4 eV [3]. Due to the highest hydrogen content it possesses among other types, it is often referred to as polymer-like hydrogenated amorphous carbon (PLCH) usually deposited using plasma enhanced chemical vapour deposition (PECVD) technique at a controlled and low bias voltage [61, 62].

2. a-C:H with 20-40% H content;

This amorphous carbon has an intermediate hydrogen content as well as a lower sp^3 content but with higher number of C-C sp^3 bonds compared to the (PLCH). These bonds offer it better mechanical properties with a relatively lower optical band gap of 1 to 2 eV [3]. The intermediate nature of both sp^3 and H contents, in addition to high hardness, makes this film to be termed as diamond-like hydrogenated amorphous carbon (DLCH) and usually grown via PECVD, electron cyclotron resonance (ECR), and reactive magnetron sputtering at moderate bias voltages [60, 61, 62, 63, 64, 65].

3. ta-C:H;

These films, called hydrogenated tetrahedral amorphous carbon films, are basically diamond-like amorphous carbon films in which the hydrogen content can be kept constant while increasing the C-C sp^3 bonds. Their high sp^3 content which is about 70% and less hydrogen (25-30%) makes them fall under an entirely different category of amorphous carbon with a higher density up to 2.4 g cm^{-3}, Young's modulus up to 300 GPa [72], [79] and an optical band gap up to 2.4 eV [67]. As a result of these extreme properties, techniques involving high-density plasma sources such as plasma beam

source (PBS) and electron cyclotron wave resonance (ECWR) are used for their deposition [67, 68, 69, 70].

4. a-C:H with less than 20% H content;

These carbon films contain a very low atomic percent (at. %) of hydrogen and are characterized by high sp^2 content and clustering. They are structurally more of graphite and thus referred to as graphite-like hydrogenated amorphous carbon film. Their optical band gap is found to be less than 1 eV and are usually deposited by magnetron sputtering or a high bias plasma enhanced chemical vapour deposition [54, 61, 64].

2.2.2 Properties of diamond-like amorphous carbon

Diamond-like amorphous carbon is a metastable, random networked amorphous phase of carbon which is composed of a mixture of sp^3 and sp^2 hybridized carbon and whose diamond-like character is derived from the C-C sp^3 bonds in its structure. As highlighted in section 2.2.2 above, It could be regarded as hydrogenated or hydrogen free depending on whether it is deposited from a hydrocarbon source or a solid carbon source, e.g. graphite and fullerene, in a vacuum or in the presence of noble gases [54, 71]. And unlike diamond, it can be deposited at ambient temperature [56]. It was originally named diamond-like when Aisenberg & Chabot [16], produced thin films of insulating amorphous carbon, having similar physical and chemical properties as those of diamond, via ion-beam deposition technique on room temperature substrates. Several other related works followed; the most popular of which was the work of Spencer et al. [72] in which similar films were characterized using x-ray and electron beam diffraction techniques and much later, Robertson [73] suggested that the beneficial properties of this disordered carbon are due to the sp^3 component of the bonding and the possession of some extreme properties such as relative hardness, elastic modulus and chemical inertness. Basman et al. [74], added that diamond-like amorphous carbon exhibits high dielectric strength, extended range of band gap, low loss, high resistivity as well as large area growth conditions. Although it contains a mixture of C-C sp^3, C-C sp^2 and C-H bonding components, its mechanical properties are determined by the C-C sp^3 bonds which account for the film's hardness, Young's modulus and general quality. Very little contribution to mechanical properties are offered by the C-C sp^2 while the C-H bonds have no contribution at all as they are just

a collection of dangling bonds not linking the network. The density and Young's modulus of the film are also found to depend largely on the sp^3 fraction in the material [50, 54, 59, 75]. The inter-relation of both hydrogenated and hydrogen free amorphous carbons (C:H alloy or nitrogen-free carbon) films can be conveniently displayed in a ternary phase diagram (Figure 2.4) originally described by Jacob & Möller [76] and adopted from [77].

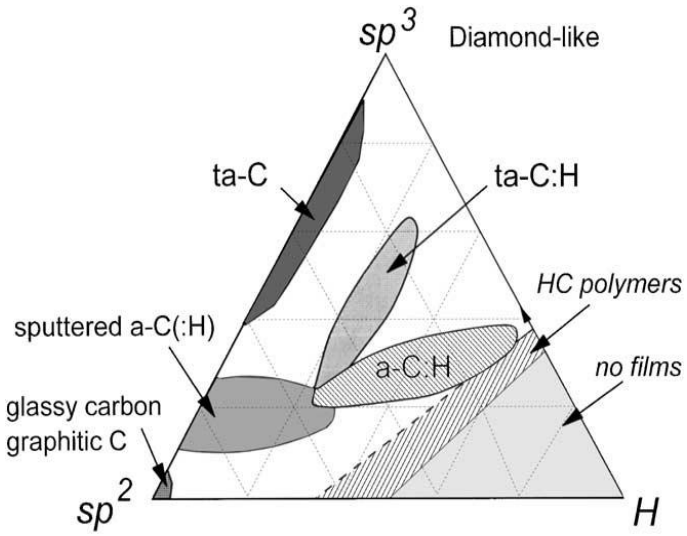


Figure 2.4: Ternary phase diagram of amorphous carbon with vertices corresponding to; diamond-like (sp^3), graphitic (sp^2) and hydrocarbons (H) [77].

Several characterization studies have shown that the microstructural and physical properties of these amorphous carbon materials varied depending on the deposition techniques applied and the film growth conditions [90]. Furthermore, based on the suitability for either laboratory studies or large scale industrial applications, different techniques were employed for their deposition. Since the first laboratory preparation of this material using ion beam deposition by Aisenberg & Chabot [16], several other deposition techniques like; mass selected ion beam-MSIB [17, 18], sputtering [19, 20], cathodic arc [21, 22], pulse laser deposition-PLD [23, 24, 25, 26], and the popular plasma enhanced chemical vapour deposition-PECVD [27, 28, 29, 30, 31, 32, 33, 34], were later developed and applied for the same deposition purposes. It is pertinent to mention also that the single and most important parameter in determining the unique properties of amorphous carbon is the fraction of the tetrahedrally bonded (sp^3) carbon

[79]. Typical distinguishing properties for the different forms of diamond-like carbon can be compared to those of diamond and graphite as shown in Table 2.1.

Table 2.1: Comparison of the major properties for the different forms of amorphous carbon with those of some reference materials as adapted from [3].

Materials	**sp^3 (%)**	**H (%)**	**Density ($g.cm^{-3}$)**	**Gap (eV)**	**Hardness (GPa)**	**Ref.**
Diamond	100	0	3.515	5.5	100	[80]
Graphite	0	0	2.267	0	-	[93]
C_{60}	0	0	-	1.6	-	[94]
Glassy carbon	0	0	1.3-1.55	0.01	3	[95]
Evaporated carbon	0	0	1.9	0.4-0.7	3	[95]
Sputtered carbon	5	0	2.2	0.5	-	[96]
ta-C	80-88	0	3.1	2.5	80	[39]
a-C:H hard	40	30-40	1.6-2.2	1.1-1.7	10-20	[85]
a-C:H soft	60	40-50	1.2-1.6	1.7-4	<10	[97]
ta-C:H	70	30	2.4	2.0-2.5	50	[82]
Polyethylene	100	67	0.92	6	0.01	[86]

The fraction of the tetrahedrally bonded (sp^3) carbon identifies the most important single parameter determining the amorphous carbon property. Using metal nanoparticles as dopants, the microhardness, adhesive strength, chemical stability, and most importantly, the electrical conductivity of amorphous carbon films can be greatly enhanced [87].

2.3 Ion implantation

2.3.1 Introduction

Research activities over the years, since the 1950's, have developed the understanding of the interaction of energetic ions with matter to some large scale applications. These include, for example, the applications of low energy ion beams in materials analysis, semiconductor industry and in materials science and, so far, the progresses made in the

development as well as upgrade of earlier compact ion accelerators have made this possible. The accelerator is a device that produces ions from a source, accelerates them to some certain required energy (whilst transporting them from the source region to the application region), and finally allow them to bombard a target material in a target chamber [100]. The process described above is referred to as ion implantation; a materials engineering process by means of which ions are accelerated in an electrical field and impacted into a target. It is often used, as an alternative to diffusion, to produce a shallow surface region of dopant atoms deposited into a target material [101]. It can as well be seen as an effective technological tool for introducing single impurities into the surface layer of a substrate (target) to a depth of several microns [102]. Although, this process has been used for several years on industrial scale in the semiconductor industry, it has applications in the modification of tribological surface properties of materials. As a surface phenomenon, defects due to bombardments by the energetic ion(s) interact directly with both the host material (matrix) and implant species within the range of the implanted volume and the consequence of this interaction is the eventual changes in the optical, electrical and elastic properties of the implanted volume as a result of atomic configuration stabilization which is a result from the point defects and extended defects resulting from the implantation process. Pertinent to tribology, the implanted ions cause physical changes in the material, leading to a new improved surface property with respect to friction, wear, corrosion and fatigue [91]. And for the fact that ion implantation is not a coating process, only the outermost layer is changed (at low temperatures below 200^0 C) leaving the bulk properties unaltered [92]. With respect to research domain, the emergence of the fundamental breakthrough in the application of ion implantation (especially in crystal silicon for electronics device fabrication) can be linked, with much confidence, to the Japan's dual meetings in the early 1970's; the Kyoto seminar in 1971 and the Osaka conference in 1974 [105] respectively. And in less than a decade, the application of ion implantation ramified through the surface modification of some light metals, carbon, ceramics and polymeric materials. These had been achieved with great successes as Aluminium was effectively implanted with Nitrogen ion for insulation purpose (ion-in-metal) and for fluence dependent increase in stress amongst others [92, 93, 94].

2.3.2 Implantation process

The ion implanter basically produces an energetic beam of ions of particular atomic species and directs the beam so that the ions are evenly implanted (deposited) across the surface of a wafer (substrate/target). It comprises of mainly three major components; the ion source, the beamline and the end station (target chamber). Each of these components carries out specific functions and works simultaneously with other components to actuate the overall goal of the system [107].

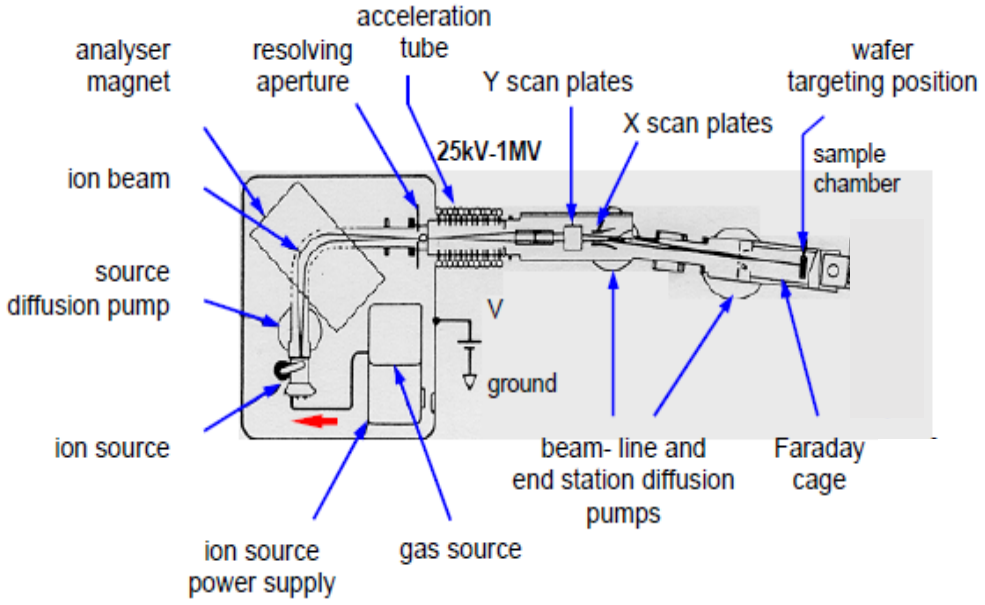


Figure 2.5: A schematic view of model 350D serial ion implanter, similar to the 200-20A2F implanter used in this work, with no automated wafer feed-through [5].

The source utilized a Freeman type ion source for generating the implant ions. Electrons generated (thermionically) from the hot cathode collide with carrier gas molecules (released in the chamber) and cause them to ionize into positively charged ions. The heat from the filament causes dissociation of the gas, for instance a source gas comprising of CO will result in CO^+, C^+ and O^+ ions being created in the arc chamber of the source. The ions are extracted out of the chamber at a sufficiently high energy and are accelerated by a high voltage difference (~ 23 kV) between the source and an extraction electrode. An electron suppression electrode at -2 keV allows a beam of primarily singly charged ions that exit the source at ~ 25 keV. An analyzer magnet that generates a transverse magnetic field is provided for appropriate specie(s) selection

so that constituent ions entering the region of the field are deflected into circular orbits (characteristic of their individual atomic masses). The selected desired ions will be deflected 90^0 through the curvature of the magnetic chamber and be focused by the magnet at the resolving aperture while other ion species in the beam will be deflected at angles below or above 90^0 and are collected on the magnetic chamber walls or the resolving aperture plates. This beam of selected ions enters the acceleration tube at high terminal potential (0-180 kV) providing the ions with their final energy boost before getting implanted.

Upon exiting from the beamline, the ions diverge and a quadrupole doublet lens is mounted immediately to focus the beam into an oval shape spot. Scanning plates raster the ion beam uniformly over a large area and an assembly of four corner Faraday cups are used to check the beam uniformity and the sum of the currents in the corner Faraday cups is used to determine the integration time used to calculate the required fluence. Particles in the beam that have become neutralized by collisions with surfaces, gas molecules, and electrons after the analyzer region, get collected in a beam gate dump in order not to affect the fluence accuracy. The ion beam gets deflected into the implant chamber and ions are implanted into the target at a fluence determined by the measured residual electric current which the ions produced in the Faraday cup assembly. The magnitude of this current is sent to a current integrator which determines the time for the target to be exposed to the ion beam to achieve a preselected fluence. As soon as the required fluence is attained, the beam is automatically deflected away from the implant chamber [5].

2.3.3 Ion stopping and range

The mechanism of energy-loss in ion irradiated materials begins as soon as the ions bombard the target material. Upon penetrating into the host target material, they (ions) collide with the host atoms, lose energy (stopping), and finally come to rest at some depth (range) within the solid target. The Stopping power of a given medium (target) is referred to as the average unit of energy loss per unit path length suffered by the ions in the medium [97, 98, 99]. In addition to atomic collisions, a drag force due to the overlap of electron orbitals also contribute to the stopping [54]. Of significant consideration in this process is the extent to which the bombarding ions penetrate into the host target. This ionic depth of penetration, called the range, is determined by the

nature of both the ions and the target material as well as the acceleration energy of the impinging ions [111]. Because ion implantation is a near-surface phenomenon, the ions penetrate to an average depth of 10 nm to 1 μm depending on their striking energies [112]. And depending on the experimental requirements and accelerator specifications, implantation energies ranging from keV to MeV [113] with fluences from 10^{11} atoms/cm^2 for threshold adjustments to 10^{18} atoms/cm^2 for buried dielectric formation are utilized [114]. Furthermore, as a low-temperature technique, ion implantation offers more flexibility than diffusion [52] and the implants are capable of altering the elemental composition of a material target and consequently the physical and chemical properties [115]. It is pertinent to mention that the implanted species experience a loss of energy which is a determining factor in the final ionic distribution and the subsequent defect(s) they effect to the host target. This energy loss is mainly due to two independent processes; nuclear stopping and electronic stopping [116]. Nuclear stopping is as a result of series of collisions of ions with the host atoms which can be simulated based on elastic collisions between pairs of nuclei while the electronic stopping is due to their inelastic collisions with electrons in the target [106]. The combined rate of energy loss, also called the total or cumulative stopping power (S), is mathematically described according to [118] as:

$$\boldsymbol{S} = \left(-\frac{\boldsymbol{dE}}{\boldsymbol{dx}}\right) \qquad 2.1$$

with a negative sign being a loss of energy and presented by Schöner [105] as follows:

$$\boldsymbol{S} = \left(-\frac{\boldsymbol{dE}}{\boldsymbol{dx}}\right) = \left(\frac{\boldsymbol{dE}}{\boldsymbol{dx}}\right)_{\boldsymbol{n}} + \left(\frac{\boldsymbol{dE}}{\boldsymbol{dx}}\right)_{\boldsymbol{e}} \qquad 2.2$$

where subscripts *n* and *e* represent the nuclear and electronic stopping powers respectively.

Besides this energy loss and the extent of penetration of the ions, a possible damage resulting from scattering effects and often in the form of structural modifications occurs in the lattice structure of the solid target involved [108]. A very popular but

approximate approach to this projectile-target interaction is the assumption that the interaction can be considered as two separate components resulting from ion-nucleus and ion-electron interactions respectively. In view of these acceptable conventions, two dominant mechanisms were adopted in describing the slowing down process of the ions namely electronic energy loss and nuclear energy loss.

And, as highlighted above, stopping power is the general tool for treating the slowing down of energetic ions as they traverse a target [119]. Generally defined as "the energy $\boldsymbol{dE}$ lost by an ion traversing a distance $\boldsymbol{dx}$" [120], stopping power is given by

$$\frac{\boldsymbol{dE}}{\boldsymbol{dx}} = \boldsymbol{N} \int \boldsymbol{T} \boldsymbol{d\sigma} \qquad (2.3)$$

Where; σ is the collision cross section,

T is the energy lost by the ion at the instant of a collision event, and

N is the density of scattering centres of the target.

A very important quantity used in describing the direct dependency of slowing down process on the inelastic collisions of the energetic ions with the target materials, called the stopping cross section ε, is deduced from equation (2.3) as follows

$$\boldsymbol{\varepsilon} = \frac{\mathbf{1}}{\boldsymbol{N}} \frac{\boldsymbol{dE}}{\boldsymbol{dx}} = \int \boldsymbol{T} \boldsymbol{d\sigma} \qquad (2.4)$$

Relating 2.4 and the Schöner's presentation in 2.2, the total stopping cross section can be expressed as

$$\frac{\boldsymbol{dE}}{\boldsymbol{dx}} = \left(\frac{\boldsymbol{dE}}{\boldsymbol{dx}}\right)_{\boldsymbol{e}} + \left(\frac{\boldsymbol{dE}}{\boldsymbol{dx}}\right)_{\boldsymbol{n}} = \boldsymbol{N}(\boldsymbol{\varepsilon_e} + \boldsymbol{\varepsilon_n}) \qquad (2.5)$$

where $\boldsymbol{\varepsilon_e}$ and $\boldsymbol{\varepsilon_n}$ are the electronic and nuclear cross sections respectively.

In order to demonstrate the dependency of both nuclear and electronic stopping powers on the ion (projectile) energy, a special case for the implantation of carbon species (C^+)

into diamond was put forward by Dresselhaus and Kalish [108]. It features three important energy parameters $\boldsymbol{E_2}, \boldsymbol{E_3}$ and $\boldsymbol{E_4}$ (Figure 2.6) representing the energy regions of maximum nuclear stopping power $\left[\left(\frac{\boldsymbol{dE}}{\boldsymbol{dx}}\right)_{\boldsymbol{n}}\right]_{\boldsymbol{max}}$, equal values of stopping power $\left(\frac{\boldsymbol{dE}}{\boldsymbol{dx}}\right)_{\boldsymbol{n}} = \left(\frac{\boldsymbol{dE}}{\boldsymbol{dx}}\right)_{\boldsymbol{e}}$ and maximum electronic stopping power $\left[\left(\frac{\boldsymbol{dE}}{\boldsymbol{dx}}\right)_{\boldsymbol{e}}\right]_{\boldsymbol{max}}$ respectively. Typical energy values for these regions were given, for the aforementioned three special cases, as $\boldsymbol{E_2}$ < 5 keV, $\boldsymbol{E_3}$ ~ 15 keV and $\boldsymbol{E_4}$ ≈ 2 MeV. For a fixed target, such as Carbon, the energy scale for these regions increases with increase in atomic number of the projectile(s) [121].

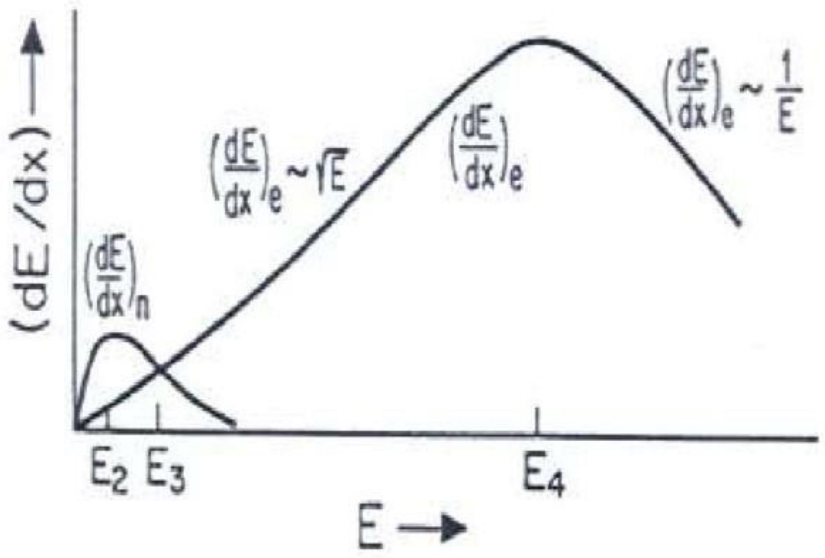


Figure 2.6: Dependency of the nuclear and electronic stopping powers on the on the projectile energy, $\boldsymbol{E}$ [6].

An obvious deduction from this discussion is the fact that nuclear stopping is the dominant energy loss mechanism at low projectile energies while electronic stopping dominates at high energies.

2.3.3.1 Range of implanted ions

The range, as presented by El-Ghossain [118], is not simply the ratio of energy to the stopping power, rather an approximate value determined as follows:

$$\boldsymbol{Range\ (approx.)} = \frac{\mathbf{1}}{\boldsymbol{N'}} . \int_{\mathbf{0}}^{\boldsymbol{E_0}} \frac{\boldsymbol{dE}}{\boldsymbol{dx}} \qquad (2.6)$$

Where

N' is the density of scattering centres of the host material.

Alternatively, by neglecting energy straggling (which defines the overall statistical fluctuations in energy loss in the course of ionic penetration through the solid) we can estimate the total path length of the ions otherwise known as the maximum range [120]. Since it has already been shown that the incident particles energy is a decreasing function of their depth of penetration $\boldsymbol{x}$ with respect to the solid surface, it follows then that:

$$\frac{\boldsymbol{dE}}{\boldsymbol{dx}} = -\boldsymbol{NS(E)} \qquad (2.7)$$

Integrating 2.7 easily gives the value for the maximum range. Thus

$$\boldsymbol{R} = \int_{\mathbf{0}}^{\boldsymbol{R}} \boldsymbol{dx} = \int_{\boldsymbol{E_0}}^{\mathbf{0}} \boldsymbol{dE} \frac{\boldsymbol{dx}}{\boldsymbol{dE}} \qquad (2.8)$$

Substituting for $\frac{\boldsymbol{dx}}{\boldsymbol{dE}}$ in Equation 2.8 with $\frac{\mathbf{1}}{\boldsymbol{NS(E)}}$, the range becomes

$$\boldsymbol{R} = \int_{\boldsymbol{E_0}}^{\mathbf{0}} \frac{\boldsymbol{dE}}{\boldsymbol{NS(E)}} \qquad (2.9)$$

Equation 2.9 gives the total path length of the energetic ions [121] which is in agreement with the presentation in Equation 2.6 by El-Ghossain [122].

2.3.4 Ion stopping in amorphous medium

In contrast to crystalline solids, where the periodic arrangements of atoms greatly influence the nature of scattering and resulting in the discrete treatment or channelling of the stopping process, statistical approach is employed in describing the slowing down process for an energetic ion traversing an amorphous material. Due to the disordered nature of its atomic arrangement, implanted charged atoms in an amorphous solid are so dispersed such that their rest positions are statistical in nature thereby requiring statistical variables for appropriate mathematical representation [108]. According to Ziegler & Lever [122], the mean track length of a traversing ion bears a direct relation with its range $\boldsymbol{R}$ before coming to rest and that the mean penetration depth of this energetic ion relative to the surface of the solid is given by the projected

range $\boldsymbol{R_p}$. Statistically speaking, a Gaussian approach is used, in this context, not only to give the implant density $\boldsymbol{n(x)}$ but to also describe a relatively simple picture of the implant profile, thus

$$\boldsymbol{n(x)} = \frac{\phi}{\boldsymbol{\sigma_p}\sqrt{\boldsymbol{2\pi}}} \exp\left[\frac{-(\boldsymbol{x}-\boldsymbol{R_p})^2}{\boldsymbol{2\sigma_p}^2}\right] \qquad (2.10)$$

where; *x* is a density parameter measured along the ion beam direction,

ϕ is the ion fluence, and

$\boldsymbol{\sigma_p}$ is the standard deviation in the projected range, R_p.

An upgraded software package concerning the Stopping and Range of Ions in Matter (SRIM) with over 500 different plots along with about 27,000 experimental data points is available for comparative simulations of stopping power and range in various media [123]. It also provides an insight on the range profiles and expected ionic damage to the material due to ion implantation [127] as well as the effect of the material thickness on the mean stopping power [128] among other quantities of interest. The cumulative stopping power, range distribution, damage as well as ionic channelling describe other related quantities associated with the ion implantation process [105, 125, 126]. TRIM simulation of 25 keV Ag ions is presented in section 4.2.

2.3.5 Implant energetics

While penetrating a target material, an energetic ion slows down as it displaces many of the target atoms from their equilibrium positions. This is strongly related to, as captured earlier, the lost energy by the energetic ion along its trajectory within the host material due to nuclear and electronic losses. Although the nuclear loss is associated with lower process energies while electronic loss dominates at higher energies (~ 100 keV/nucleon), the displacement of the implant species strongly depends on the masses of the energetic ions and the target atoms [127]. In the case of implanted ion species that chemically react with the host target, the ions may be captured in substitutional sites and become bonded chemically with the amorphous target. Otherwise, the ions proceed and come to rest at some interstitial positions or continue diffusing through the target lattice where they may get trapped at vacancy clusters [132]. In the implants performed for this study, the implanted Ag ions do not form chemical bonds with the

carbon host atoms. The Ag ions diffuse and coagulate to form nanoparticles which leads to change in the dielectric properties of the carbon host matrix [133]. A scanning electron microscopy (SEM) image and a transmission electron microscopy (TEM) micrograph of pristine (pure) and silver (Ag) implanted amorphous carbon films are depicted in Figure 2.7 below.

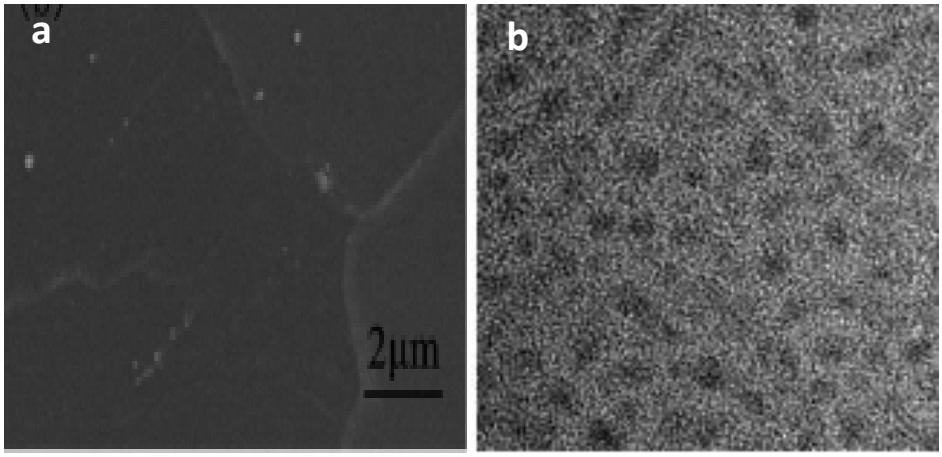


Figure 2.7: (a) SEM image of pristine a-C film deposited at 200 ^{0}C on silicon substrate as adopted from [130]; and (b) TEM micrograph of 25 keV Ag implanted a-C at 1 x 10^{16} ion/cm^{2} fluence as adopted from [131].

As the ion beam strikes the target, part of its energy is dissipated at the target's surface resulting in the ejection of atoms and electrons. This is called sputtering and is been accounted for in terms of yield, that is the number of surface atoms ejected per incident ion [52]. The effect of sputtering on target surface is mostly negligible for most low-temperature ion implantations. For instance, only some 20 monolayers are removed by 10^{16} ions cm^{-2} dose of 200 keV argon ions on silica due to sputtering [134]. According to simple kinematic approach, the projectile (energetic ion) energies before ($\boldsymbol{E_0}$) and after ($\boldsymbol{E_1}$) scattering with the target atoms are linearly related [108] as follows;

$$\boldsymbol{E_1 = kE_0} \qquad (2.11)$$

where $\boldsymbol{k}$ is called the kinematic factor given as

$$\boldsymbol{k = \left(\frac{M_1 \cos\theta \pm (M_1^2 - M_2^2 \sin^2\theta)^{\frac{1}{2}}}{M_1 + M_2} \right)^2} \qquad (2.12)$$

where

- θ is the scattering angle of the projectile in a laboratory frame of reference,
- M_1 is the mass of the energetic ion, and
- M_2 is the mass of the target atom.

The scattering angle, θ is determined form the relation

$$\boldsymbol{\cos\theta = \frac{1 - \left(1 + \frac{M_2}{M_1}\right)\left(\frac{T}{2E_0}\right)}{\sqrt{\left(1 - \frac{T}{E_0}\right)}}} \qquad (2.13)$$

where $\boldsymbol{T}$ is the recoil energy, due to collision, transferred from the projectile to the target and determined from the conservation of energy as

$$\boldsymbol{T = E_0 - E_1} \qquad (2.14)$$

The above relations (2.11-14) generally hold for all elastic scattering processes provided the driving force acts along the line joining the interacting particles.

2.4 Carbon based thin films

Thin films comprise of all solid materials of either a metal, a semiconductor or an insulator, which are technically deposited, by physical or chemical means, onto appropriate substrates at various thicknesses in the range of 10 nm – 1000 nm (or 1 micron) [135]. Film thicknesses beyond the quoted range are regarded as thick films. Ultra-thin films, within 10 nm – 100 nm thickness, which play central roles in modifying characteristics of a material such as the physical, chemical and mechanical properties to entirely different and more favorable ones compared to those of the inherent bulk material thereby paving ways for innovative applications [136]. A variety of good quality and homogeneous thin films of carbon based materials have, in the recent, found wide applications in electronics, optoelectronic devices, optical sensors and surface engineering [137].

Carbon based thin films, particularly those of amorphous carbon (a-C), had been extensively studied due to their unique size-/surface-dependent (e.g., morphological, electrical, optical, and mechanical) properties useful for a variety of research and industrial purposes [3]. They stood outstanding, among other materials, due to their vast applications in carbon nanostructures as well as their remarkable extreme properties like high hardness, high electrical resistivity, high thermal conductivity, high dielectric strength and infrared transparency [10]. Certain metallic species do not form nanoparticles and are categorized as carbide-forming (e.g.; Ti, Mo, Nb, Cr, Zr and W) while those that do not react with carbon (e.g.; Au, Pt, Ag, Ni, and Cu) form nanoparticles in the amorphous carbon film [30]. The metal-containing nanomaterials have, in the past, been prepared and or deposited by means of chemical reactions (depositions). Techniques like dc magnetron sputtering [30], rf reactive sputtering [133], thermal chemical vapour deposition [12, 134], plasma assisted/enhanced chemical vapour deposition [22], thermal co-deposition [135] and pulsed laser deposition [136] were applied and utilized for carbon deposition. Although the deposition processes have the advantages of batch fabrication and present no damages to the doped materials [36], ion implantation offers greater advantages of low temperature process, precise fluence, junction depth control, implantations through thin layers, implantation of different ions at different depths, and short process times [37, 38].

2.4.1 Noble metal nanoparticles

These comprise of ruthenium (Ru), rhodium (Rh), palladium (Pd), silver (Ag), osmium (Os), iridium (Ir), platinum (Pt), gold (Au) and rhenium (Re) [142]. However, there is strict definition in physics as to the actual requirement of noble metals. In this perspective, it is required that the d-band of the electronic band structure of the metal be filled. To this effect, silver and gold are noble metals due to the fact that all d-like bands are completely filled and do not cross the Fermi level [143]. In terms of reactivity, these two metals have demonstrated strong noble nature in such a way that their surfaces are easily cleaned and kept clean for a long period in ultra-high vacuum while surfaces of other metals like platinum and palladium are very quickly covered by carbon monoxide (CO) [139].

2.4.2 Surface plasmon resonance

Advances in lithographic as well as wet chemical techniques have paved way for the successful synthesis/development of a wide range of nanoparticles with varying sizes/geometries and exhibiting varying optical responses. These spectroscopically diverse optical responses are due to a single phenomenon generally referred to as the surface plasmon resonance (SPR), which occurs as a result of collective oscillations of the nanoparticles' conduction band electrons [145]. Although Mie theory, which was first described in 1908, can be used to understand SPR for a sphere, spectroscopic approach as well as advanced electrodynamic numerical methods are necessary in order to correctly describe metal nanoparticles' optical properties [146]. Previous studies have shown that SPR are intimately related to nanoparticle's size, shape, composition, and dielectric environment. In fact, these studies have shown the SPR resonance position (peak position) to be highly tunable across a wide spectroscopic range by only varying the sizes of the nanoparticles [147]. Against this backdrop, significant attention was given to the study of the plasmonic properties of noble metal nanoparticles (e.g. Ag, Au, Cu, etc.) due to their potential uses as components in a diverse range of technologies such as waveguides, photonic circuits, and chemical/biological sensors etc. These applications are exclusively based on the localized surface plasmon resonance of the appropriate nanoparticle [148]. The SPR phenomenon has two key consequences: (1) selective photon absorption and scattering allows the optical properties of the nanoparticles to be monitored by conventional UV-vis spectroscopy and far-field scattering techniques and (2) enhancement of the electromagnetic fields surrounding the nanoparticles lead to surface-enhanced spectroscopic techniques including surface enhanced Raman spectroscopy. The plasmon frequency has been established to be extremely sensitive to nanoparticle composition, size, shape, dielectric environment, and proximity to neighbouring nanoparticles [149].

2.4.3 Noble metal carbon based nanomaterials

Noble metal nanoparticles do not react (do not form carbides) with carbon and their incorporation into carbon-based materials. In the past five decades, innovative applications in cluster deposition for minimizing the influence of surface crystallinity and ion-induced structural changes in the materials have been found [150]. Pure amorphous carbon films are structurally known to exhibit low compressive stress as

well as lower friction coefficients and wear rates [142]. Dimigen & Klages [143] and Jun et al. [144] reported an excellent tribological performance with a favorable combination of considerable hardness, high elasticity, low surface energy and a relatively high wear resistance in metal containing amorphous thin films. Noble metal-containing carbon-based nanomaterials have also been extensively studied and applied as implantable microelectromechanical systems (MEMS) for radio frequency (RF) switches and for the diagnosis of medical conditions [154]. And due to the evident improved antimicrobial efficacy shown, they have been used against *Staphylococcus aureus* and to evaluate the possible eradication of *E. coli* bacteria [147, 148, 149, 150] with a remarkable record in annihilating over 99.9% of variety of strains of bacteria including the methicillin-resistant type [159].

Furthermore, carbon-based nanofilms have attracted a lot of interest in the industrial processing of protective coatings used in medical implants in human bodies. To successfully achieve this, the surface chemistry of the implants needed to be controlled in order to produce a coated surface with favourable biological reaction so as to avoid blood coagulation in patients' bodies, so-called haemocompatibility. To this effect, silver nanoparticles had been used, at a controlled doping ratio, to test the adsorption ratio of protein in form of albumin/fibrinogen [152]. As a measure to contain an obvious drawback of amorphous carbon films, i.e. high compressive stress leading to adhesive and stability problems, metallic nanoparticles such as Ag and Cu had been used in preparing metal containing carbon nanomaterials. To this effect, gold nanoparticles had been successfully applied in biomedical process of plasmon-enhanced photothermal cancer therapy [153].

During the high energy irradiation of amorphous carbon with heavy noble metal ions (e.g. 1 GeV Au ions), conducting ion tracks are formed as a result of the ionic passage [154, 155]. These resulting tracks constitute a collection of extremely small diameter (< 10 nm) of electrically conducting nanowires with the potential for nanoelectronic device applications [164]. By selectively doping thin films of carbon with appropriate noble metal ion species, the conductivity of the ion tracks can be enhanced (at nanoscale) by influencing the atomic arrangement in the track without causing any significant increase in the conductivity of the pristine carbon films. These track

rearrangement of atoms due to dopant ions modifies the sp^3/sp^2 ratio (i.e. increased sp^2-coordinated carbon) leading to increased or higher conductivity [162].

In terms of materials characterization, noble metals nanoparticles have been used for a variety of property modifications including their incorporation into amorphous carbon films with tunable transparency and optical band gap advantages as a result of controlled irradiation with Ag NPs [138] with the possibility of being used in radiation zones as suggested by [9]. In a similar scenario, the spectral analysis of Cu implanted amorphous carbon film via Raman scattering revealed a decrease in the sp^3/sp^2 ratio with increasing atomic concentration in the films and, despite no clear dependence of surface roughness of the amorphous films on the nanoparticle concentration was observed, the collective optical properties (extinction, absorbance and reflectance spectra) of the films were observed to depend on the atomic concentration of Cu as well as on the deposition mode [158]. In addition to optical property modification, these NPs have also been playing key role in the modification of the electrical properties of amorphous carbon nanocomposites. The said Ag irradiated carbon films become plasmonic materials because of the formation of nanoparticles as a result of noble metal irradiation [159]. In the surface modification and property tailoring of amorphous carbon, these nanoparticles have vast applications. Energetic silver ions (15 keV) at varying fluence of 7-10 x 10^{16} ions/cm^2 were used to modify the surface and bulk properties of amorphous diamond-like carbon by independently changing the overall ion beam interaction with the surface and its chemical composition [160]. Menegazzo et al., [161] revealed that gold- and platinum- implanted amorphous carbon nanocomposites are excellent electrode candidates with interesting electrochemical activities that are directly influenced by the noble metal concentration (3-36 at. % in this case).

In another development, noble metals were used in the formation of metal-carbon clusters applicable in the sensitivity control of a surface enhanced Raman scattering technique [162, 165]. It was additionally reported that an induced structural modification of noble metal incorporation in amorphous carbon films results in a considerable change of their surface topography and optical properties [166, 167].

2.4.4 Intermediate band prospects

The intermediate band is designed in such a way that it provides for large generation of photocurrent in a solar cell while maintaining a high output voltage. This is practically achieved by sandwiching the intermediate band material between two ordinary p- and n-type semiconductor materials. In this way, two-way or double transition of absorbed energy photons is initiated. Transition due to sub-bandgap from the valence band to the intermediate band and that from the intermediate band to the conduction band which combines with the conventionally generated photocurrent as a result of valence band-conduction band transition [61]

This Intermediate band property can be realised typically by the ion implantation of metal atoms (especially atoms of noble metals) into the pristine amorphous carbon material and avoiding, in its entirety, the complexities of quantum confinement effects [43]. Attempts to actuate this were made with successes in the implantation of silicon (Si) with titanium (Ti) and that of Zinc Sulphide (ZnS) with Chromium (Cr). In this way, the dopant atoms modify the electronic energy band structure thereby creating an additional intermediate energy band in the host matrix besides its intrinsic bandgap.

Theoretical efficiencies as high as 63.2% were attained in these intermediate band materials as compared to the maximum of 40.7% in the single band gap cells. However, practical realisation of these high efficiency is faced with such challenges as that of producing high density quantum dots with homogeneous shapes and sizes as well as a perfect system without defects [20].

2.5 Optical Properties of Solids

Optical properties of a material can be defined as any property that involves the interaction between electromagnetic radiation or light and the material. These properties include absorption, diffraction, polarization, reflection, refraction, and scattering effects amongst others [166]. In more general terms, it refers to all those techniques that use optical materials to disperse and or focus electromagnetic radiation and whose measurements are only possible if the interaction of photons with the sample leads to a certain change in one or more of the characteristic properties of the radiation such as energy, polarization, frequency [174] etc. The electromagnetic spectrum is an important approach to obtaining an overview of the necessary types of measurements

and physical processes that are characteristic of the particular regions of interest involving the optical properties of the material in question [175]. An evident practice in the determination of optical properties of solid materials is shining a beam of monochromatic light onto an appropriate sample and then measuring the reflectance or transmittance of the sample as a function of photon energy [176].

2.5.1 Interaction of light with matter

There are many different ways in which light interacts with matter. As a general phenomenon and with respect to its interaction with solid materials, two major light interaction processes had been identified. The external or surface interactions involving reflections at both the front and back surfaces (leading to transmission) and internal interactions (propagation) involving refraction and absorption within the material. However, a more appropriate way of quantifying the above optical phenomenon is in terms of a number of certain parameters as reflectivity or coefficient of reflection $\boldsymbol{R}$ and transmissivity or coefficient of transmission $\boldsymbol{T}$ both of which describe surface interaction. Other parameters include absorption coefficient α, which quantifies light absorption by the material and refractive index n, a frequency dependent quantity that relates the velocities of light in free space and in the material [177]. Reflectivity and transmissivity can be defined as the ratios of the reflected or transmitted powers to the incident power relative to the medium [178] and are so complementary in such a way that for a non-absorbing/non-scattering medium,

$$\boldsymbol{R + T = 1} \tag{2.15}$$

The refractive index is also given by the relation

$$\boldsymbol{n = \frac{c}{v}} \tag{2.16}$$

The absorption coefficient is described in terms of the fraction of light power absorbed in a unit length of the medium. Hence for an incident beam of light propagating along the x direction with intensity at any point x given by $I(x)$, then any slight decrease in intensity for a small increase in path length dx can be expressed as;

$$\boldsymbol{dI/I = -\alpha x} \tag{2.17}$$

Integrating Equation 2.17;

$$\boldsymbol{I(x) = I_0 e^{-\propto x}} \qquad (2.18)$$

Equation 2.18 is called the Beer's law, where $\boldsymbol{I_0}$ is the light intensity at *x=0*.

And for a material of certain thickness d (such as thin films) and reflectivities of the front and back surfaces R_1 and R_2 respectively, the transmissivity can be given as;

$$\boldsymbol{T = (1 - R_1) e^{-\propto d} (1 - R_2)} \qquad (2.19)$$

But for a homogenously deposited thin film on plain substrates such as glass, $R_1 \approx R_2$ so that Equation 2.19 reduces to

$$\boldsymbol{T = (1 - R) e^{-\propto d}} \qquad (2.20)$$

Equation 2.20 describes the amount of light that is transmitted through the thin film in relation to a certain amount of incident light on it [179].

2.5.2 Optical properties of amorphous carbon

The optical, and by extension, optoelectronic properties of amorphous carbon films including diamond-like carbon (DLC) and hydrogenated amorphous carbon (a-C:H) films have been shown to depend, not only on their doping or implantation with various elements such as boron, nitrogen silicon, phosphorous and tungsten etc., but largely on the variations of chemical bonding structure [180]. This chemical bonding structure was rarely understood until the development of a detailed structural model by Robertson in 1986 (i.e. the Robertson model) [9] which successfully correlates the said structure with the material physical properties. The bonds in amorphous carbon contain mixtures of sp^2 and sp^3 bonds in contrast to those in amorphous silicon (Si) and germanium (Ge) where the bonds are exclusively sp^3 in nature [181]. To this end, the Robertson model suggested that these sp^2 sites in amorphous carbon form graphitic clusters which are embedded in the sp^3 bonded matrix [9]. Figure 2.8 describes the electronic band structure of an amorphous carbon and showing the occupied and unoccupied π and σ states. According to Robertson and O'Reilly [182], the π bonds of amorphous carbon are much weaker than the σ bonds so that the π states are in close proximity with the Fermi level (E_F) than the σ states. Furthermore, a relatively wide energy gap, ~ 6 eV, separates the valence band (containing filled σ bonding states) and the conduction band (containing empty σ* anti-bonding states). The material band edges are formed by the weaker π bonds of sp^2 sites with filled π bonding states and

empty π* anti-bonding states which are, principally, within the σ - σ* gap and controlling the optical properties of the amorphous carbon [183].

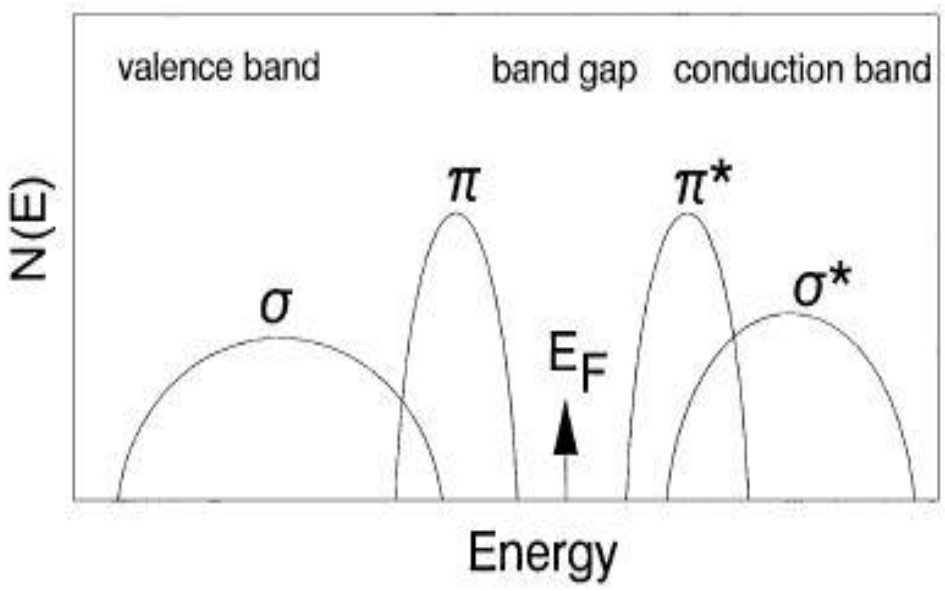


Figure 2.8: Schematic representation of the electronic band structure of amorphous carbon as adopted from [9].

In view of the foregoing discussion, the optical properties of amorphous carbon films are commonly discussed in relation to electronic transitions from the occupied π states to unoccupied π* states (linked to the sp^2 sites) and not the widely separated σ and σ* states (linked to the sp^3 sites). Therefore, the optical band (or Tauc) gap of amorphous carbon is deduced from the separation between these two bands, i.e. $2E_\pi$, such that the larger the average sizes of the sp^2 clusters, the closer these two bands would be and, eventually, the smaller the optical band gap [95]. This implies that the optical band gap of amorphous carbon films is given by the average gap sizes of the sp^2 clusters in it.

2.5.3 Optical band gap

The accurate, or near accurate determination of the optical band gap ($\boldsymbol{E_g}$) is an essential requirement in corroborating the predictions on the applicability and performance of the material under investigation. It is possible, therefore, to critically examine the UV-Visible spectrum in a region within the vicinity of the material's optical energy gap. This region, often referred to as the fundamental absorption edge, is identified from a rapid increase in the magnitude of the absorption coefficient measured as a function of material optical density per unit path length or thickness [184]. Moreover, the

fundamental absorption edge plays a central role in the determination of optical band gap for both direct and indirect interband electronic transitions in the material such the absorption energy, α as a function of photon energy, $\boldsymbol{h\upsilon}$ is given by the Tauc's relation [185] as;

$$\boldsymbol{\alpha = A\frac{(h\upsilon - E_g)^r}{h\upsilon}} \qquad (2.21)$$

So that

$$\boldsymbol{(\alpha h\upsilon)^{\frac{1}{r}} = A(h\upsilon - E_g)} \qquad (2.22)$$

where A is a constant, $\boldsymbol{h\upsilon}$ defines the photon energy in electron-volt (eV), $\boldsymbol{E_g}$ is the optical band gap energy of the material which represents the energy difference between the valence and conduction bands, respectively, while $\boldsymbol{r}$ is an index having values between $\frac{1}{2}$ and 3 depending on the nature of the interband electronic transitions. A plot of $(\boldsymbol{\alpha h\upsilon})^{\frac{1}{r}}$ versus $\boldsymbol{h\upsilon}$ yields a curve whose extrapolation of the linear portion to the $\boldsymbol{h\upsilon}$ axis, at $\boldsymbol{\alpha = 0}$, gives the optical band gap energy.

2.5.4 Urbach energy

One of the standards used as a yardstick in measuring inhomogeneous disorder in amorphous systems is the Urbach energy, $\boldsymbol{E_u}$ [138]. First observed experimentally in 1953 by Franz Urbach [186], the Urbach energy (also called Urbach parameter) describes the tendency of an amorphous system to convert the characteristic weak bonds in its natural disorder into defects, often described as defect density [187]. Due to the prevalence of short order ranges in amorphous systems, the valence and conduction bands are not characterized by sharp optical absorption edges but tails of localized states which are extended in the band gap [188]. Hence, the absorption coefficient is related to the Urbach parameter [186] as follows;

$$\boldsymbol{\alpha = \alpha_0\left(\frac{h\upsilon}{E_U}\right)} \qquad (2.23)$$

where $\boldsymbol{\alpha_0}$ is a constant called band tailing parameter.

Taking the natural logarithm of both sides of Equation 2.22 gives;

$$\boldsymbol{\ln \alpha = \frac{h\upsilon}{E_U} + \ln \alpha_0 = \frac{1}{E_U}h\upsilon + \ln \alpha_0} \qquad (2.24)$$

Equation 2.24 describes a linear relationship between $\ln \alpha$ and the photon energy ($h\nu$) whose slope is given by the inverse of the material's Urbach energy at a particular temperature.

2.5.5 Refractive index, n

For Ag doped amorphous carbon films, the refractive index can be expressed as a function of the optical band gap energy using the Lorentz-Lorentz equation earlier suggested by Duffy [189] and as presented by Dimitrov and Sakka [190]. Thus,

$$\frac{n^2-1}{n^2+2} = 1 - \sqrt{(E_g/20)} \qquad (2.25)$$

Or

$$n = \left(3\sqrt{(20/E_g)} - 2\right)^{\frac{1}{2}} \qquad (2.26)$$

where n is the refractive index and E_g is the optical band gap energy.

The refractive index, n is related to the dispersion of light energy, E_d below the interband absorption edge which is determined using the Wemple-Di domenico (W-D) model [191] as illustrated below.

$$n^2 - 1 = \frac{E_d E_o}{E_d^2 - E^2} \qquad (2.27)$$

where E_d and E_o are the dispersion and oscillator energies, respectively and $E = h\nu$ is the photon energy.

Equation 2.27 is re-expressed linearly as follows;

$$(n^2 - 1)^{-1} = -\frac{1}{E_d E_o}.E^2 + \frac{E_d}{E_o} \qquad (2.28)$$

From the above Equation, the dispersion energy and oscillator energies can both be deduced from the slope ($\frac{1}{E_d E_o}$) and intercept ($\frac{E_d}{E_o}$) on the vertical axis of the straight line portion of $(n^2 - 1)^{-1}$ versus E^2 plot. Furthermore, by letting $E = 0$ in Equation 2.28

above, the static refractive index of the material at zero photon energy, $\boldsymbol{n_{(0)}}$ can be deduced. So that;

$$\boldsymbol{n^2_{(0)} = 1 + \frac{E_d}{E_o}} \qquad (2.29)$$

2.6 Application to solar cell photoconductivity enhancement

The term photoconductivity refers to the incremental change in electrical conductivity of a material as a result of the absorption of optical photons [188]. Investigations into the photoconduction of certain photoactive materials, such as metal containing carbon nanomaterials, have become important diagnostic tools in the search for new materials suitable for electronic devices applications. A lot of research efforts had been put in place to enhance the performance of conventional photovoltaics but faced serious challenges due to limitations offered by the presence of localized electronic states in certain semiconductors. The disordered nature of these materials, their low charge carrier mobilities, as well as the significantly short free-carrier life times when compared to intrinsic crystalline silicon, made it necessary to conduct property modification on semiconducting materials including carbon based nanomaterials [189]. Pertinent to this, we present an approach for tailoring the applications of metal nanoparticles (silver in this case) in electrical properties modification of a covalently bonded material (carbon). This is essential in the sense that the metal inclusions greatly influence the basic processes of adequate photocurrent generation including the generation of free electron-hole pairs due to photon absorption, response to an external electric field for smooth transport of generated charge carriers and material conduction stability due to appropriate reduction in charge carrier recombination [194]. Furthermore, the surface plasmon resonance (SPR) of the metallic nanoparticles, whose strength depends largely on the shape, size and distribution of the particles, can adequately be tailored into improving the photo-activity of optical devices including solar cells [191].

2.6.1 Solar cell current-voltage (I-V) relationship

The solar cell current-voltage relationship is a superposition of the cell's response in the dark with the light generated current, I_L [192] so that the p-n junction diode equation becomes;

$$\boldsymbol{I = I_0\left[e^{\frac{qV}{nkT}} - 1\right] - I_L} \qquad (2.30)$$

where $\boldsymbol{I_0}$ is the reverse saturation current, q is the electronic charge, v is the forward bias voltage, k is the Boltzmann constant, T is the temperature in Kelvin and n is the ideality factor which varies depending on the material.

Equation 2.30 describes the form of the diode equation in the fourth quadrant (reverse operating region where the forward current is negligible), due to light shifting, that enables the extraction of power from the diode. In the first quadrant (forward operating region), however, the equation is presented as;

$$\boldsymbol{I = I_L - I_0\left[e^{\frac{qV}{nkT}} - 1\right]} \qquad (2.31)$$

And for low voltage operations (< 100 mV), the exponential term in Equation 2.31 dominates such that

$$\boldsymbol{I = I_L - I_0\left[e^{\frac{qV}{nkT}}\right]} \qquad (2.32)$$

Equation (2.32) is of great importance in describing certain parameters used in the characterization of solar cells. These include amongst others; short-circuit current ($\boldsymbol{I_{SC}}$), open-circuit voltage (V_{oc}), fill factor (FF) and efficiency (η) respectively.

2.6.2 Short-circuit current ($\boldsymbol{I_{SC}}$)

This refers to the current passing through a solar cell device when the voltage across it is zero (i.e. when it is in short-circuit mode). It is usually denoted as I_{SC} and represented on a solar cell current-voltage (I-V) characteristic curve as the maximum current from the solar cell under consideration. This current is mainly due to the photo-generated charge carriers such that for an ideal device (i.e. device with most tolerable resistive loss mechanism), the photo-generated (or light-generated) and the short-circuit currents

become equal [10]. Thus, at this instance, I_{SC} becomes the maximum current which may be drawn from the device.

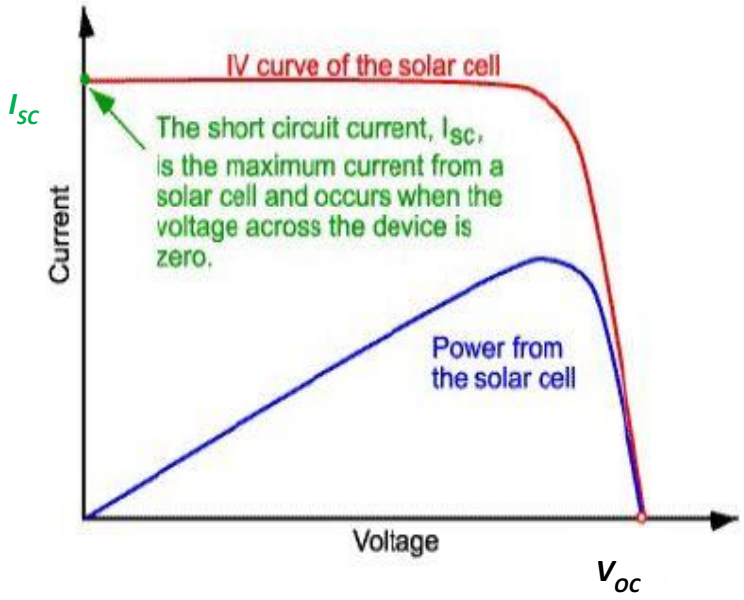


Figure 2.9: I-V curve of a solar cell showing the short-circuit current, $\boldsymbol{I_{SC}}$ [10].

Generally, the short-circuit current of a solar cell depends on the following factors;

1. Area; the surface of the solar cell exposed to solar radiation greatly determines the amount of current to be generated. As such, the short-circuit current is often described in terms of current density, J_{SC} in mA/cm^2, in order to address this dependence on area.
2. Number of photons; the intensity of light arriving at the surface of the device also offers a direct influence on the magnitude of I_{SC}.
3. Incident light spectrum; a standard spectrum is, in this case, adopted for most current measurements in solar cell fabrication which is the global standard AM1.5g spectrum.
4. Optical properties: the material optical properties (absorption and reflection) is also established to affect the photo-generation of charge carriers which, by extension, affects the performance of the solar cell.

Collection probability; short-circuit current is also a function of the cell collection probability which depends on the material's surface passivation and the life time of the minority charge carriers in the base of the device [197].

2.6.3 Open-circuit voltage (V_{oc})

The photo-current due to light-generated charge carriers is as a result of a forward bias at the p-n junction of the solar cell. The voltage responsible for this bias is called the open-circuit voltage and it is the maximum available voltage from the solar cell when it is not delivering any current to an external load. This voltage is denoted as V_{oc} and represented in the solar cell I-V curve as depicted below;

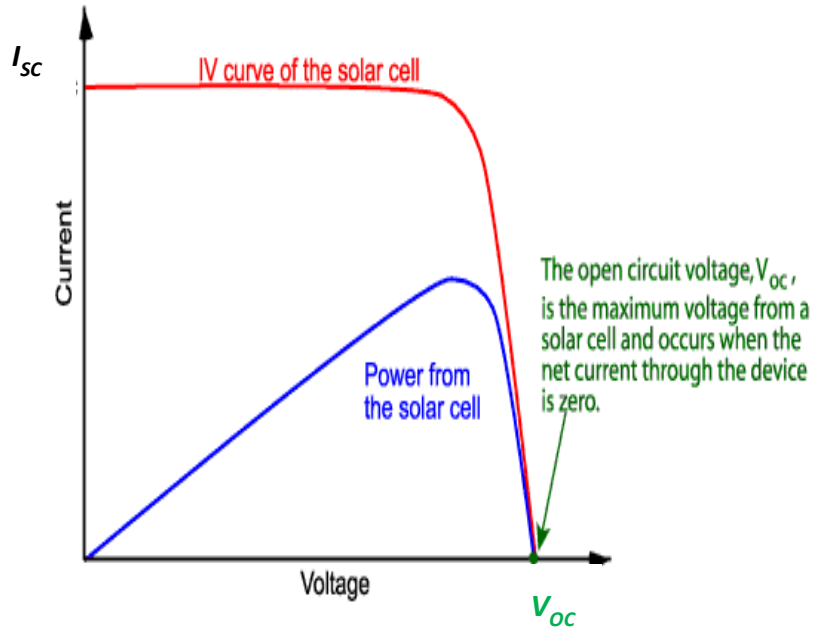


Figure 2.10: I-V curve of a solar cell showing the open-circuit voltage, V_{oc} [10].

The condition of zero current for open-circuit voltage reduces the diode equation to;

$$V_{oc} = \frac{nkT}{qV} \ln\left[\frac{I_L}{I_0} - 1\right] \qquad (2.33)$$

It is clearly shown in the above equation that V_{oc} depends on both saturation and light-generated currents. Since the saturation current has a key effect on the magnitude of open-circuit voltage and also depends on the rate of charge carrier recombination, V_{oc} is then said to be a quantitative measure of recombination in a solar cell [198]. This recombination tendency varies in different materials such that for high quality single crystalline semiconductors and under the most favorable operation conditions, the open-circuit voltage, V_{oc} could be as high as 730 mV as against the ~ 600 mV obtained in most commercial devices [196].

2.6.4 Solar cell fill factor (FF) and efficiency (η)

The power from a solar cell at the two essential operating points ($\boldsymbol{I_{SC}}$ and V_{oc}) equals zero. This suggest the idea of a solar cell fill factor, *FF* which describes the maximum power that can be generated by a solar cell with respect to its short-circuit current and open-circuit voltage respectively [200]. Derived from the "squareness" of the cell characteristic on the I-V curve (Figure 2.9), the fill factor is the ratio of the maximum power, due to squareness, to the product of $\boldsymbol{I_{SC}}$ and V_{oc}. i.e.

$$\boldsymbol{FF = \frac{P_{max}}{V_{OC} I_{SC}}} \tag{2.34}$$

An empirical expression for determining the fill factor is given, according to [201], as

$$\boldsymbol{FF = \frac{v_{oc} - \ln(v_{oc} + 0.72)}{v_{oc} + 1}} \tag{2.35}$$

where $\boldsymbol{v_{oc}}$ is the normalized V_{oc} which is given as;

$$\boldsymbol{v_{oc} = \frac{q}{nkT}} V_{oc} \tag{2.36}$$

Equations 2.35 demonstrates the significance of the magnitude of V_{oc} such that a higher open-circuit voltage will result in a higher fill factor. It also shows the importance of the ideality factor**,** $\boldsymbol{n}$ such that for simple recombination mechanisms (i.e. $\boldsymbol{n = 1}$) the normalized V_{oc} is less affected and the fill factor appreciates. For complex/large recombination mechanisms, however, a low open-circuit voltage is recorded which affects (lowers) the fill factor value.

Fill factor plays a central role in the efficiency evaluation of a solar cell. This (efficiency) is the most common solar cell parameter that is used in performance comparisons of one device with respect to another [202]. Depending on the intensity and spectral nature of the incident sunlight as well as the operating temperature of the solar cell under consideration, efficiency is extracted as the ratio of the output energy from the device to the input energy from the sun [203].

In view of the above, and with respect to the solar cell active operating points, the efficiency is given as;

$$\eta = \frac{P_{max}}{P_{in}} = \frac{V_{oc} I_{sc} FF}{P_{in}} \quad (2.37)$$

where P_{in} is the input power from the sun usually given as 1kW/m^2 for solar cell efficiency calculations and η is the efficiency.

2.6.5 Series and shunt resistances of a solar cell

As in the case of most electrical/electronic systems, resistive effects arising from the circuitry reduce the solar cell efficiency through dissipating reasonable fraction of the output power in the resistances [201]. The most common parasitic resistances are series resistance and shunt resistance.

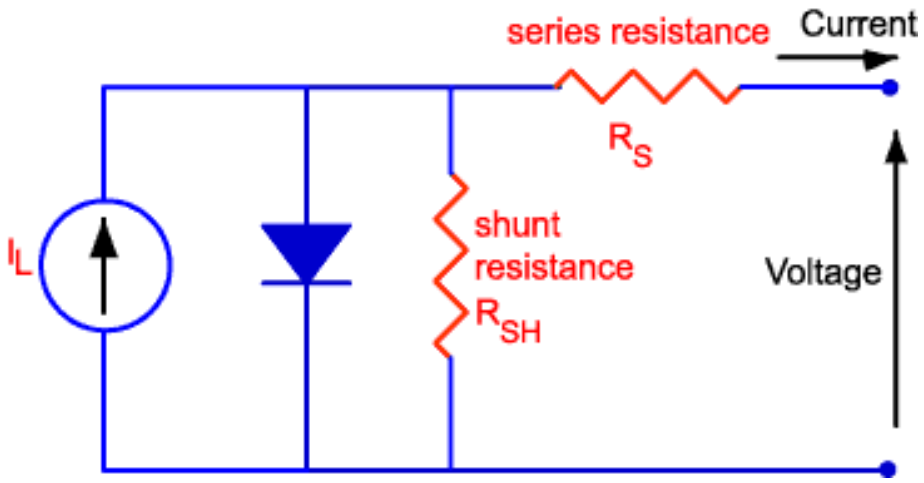


Figure 2.11: Schematic of series and shunt resistances in a solar cell [25].

Both the magnitude and impact of these resistances depend on the geometry of the cell. Although, the impact is mainly to reduce the fill factor (FF), excessively high resistive values may also reduce the short-circuit current. Also, since the magnitude of resistance depends on the area of the solar cell, a common unit for these resistances is Ωcm^2. This unit arises from the fact that current is replaced with current density in Ohm's law [204]. In a typical solar cell, the series resistance has negligible effect at open-circuit voltage since the overall current flows through the solar cell thereby making current flow through the series resistance to be zero. So, based on the assumption that the open-circuit voltage and short-circuit current are not affected by the series resistance, the impact of this resistance on the fill factor (FF) can be determined using the following empirical equation;

$$FF_S = FF_0(1 - 1.1R_s) + \frac{R_S^2}{5.4} \qquad 2.38$$

Which is valid for $R_s < 0.4$ and $V_{oc} > 10$ [205].

A reliable series resistance calculator is available [206] which determines the effect of R_s on the solar cell fill factor for area-normalized series resistances between 0.5 Ωcm^2 for laboratory type solar cells and up to 1.3 Ωcm^2 for commercial solar cells.

In the case shunt resistance however, solar cell power losses are typically due to fabrication defects rather than poor solar cell design [204]. The impact is that low shunt resistance causes power losses in the device by providing an alternate current path for the light-generated current. This alternate path will inhibit the short-circuit current as a result of decreased open-circuit voltage. The shunt effect has larger impact on the current and is particularly severe at low radiation intensities, since there will be less light-generated current [207].

The impact of the shunt resistance can be calculated in a manner similar to that used to find the impact of series resistance on the solar cell fill factor. Therefore, based on an assumption that the open-circuit voltage and short-circuit current are not affected by the shunt resistance, the impact of shunt resistance on FF can be determined using the following empirical relation;

$$FF_{SH} = FF_0\left(1 - \frac{V_{oc}+0.7}{V_{oc}} \cdot \frac{FF_0}{R_s}\right) \qquad 2.39$$

Which is valid for $R_{SH} > 0.4$ [205].

A reliable shunt resistance calculator is available [206] which determines the effect of r_{SH} on the solar cell fill factor for area-normalized series resistances in the MΩcm^2 range for laboratory type solar cells, and 1000 Ωcm^2 for commercial solar cells.

CHAPTER THREE

3.0 Experimental Techniques

3.1 Amorphous carbon film preparation

Amorphous thin and floatable carbon films of thicknesses 40 μg/cm^2 (approximately 500 nm as extracted from AFM analysis) were obtained from YISSUM Research Development Company, Hebrew University Jerusalem, Israel for this research. These films, earlier prepared as stripper foils for tandem accelerators' application, were deposited on plain glass slides (substrates) of dimensions 7.5 cm x 2.5 cm respectively. While still on the glass substrate, a pen knife was used to cut the film into rectangular pieces. This is successfully done by making the cuts parallel to the short side (2.5 cm) of the glass substrate near the edge of the carbon film. By carefully and slowly immersing the substrate into a clean dish of distilled water at an elevation of 30°-45° to the water surface, the films were floated off the slide as shown in Figure 3.1. In some instances, the water level passes the start cut of the films without separating. In such situations, the edges of the films were allowed for about two minutes to get wet before floating. Throughout the process, caution was taken not to touch the film surface with fingers or keeping the film side down.

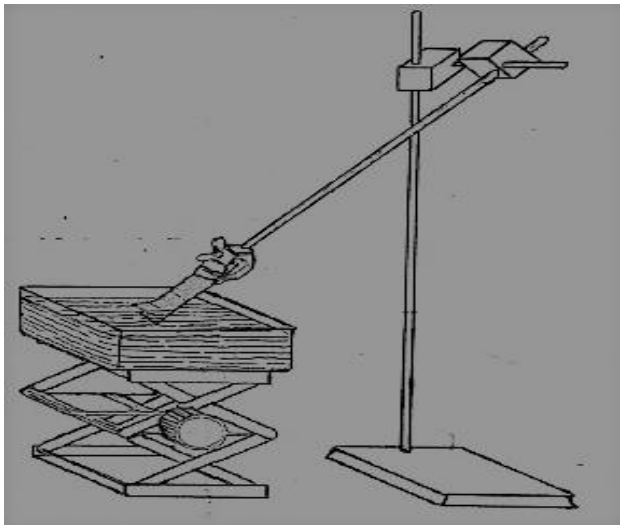


Figure 3.1: Carbon thin film floating set up.

Several thin sheets (mounts) of a metallic material (copper) were prepared. Each sheet is of dimension 1 cm x 1 cm, 0.5 mm thickness and with a 1 mm diameter hole at the centre. The edges of the hole were made smooth; free of sharp edges. These sheets were pre-washed with clean water and then thoroughly with acetone, rinsed with distilled water again, and finally wiped with methanol. A drop of domestic liquid detergent was added to the distilled water containing the floating film pieces in order to reduce surface tension effect on the mount. Using a pair of forceps, the mount was lowered into the water and below the film at an angle of about 60°. By carefully and gently lifting up, the central hole became covered and the captured film adhered permanently to the mount as shown in Figure 3.2(a). At instances where the film tend to move laterally away from the mount, a clean glass microscope slide was held in order to trap the film in position between the slide and the mount while lifting as depicted in Figure 3.2(b). The mounted films were allowed to dry in air and analyzed soon after to avoid cracking due to external pressure.

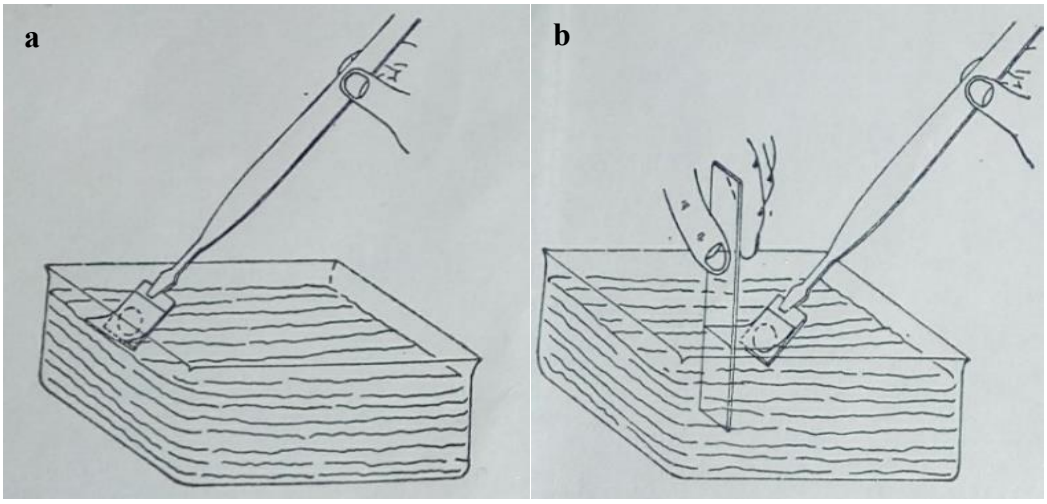


Figure 3.2: Mounting carbon film on metal sheet or other substrates; (a) direct mounting and (b) trapped film mounting.

Initial investigations into the optical response of the pristine carbon films were carried out at the materials physics research institute (MPRI) optical laboratory of the school of physics, university of the Witwatersrand. Absorption spectra were acquired at room temperature between 800 nm and 200 nm at a scan rate of 200 nm/min using a Varian Cary 500 UV-Vis-NIR spectrophotometer. The substrate material is glass, which absorbs in the deeper UV and accounts for the high absorbance values below 300 nm. This, in essence, was done in order to study the optical response of the as-deposited films which served as guide or reference points when compared to the observed optical properties of ion irradiated films. The films were floated off the glass substrates and mounted over tiny holes on the surfaces of clean and abrasion free (polished) thin sheets of material (copper in this case) and analysed as stand-alone films.

3.2 Ion implantation of carbon films

3.2.1 Introduction

As a non-equilibrium method, ion implantation is used to inject different species of atoms into solid materials in a way that precise atomic species can be efficiently introduced into preferred targets while avoiding the reactional effects of precipitation, diffusion as well as solid solubility. Structural modifications of the target are of great importance and depend largely on their pristine nature; either crystalline or amorphous which offers a great bearing on the interactions of the impinging ions with the targets

[173]. For high energy implantations, energetic ions traverse a solid target with velocities ~ 10^8 - 10^9 cm.s^{-1}, interact with the nuclei of the targets and with the electron clouds surrounding the target atoms, and finally come to rest below the surface of the target material [173]. The ion implantation procedure is mainly employed, in this context, to alter the near surface properties of the amorphous carbon thin films. A major requirement here is to introduce energetic ions of silver (Ag) into the amorphous carbon films with energies sufficiently enough to penetrate through the surface of the films and moderate enough as not to damage the films or escape to the supporting substrate (glass in this case). To this effect, an ion implanter was used. It generated a beam of silver ions, accelerated them (the Ag ions) with the required energy and guided the beam onto the target material where the ions come to rest few tens of nanometres within the target (film).

In this research, a modified version of a 200-20A2F Varian/Extrion ion implanter (Figure 3.3) at the iThemba Labs, Gauteng, South Africa was utilized. The machine was originally designed with the specifications of a production type ion implantation system for doping silicon wafers for semiconductor application. It initially has two end stations with a wafer handling system but was fitted with the RS-LN600 research end station that facilitates different target holders that allow implantations at different substrate temperatures. The ion source is fitted with a sputter type source as well as a carbon tetrachloride (CCl_4) vapour feed through attachment to the ion source. Both these systems allow the generation of ion species of any stable element of the periodic table. The sputter source, prior to modification, was designed to produce ion species from a range of source gases which are typically used in the semiconductor industry.



Figure 3.3: Front view of the modified 200-20A2F Varian ion implanter.

The sputter source was later modified (Figure 3.4) to enable the generation of a range of exotic beams rarely used in the semiconductor industry. This was enabled by purchasing a purposeful sputter type ion source for the generation of noble metal ions such as Pt and Au. Synthesis of other metallic ions is also achieved using the CCl_4 synthesis in the Freeman type ion source.

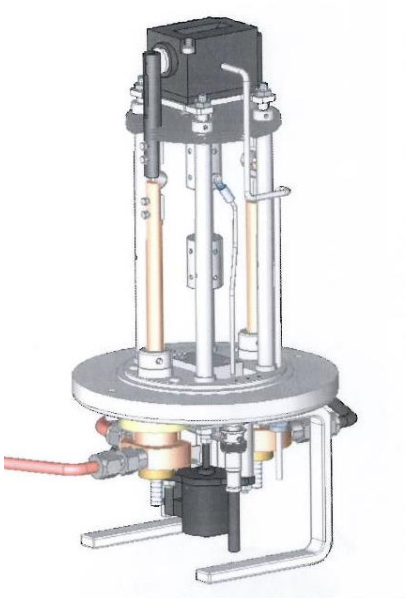


Figure 3.4: Modified 200-20A2F Varian/Extrion ion implanter sputter source.

Singly charged silver ions were implanted in the thin amorphous carbon films at varying fluences and according to specific implantation parameters. The carbon films were purchased from the supplier already on glass slides and were easy to mount on the end station target holders used in the ion implanter.

3.2.2 Silver implantation

During the implantation of silver ions in amorphous carbon thin film, a solid piece of silver was held in a crescent shaped crucible in the arc chamber of the ion source just below the filament. Carbon tetrachloride vapour was admitted into the ion source through a separate feed housed in the gas box of the ion implanter. A support gas, in this case Ar, was fed through the gas feed to the ion source assembly. At the typical operating temperatures of the ion chamber, the CCl_4 reacts with the silver material in the crucible contained in the arc chamber and the volatile silver chloride compound (AgCl) is formed. This sublimes over the hot tungsten filament of the ion source and dissociates the AgCl. The electrons from the filament ionized the different atomic species or molecules within the arc chamber as described in section 2.4. The Ag ions, along with other charged ions, get extracted out of the source chamber as a beam and into the analyzer magnet region where the appropriate ion selection takes place. The current of the analyzer magnet was set so that the magnetic field deflected singly charged ions of silver at an angle of 90° characteristic of their atomic mass. The beam of purely silver ions exits via the resolving aperture and into the acceleration tube where they receive their final energy. This beam was maintained at an average beam current of 0.55 μA for the implantation process. The singly charged Ag ions were not further accelerated in the post acceleration tube after extraction from the ion source at 25 keV, which meant that the Ag ions were implanted into the carbon films at 25 keV. The current was calculated by a current integrator. The ion beam was uniformly scanned over an area where four Faraday cups were placed in the beam path. The area of each Faraday cup as well as the beam current are parameters which the current integrator uses to digitally determine the preselected fluence for the implant. Once this required ion fluence is attained, an electronic gate automatically deflected the beam from the implantation chamber by placing it in a neutral cup thereby preventing it from reaching the target chamber. The different fluences were obtained by using a target holder with a travelling mask (Figure 3.5) that could be controlled externally while the target was under vacuum. The mask was lowered by ~ 1.0 cm so as to leave an area of 2.5 x 1 cm^2

unimplanted. The first step implanted 2.5 x 10^{15} ions/cm^2 over the remaining area of the carbon film. The mask was lower by ~ 1.0 cm and an additional fluence of 2.5 x 10^{15} ions/cm^2 was implanted. This process was continued as described in Table 3.1 and additional fluences were added at each step so that the film had eventually 6 regions of varying fluences labelled as C1 to C6.

These stages involve the appropriate addition of fractions of implantation fluence that determine subsequent fluence in the series until all the required fluence of 2.7, 2.9, 3.0, 3.2 and 3.4 x 10^{-16} atoms/cm^2 were respectively achieved at different areas of the film. Details of this implantation fluence steps are presented in Table 3.1.

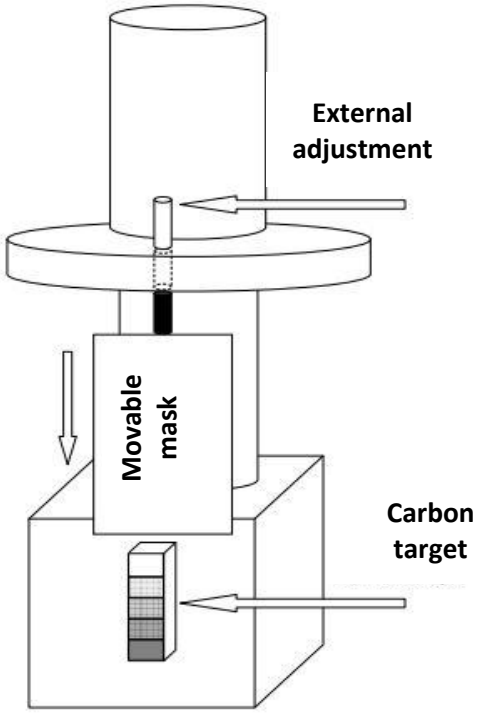


Figure 3.5: Schematic diagram of implantation stages for the various fluence.

The beam energy of 25 keV, which has direct bearing on the depth of penetration (range) of the silver ions (as described in section 2.4.4), was predetermined based on computer simulations of the implantation process using Stopping and Range of Ions in Matter-2008 package [123]. The different sections of the glass slide were scored with a table top glass cutter at ~ 1.0 cm along the length of the slide. The glass slide was

carefully placed over a sharp edge and the glass cleaved so that six sections of the glass slide was created, each with the different implanted fluence of the carbon film, C1 to C6. Little sections of these implanted films were later floated off the glass slides, captured (mounted) on clean metal sheet surfaces as described earlier and analysed/characterized as stand-alone silver-implanted amorphous carbon (Ag:a-C) films.

Table 3.1: Irradiation steps for the appropriate fluence requirements.

Sample	Required fluence, ϕ (ions/cm^2)	Irradiation dose steps (ions/cm^2)
C_1	2.5×10^{16}	2.5×10^{16}
C_2	2.7×10^{16}	$2.5 \times 10^{16} + 2 \times 10^{15}$
C_3	2.9×10^{16}	$2.5 \times 10^{16} + 2 \times 10^{15} + 2 \times 10^{15}$
C_4	3.0×10^{16}	$2.5 \times 10^{16} + 2 \times 10^{15} + 2 \times 10^{15} + 1 \times 10^{15}$
C_5	3.2×10^{16}	$2.5 \times 10^{16} + 2 \times 10^{15} + 2 \times 10^{15} + 1 \times 10^{15} + 2 \times 10^{15}$
C_6	3.4×10^{16}	$2.5 \times 10^{16} + 2 \times 10^{15} + 2 \times 10^{15} + 1 \times 10^{15} + 2 \times 10^{15} + 2 \times 10^{15}$

3.3 Characterization techniques

3.3.1 UV-visible spectroscopy

Introduction

Light as a form of energy and upon interaction with matter gets absorbed and causes a change (increase) in the energy of the atoms. A spectroscopic technique of interest is that in which there is transfer of energy between photons and the atoms of a solid sample. This is generally regarded as absorption spectroscopy. It simply involves the transition, due to photon absorption, by the electrons of an atom or molecule from a lower-energy state to a higher energy state (excited state) [174]. As the beam of electromagnetic radiation traverse through a solid sample, its intensity gets attenuated at certain selected wavelengths. This attenuation process is what brings about absorption. For this absorption to occur, there should be an interaction between the

electromagnetic field of the light beam with the atoms of the material such that absorption of a photon brings about a change in the energy of their valence electrons for UV and visible radiations while for infrared radiation, a bond's vibrational energy is altered [209]. Furthermore, the energy ($\boldsymbol{h\upsilon}$) of the absorbed photon must be equal to the energy difference ($\Delta \boldsymbol{E}$) between two of the sample's quantized energy states [174]. The ultraviolet (UV) and visible radiations constitute only a small region of the electromagnetic spectrum. Other wavelengths in the spectrum include infrared (IR), microwave, X-rays, gamma rays, cosmic rays etc. The region of each of the components above is characterized by its wavelength on the spectrum, usually expressed in nanometres unit (1 nm = 10^{-9} m) [11]. Figure 3.6 shows the electromagnetic spectrum showing the different forms of radiations and their respective regions (wavelength ranges). For spectroscopy purposes, light is characterized in the ultraviolet (10 nm - 400 nm) and visible (400 nm - 700 nm) regions respectively [210]. And within these two regions of greatest spectral interest (ultraviolet and visible), absorption of light is generally high such that light transmission is usually a negligibly small fraction [176]. Pertinent to this, solid materials of prospective optical potentials are mostly operated or characterized within visible region and the near visible wavelength (200 nm – 380 nm) of the ultraviolet region in the electromagnetic spectrum [211].

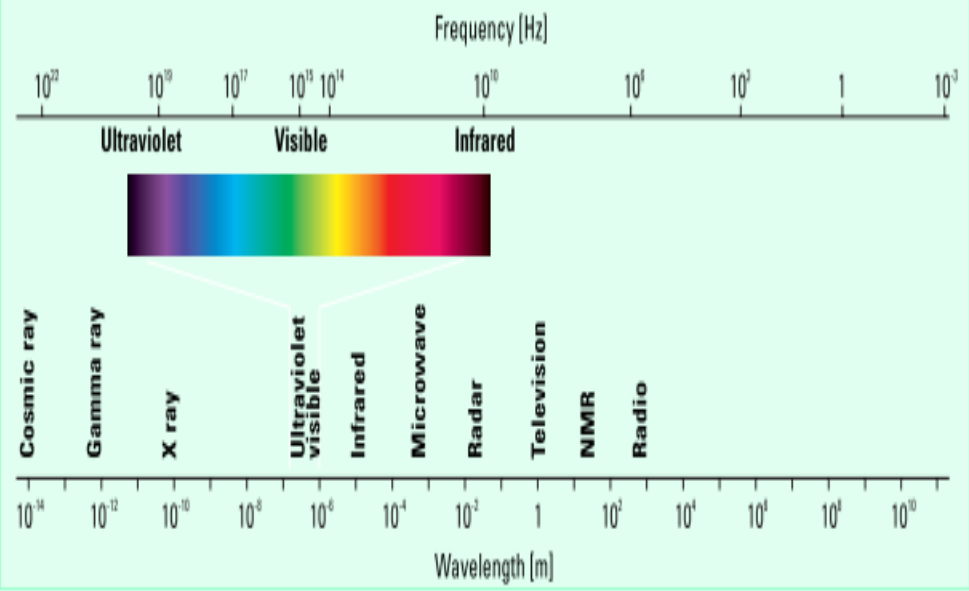


Figure 3.6: The electromagnetic spectrum, [11].

The interaction of light with the Ag:a-C nanomaterial is such that the light either gets scattered (elastically or inelastically), absorbed, or transmitted depending on the inherent properties of the nanomaterial (physical, chemical, and structural) as well as the intensity and energy of the light photons [210]. Each region of the spectrum interacts with the material to give specific spectroscopic information about the nanomaterial. It has been established that [212], within the ultraviolet and visible regions, photons create excitons by interacting with the outer shell electrons of a material and promoting them to higher energy levels while photons in the infrared region create phonons by interacting with lattice and molecular vibrations and rotations. Sequel to this, a predetermined photon energy can appropriately be chosen and tailored to investigate specific properties of interest for the material at hand. Moreover, the plasmonic property of the silver nanoparticles due to the collective motion of charges and with respect to the attraction by the bulk carbon nanomaterial background allows for the adequate investigation of the optical absorption in the UV-visible range. Infrared and Raman spectroscopies are also considered as sufficient tools [213] for this nanomaterial characterization.

As a guiding principle for the study of light-matter interaction, the total energy incident on the nanomaterial can be accounted for by the additional relationship of the absorptance (A), defined as the ratio of the energy transferred to the nanomaterial, and the fractions of the energy that are reflected (R) off the material surface and or transmitted (T) through it. So that

$$\boldsymbol{Abs = 1 - T - R} \qquad (3.1)$$

A more convenient way of expressing this transferred energy is in terms of absorbance($\boldsymbol{Abs}$), often referred to as the optical density and explained in terms of the attenuated incident light within the material. And in relation to both transmission for a transparent or reflection for a highly reflective media, absorbance is given as

$$\boldsymbol{Abs = -\log_{10}(T) = -\log_{10}(R)} \qquad (3.2)$$

The optical coefficient of absorption ($\boldsymbol{\alpha}$) describes the rate of light absorption as it traverses through a given path length or thickness ($\boldsymbol{l}$) of the material. i.e,

$$\boldsymbol{\alpha = \frac{Abs}{l} = -\frac{\log_{10}(T)}{l}} \qquad (3.3)$$

Or, using the natural logarithms

$$\boldsymbol{\alpha = a \ln 10} \qquad (3.4)$$

where the value of $\boldsymbol{a}$ is expressed in terms of the imaginary part of the complex index of refraction, $\boldsymbol{k}$ (called the extinction coefficient) and the wavelength of the incident light $\boldsymbol{\lambda}$, as $\boldsymbol{a = -\frac{4\pi k}{\lambda}}$.

One major challenge in absorbance measurements is that in a transmittance or reflectance spectrum, we often assume that all the non-transmitted or non-reflected light is absorbed by the sample under investigation. However, certain areas of the sample that are not directly illuminated also contribute to the total light absorbance. As such, special accessories are inherently provided with the sample holders which ensure that the light is directed at the appropriate spot(s) of interest [181].

3.3.1.1 Instrumentation

Most UV-visible spectrometers operate by passing a beam of electromagnetic radiation directly through the sample held in a certain fixed position (cell). Radiation, across the whole wavelengths of ultraviolet and visible ranges, is scanned for a certain period of time. Simultaneously, a radiation of same intensity and frequency as the first is also passed through a reference cell containing the same substrate upon which the sample is deposited (as in the case of thin films) [212]. The transmitted radiation is then detected by a collection of photocells and the absorption is determined by measuring the difference in intensity of radiation passing through the sample (target) and the reference substrate as depicted in Figure 3.7.

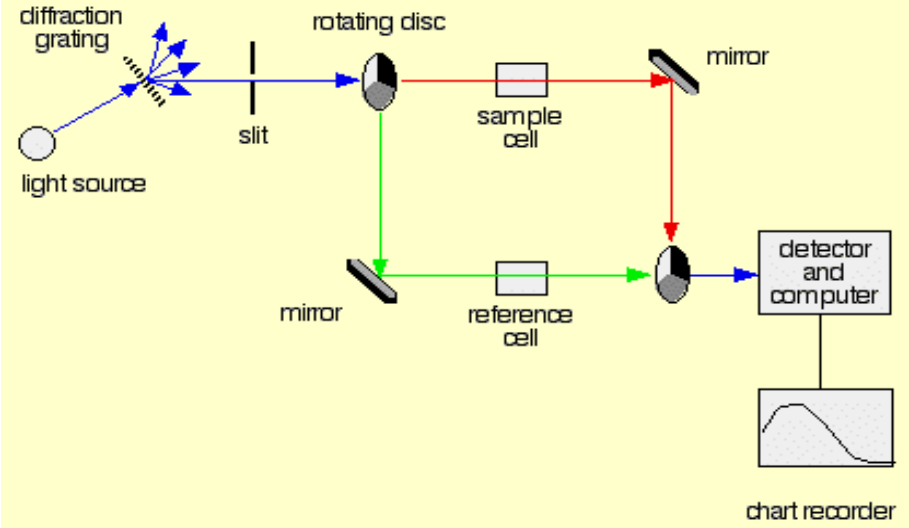


Figure 3.7: A schematic diagram of a typical ultraviolet/visible spectrophotometer [12].

Two lamps (sources) are provided for the scanning process; a deuterium or hydrogen discharge lamp covering the ultraviolet range and a tungsten/halogen lamp covering the visible range respectively. A diffraction grating is incorporated so that light from each source is separated according to its frequency/wavelength and then transformed into a narrow waveband (monochromatic) by a narrow slit. The required absorption information follows from the detection of the radiation through both the sample and reference material. This is achieved in either of the following two transduction processes [177];

- By a photodiode or a photomultiplier which converts the photons into minute electrical signals (currents), or
- By photo-induced emission of electrons by a semiconducting cell which are processed by an electron multiplier.

An automatic comparison of these currents, generated from the sample and the reference substrate, gives the required absorption spectrum.

In this research, optical absorption measurements were conducted using a Carey 500 UV-Vis-NIR (Varian) spectrophotometer at the School of Physics, University of the Witwatersrand, Johannesburg.

3.3.2 Raman Spectroscopy

Introduction

Incident monochromatic light interacts with the atoms or molecules of a target in such a way that a greater part of it is transmitted and a smaller part absorbed. The smaller absorbed part undergoes both elastic and inelastic scattering process with the atoms or molecules of the sample. In the elastic scattering, about 99.999% of all the incident photons retain the nature of their initial frequency of propagation as no energy is lost. This interaction, which is the dominant process and commonly referred to as Rayleigh scattering, is of no significance in Raman spectroscopy as it provides no useful information regarding the molecular structure, bonding and or stoichiometry of the scattering atoms or molecules. On the other hand however, about 0.001% of the photons are scattered inelastically such that the scattering from the associated vibrations of atoms or molecules are excited leading to a shift in the magnitude, by one vibrational unit [215], of the frequency of the incident photons.

Raman spectroscopy is a non-destructive standard spectroscopic technique in that it serves as a powerful tool for the identification of the bonding(s), the symmetries of molecular structures as well as the energies associated with the fundamental vibrational excitations of solid materials [6] including carbon-based materials [184]. It is basically a technique, as earlier mentioned, that utilizes the inelastic scattering of monochromatic light emanating from, usually, a laser source [217]. The Raman effect was first discovered or postulated by C.V. Raman and K.S. Krishnan in 1928 but until the invention of the laser in the 1960's that it was later explored in more details [183]. This phenomenon utilizes the inelastic scattering of photons when they interact with the molecules of a sample. Whereas most of the photon are scattered elastically (Rayleigh effect, i.e. with the same cadre as the source light), some of the photons are scattered at different frequencies compared to that of the input light. According to classical physics model as compiled and presented by Princeton Instruments [185], the inelastically scattered photons impart a sample's molecule with certain energy which causes it to vibrate and rotate. In the course of its vibrational motion, a new photon is emitted at a specific frequency for each degree of freedom of vibration. This is fundamentally important because every molecule has its unique set of frequencies which act as a fingerprint by which it can be identified. A range of different Raman

measurement techniques are in use for the identification of chemicals or molecules with Classic Backscatter Raman as the most common. Furthermore, the technique is found to be an excellent tool for the adequate understanding of the distinguishing properties of various allotropes of carbon, a feature that motivated its choice in the characterization of both un-implanted and implanted carbon-based materials [186].

3.3.2.1 Principles of Raman

When a monochromatic light of frequency $\boldsymbol{\nu_0}$ interacts with the molecules of a given sample, the molecules get excited and are transformed into independent oscillating dipoles [187] which consequently emit light of different characteristic frequencies in the following three ways;

- A molecule in a non-Raman mode absorbs the photon, gets excited and vibrates within the same vibrational state as the source while emitting light of the same frequency as the excitation source (ν_0). This is called elastic or Rayleigh scattering.
- A Raman-active molecule, initially at a normal vibrational state, absorbs the photon and impart some of its energy to the active mode with a different frequency ν_m thereby reducing the frequency of the source light to $\nu_0 - \nu_m$. This is called "Stokes" or "Stokes frequency".
- A Raman-active molecule, initially in the excited vibrational state, absorbs the photon and release excess energy such that the frequency of the scattered source light appreciates higher as $\nu_0 + \nu_m$. This is called "Anti-Stokes" or Anti-Stoke frequency.

According to literature [183], a significant percentage of all the incident light photons in Raman spectroscopy undergo Rayleigh scattering and only small percentage produces the required Raman effect resulting in signals with frequencies $\boldsymbol{\nu_0 \pm \nu_m}$. This is a great setback in the earlier applications of Raman spectrometers and a more reason why most spectrometers now have filters (notch/tunable), laser stop apertures, etc. that are incorporated to enhance the quality of Raman spectra by reducing the Rayleigh effect [220].

3.3.2.2 Theory of the Raman effect

There are basically two interpretative approaches by which the physics of Raman effect is described namely; the classical wave interpretation which considers light as an electromagnetic radiation containing oscillating electric field at a given frequency and interacting with atoms or molecules of a solid through its polarizability and the quantum particle interpretation which considers light as a photon, emitted or absorbed, due to its inelastic scattering by the atoms or molecules of the solid target.

A brief overview of both approaches is given in the next section and based mainly upon discussions from these texts [108, 183, 187 - 191].

- Classical wave interpretation

The classical approach, apart from its consideration of light as containing oscillating electric field, assumes that photons of the incident light interact with the dipole moment of the atoms or molecules of the material under investigation. It also avoided, totally, the mathematical complexities in the dependency of the molecules' dipole moment on the electric field component of the radiation as well the distortion of stable electronic distribution of the molecules. To this effect, the "mass on a spring" classical model of a simple diatomic molecule is considered and analysed in a completely classical frame of reference utilizing the Hooke's law. A simple system of diatomic molecule as a mass on a spring is considered in Figure 3.8 which comprises of a spring of constant $\boldsymbol{k}$, representing the bond strength, such that $\boldsymbol{x_1, x_2, m_1, and\ m_2}$ are the displacements and atomic masses of the vibrating atoms respectively.

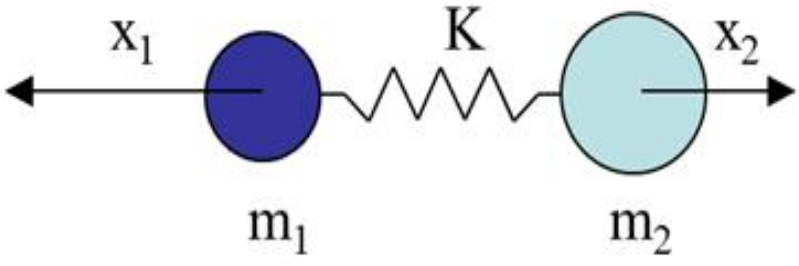


Figure 3.8: Diatomic molecule as a mass on a spring.

Using Hooke's law, the molecular displacement can be expressed based on the classical approximation as follows;

$$\frac{m_1 m_2}{m_1 + m_2}\left(\frac{d^2 x_1}{dt^2} + \frac{d^2 x_2}{dt^2}\right)\alpha - (x_1 + x_2) \quad (3.5)$$

So that

$$\frac{m_1 m_2}{m_1 + m_2}\left(\frac{d^2 x_1}{dt^2} + \frac{d^2 x_2}{dt^2}\right) = -k(x_1 + x_2) \quad (3.6)$$

Where $\mu = \frac{m_1 m_2}{m_1 + m_2}$ is the reduced mass of the diatomic system and $q = (x_1 + x_2)$ is the total displacement.

So that Equation 3.6 becomes

$$\mu \frac{d^2 q}{dt^2} = -kq \quad (3.7)$$

Or

$$\frac{d^2 q}{dt^2} = -\left(\frac{k}{\mu}\right) q \quad (3.8)$$

Solving Equation 3.8 with respect to the periodic motion of the atomic displacement yields:

$$q = q_0 \cos(2\pi v_m t) \quad (3.9)$$

Where v_m is called the molecular vibration and defined in terms of μ and k as

$$v_m = \frac{1}{2\pi}\sqrt{\frac{\mu}{k}} \quad (3.10)$$

From the foregoing discussion and as contained in Equations 3.9 & 3.10, it appears that the excited molecules are vibrating via cosine pattern and having frequency directly proportional to the molecular bond strength, k and inversely proportional to the reduced mass, μ. This clearly infers that each vibrating molecule will have unique vibrational signatures determined by both the atoms therein as well as the characteristics of the individual interatomic bond.

Since the polarizability, α of a molecule is a function of the displacement, q, then the vibrational frequencies can easily be determined from the induced dipole moment, P due to the interaction of light with vibrational molecules. So that

$$\boldsymbol{P} = \boldsymbol{\alpha E_0} \tag{3.11}$$

Or, in terms of Equation 3.9

$$\boldsymbol{P} = \boldsymbol{\alpha E_0 \cos(2\pi v_0 t)} \tag{3.12}$$

where $\boldsymbol{E_0}$ and $\boldsymbol{v_0}$ are the intensity and frequency of the electric field.

Now expressing the polarizability as a linear function of displacement and in terms of small amplitude approximation, i.e.

$$\boldsymbol{\alpha} = \boldsymbol{\alpha_0 + q\left(\frac{\partial \alpha}{\partial t}\right)_{q=0}} + \cdots, \tag{3.13}$$

and a combination of Equation 3.13 with Equations 3.9 and 3.12 gives

$$\boldsymbol{P} = \boldsymbol{\alpha E_0 \cos(2\pi v_0 t) + q_0 \cos(2\pi v_m t)\, E_0 \cos(2\pi v_0 t)\left(\frac{\partial \alpha}{\partial t}\right)_{q=0}} \tag{3.14}$$

Equation 3.14 reveals two major effects resulting from the photon-molecule interaction. The first term describes the earlier mentioned dominant Rayleigh scattering, having frequency $\boldsymbol{v_0}$, which results in no frequency change in the incident radiation. The second term is the component of the Raman scattered light which when expanded gives;

$$\boldsymbol{q_0 E_0 \left(\frac{\partial \alpha}{\partial t}\right)_{q=0} [\cos(2\pi\{v_0 - v_m\}t)\cos(2\pi\{v_0 + v_m\}t)]} \tag{3.15}$$

Equation 3.15 demonstrates how the linear induced dipole moment, $\boldsymbol{P}$ gives rise to two different radiations of varying frequencies; $\boldsymbol{\cos(2\pi\{v_0 - v_m\}t)}$ that gives rise to a radiation at a reduced frequency of $\boldsymbol{v_0 - v_m}$ and responsible for the Stoke Raman scattering, and $\boldsymbol{\cos(2\pi\{v_0 + v_m\}t)}$ that gives rise to a radiation at an increased frequency of $\{\boldsymbol{v_0 + v_m}\}$ and responsible for the Anti-Stoke Raman scattering. Molecules will be mostly found in the ground state, at room temperature, and there is a lower probability that a photon will be Anti-Stokes scattered. Raman measurements from Stokes shifted light are much higher in intensity and are used for Raman analysis.

- Quantum particle interpretation

This interpretation approach is used to better visualize the classical wave interpretation and offer more viable information about the process. Here, photon from the electromagnetic radiation is considered to directly interact with the phonon in the target (matter) such that the radiation is regarded as being either absorbed or emitted due to the upward or downward transition of a molecular system between two discrete energy levels. This transition can be in a vibrational mode, rotational mode or a combination of both and according to the perturbation theory of quantum mechanics, the energies of that molecule in vibrational and rotational modes are quantized. Thus:

$$\boldsymbol{E_v = hv\left(m + \frac{1}{2}\right)} \qquad (3.16)$$

where $\boldsymbol{m = 0, 1, 2, 3}$, ... represents the quantum number.

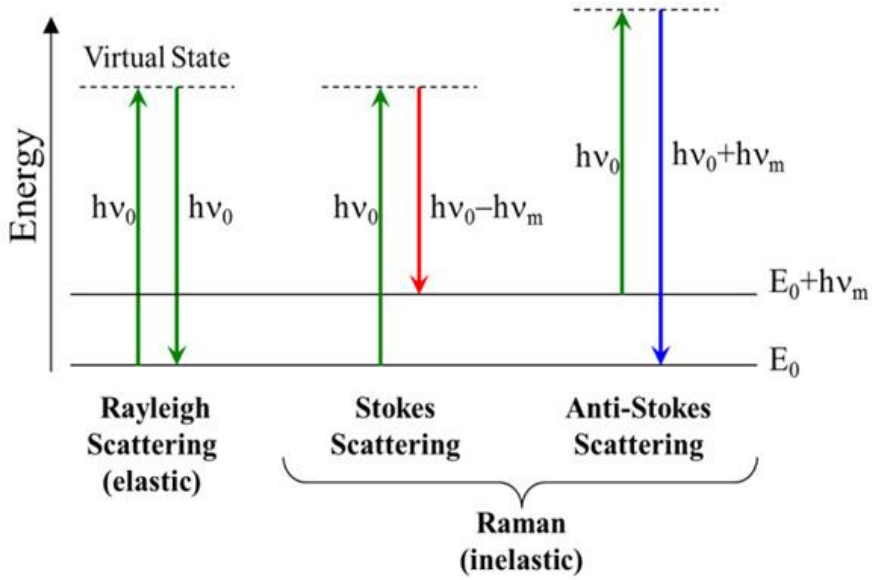


Figure 3.9: Jablonski representation of Rayleigh and Raman scattering, adopted from [221].

Now referring to Raman effect as a simple two-photon system in which energy emission or absorption due to the downward and upward transitions strictly occur between two energy level, then the only two permitted transitions would also strictly obey the quantum mechanical selection rule of $\Delta J = 0, \pm 2$, where J is the total angular momentum number. Applying this rule to Equation 3.16 gives the three conditions of Rayleigh scattering at $\Delta J = 0$, the Stokes scattering at $\Delta J = +2$ and the anti-Stokes scattering at $\Delta J = -2$ respectively. This was also summarized in Jablonski representation of Figure 3.9 and as highlighted in section 3.4.2.1 above.

3.3.3 Instrumentation

The Raman spectrograph utilized for the Raman scattering measurements of our carbon nanomaterials was briefly described in this section; including the details of the laser source as applied to sample illumination system. The instrument comprises mainly of four major parts;

- An excitation source (laser),
- A sample illumination system,
- A wavelength selector (or filter), and
- A detector (CCD or photodiode array).

An electromagnetic radiation from a laser beam (usually in the ultraviolet, visible, or near infrared range) is used to illuminate the sample under investigation such that upon interacting with the sample's atoms or molecules, scattered light is collected via lens(es) and sent through an interference filter and processed into an appropriate Raman spectrum of the sample.

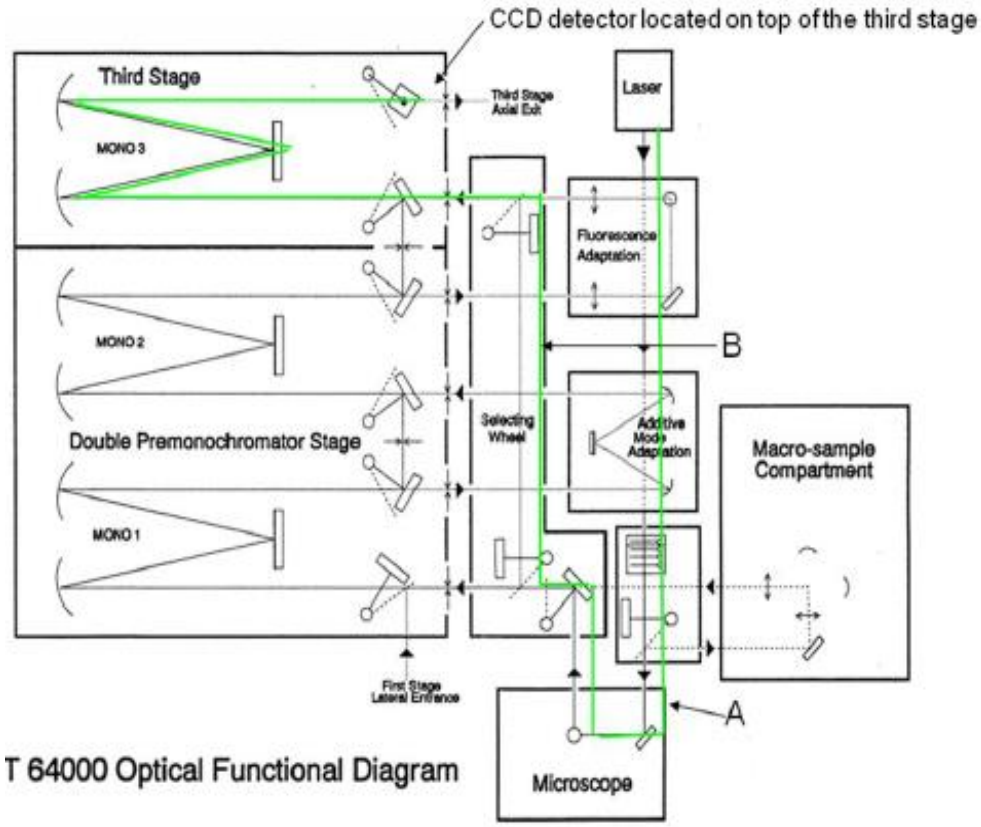


Figure 3.10: Schematic diagram of the Raman Spectrograph showing beam trajectory from [13].

The Argon ion-laser of intense but coherent monochromatic radiation and having 514.5 nm excitation wavelength was used for the whole Raman session. The logic in the choice of this excitation wavelength (i.e. 514.5 nm) was due to the dependence of the light scattering power, $\boldsymbol{P_s}$ on the frequency of the incident radiation, $\boldsymbol{\upsilon}$. It was already shown [223] that there is a linear relationship between the power of the scattered light, $\boldsymbol{P_s}$ the intensity of the incident light, $\boldsymbol{I_0}$ and the inverse of the fourth power of the source excitation wavelength, $\boldsymbol{\lambda}$ as follows;

$$\mathbf{P_s\ \alpha\ \frac{I_0}{\lambda^4}} \tag{3.17}$$

Or, since $\boldsymbol{v\ \alpha\ \frac{1}{\lambda}}$, then

$$\boldsymbol{P_s\ \alpha\ I_0 v^4} \tag{3.18}$$

So that for laser source of constant intensity,

$$\boldsymbol{P_s\ \alpha\ v^4} \tag{3.19}$$

Equation 3.19 describes the dependence of the source scattering power on the fourth power of the frequency of the incident light. The Argon ion-laser of wavelength up to 514.5 nm and other short wavelength laser sources like Krypton (530.9 nm) are preferred to longer wavelength laser sources like Helium-neon (from about 632.8 nm up to about 3.3913 μm).

In this study, a Horiba LabRAM HR Raman spectrometer equipped with an Olympus BX41 microscope attachment was used. The Raman spectrograph has a sample illumination system that comprises of glass only. It employs the dispersive Raman mode of operation for the appropriate separation of the unwanted strong Rayleigh scattered light from the desired weak Raman scattered light. The Olympus BX41 microscope, attached to the spectrograph, is used to focus the filtered laser beam unto the sample. A working distance of 50X or 100X objective is chosen depending on the nature of the sample; 100X objective was used in this work. In order for a preselected wavelength of operation for the microscope to be achieved, a narrow band-pass filter is used to remove all unwanted laser plasma lines. The beam of light gets scattered by the sample and redirected via optical mirrors into the spectrometer operating in a single spectrograph mode. An entrance slit transmits the light unto a grating for dispersion. Two different gratings are available in the spectrograph which can be employed based on resolution and spectral range requirements. For a reduced resolution but a wide spectral range, the 600 lines/mm grating is used while the 800 lines/mm provides an improved resolution but a narrow spectral range. For the purpose of this research, the 600 lines/mm grating was utilized. Upon dispersion, the scattered light is collected by a liquid nitrogen-cooled charge-coupled device (CCD) detector which processes the signals and produces the Raman spectrum. The signals from the detector were processed with the aid of Labspec V5 scientific software. The detector was also kept at a low temperature of about 140K via liquid nitrogen-cooling while the operating

temperature of the micrograph was the normal room temperature. The laser beam power supplied to the sample was maintained at approximately 0.4 mW to minimise localised heating effects.

3.3.4 Scanning Electron Microscopy

Unlike an optical microscope, the scanning electron microscope utilizes the very short wavelength of electrons in order to generate images at greater magnifications. As one of the most versatile instruments for morphological characterization and typically comprising of an electron source (electron gun), electron column, sample chamber and a visual display system, this powerful instrument employs a well-focused beam of high-energy electrons to generate variety of useful surface signals that are characteristic of solid samples [208]. These generated signals reveal certain information of the sample surface as morphology, crystalline structure as well as chemical composition. The technique is considered mostly as non-destructive in the sense that x-rays generated due to electron-sample interactions do not result in volume loss of the sample under investigation such that a single sample can be repeatedly analyzed. The sample chamber is capable of accommodating sample areas from 1 cm to as low as 5 microns in width and producing images in the magnification range of 20 times to as high as 600 000 times for high resolution applications; typical spatial resolution ranges between 50-100 nm [209].

3.3.4.1 Basic scanning electron microscopy principle

The scanning electron microscope basically comprises of an electron gun (source) that emits electrons thermionically into a column (containing multiples of condenser and objective lenses) and directing these energetic electrons unto the surface of a solid sample. A schematic diagram of a typical scanning electron microscope showing its major components is depicted in Figure 3.11. These electron-sample interactions produce a variety of signals, as the electrons decelerated within the solid sample, such as secondary electrons, backscattered electrons, diffracted backscattered electrons, photons, visible light and heat [226]. The secondary electrons produced are mainly utilized for morphology and topography of samples while the backscattered electrons find applications in illustrating compositional contrasts of multiphase analytes (i.e.

rapid phase discrimination of samples). The photons are in the form of characteristic x-rays which are utilized for elemental analysis of the samples under consideration.

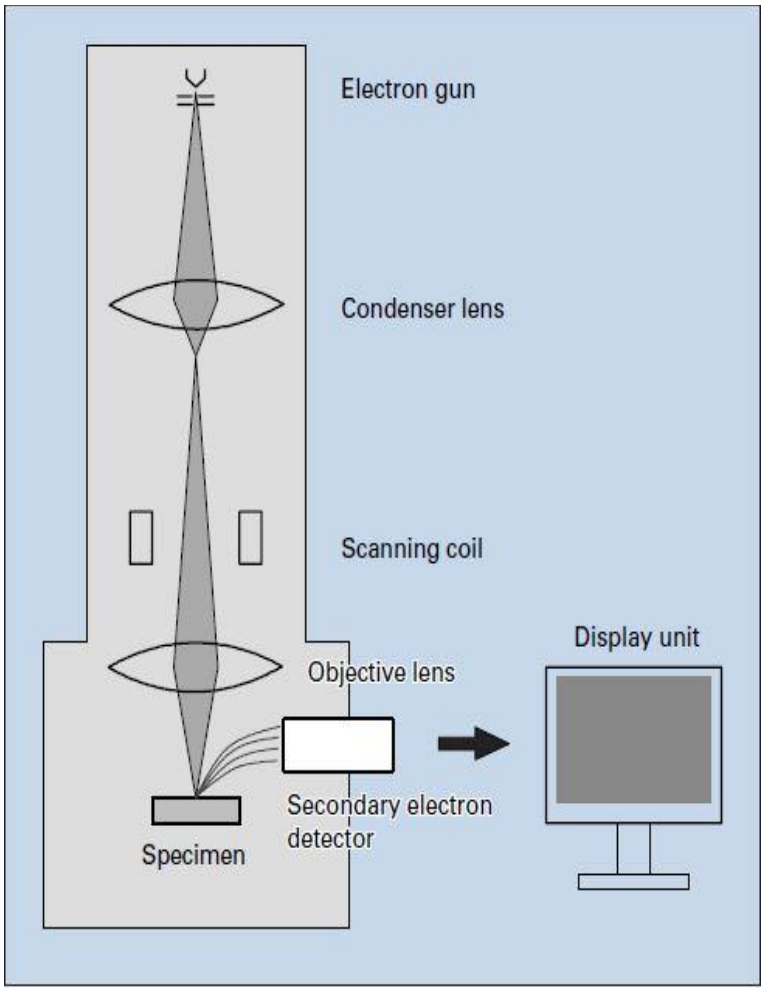


Figure 3.11: Schematic diagram of a typical scanning electron microscope [208].

Different kinds of electron sources are in use for scanning electron microscopy purposes. These include amongst others; lanthanum hexaboride (**LaB_6**) filament, tungsten filament, tungsten field-emission tip, etc. capable of producing electrons which are generally accelerated via the gun's grid and anode to a maximum voltage of ~ 30 kV. Upon exiting the grid aperture, the beam of accelerated primary electrons is focused by a collection of condenser lenses through a scanning coil and an objective lens before they are incident on the sample surface [224]. The combined function of the electron gun and the electron lenses greatly influences the overall transition of the accelerated electrons down the evacuated SEM column. The SEM column base is,

under normal operating conditions, evacuated to about 10^{-4} Pa vacuum (which is about 10^{-6} torr). A control console is the display system consists basically of a cathode ray oscilloscope (CRO) viewing screen equipped with control knobs and keys for appropriate beam control [226].

For the purpose of this research, a scanning electron microscope JEOL JSM- 7001F was used at the Microscopy and Microanalysis Unit (MMU) of the Wits University. It has 1.1 nm microscopic resolution of secondary electron image (SEI) at an accelerating voltage of 30 keV or 2.2 nm resolution at 1 keV accelerating voltage. The driving energy changes in steps of 10 V in voltage range 0.5 - 2.9 keV and steps of 100 V in the range 2.9 – 30 keV while its magnification ranges from 25 to 19 000 times for low magnification imaging mode and from 100 to as high as 650 000 times for high-resolution imaging mode. At an appropriate operation vacuum of ~ 10^{-8} Pa, the facility can generate electrons with quite a small energy spread (at low accelerating voltages) which is suitable for high resolution applications. At an appropriate operation vacuum of ~10^{-8} Pa, the facility is capable of generating electrons with quite a small energy spread (at low accelerating voltages) which is suitable for high resolution applications [227].

3.3.5 Transmission Electron Microscopy

Introduction

Transmission electron microscopy (TEM) is a powerful technique for the microstructural characterization of materials. First invented in 1933 by the two German scientists Max Knoll and Ernst Ruska [193], the transmission electron microscope passes a beam of energetic electrons through a very thin layer of a sample and utilizes series of powerful condenser lenses and apertures to produce a highly magnified image of the thin sample on a phosphor screen.

3.3.5.1 Basic TEM microscopy principle

A modern TEM basically consists of a vertically oriented beam column, about 2.5 m tall and 30 cm diameter, which is capable of achieving up to about 2 Å image resolution. In contrast to the maximum resolution of about 200 nm by a conventional transmission light microscope, TEM as an updated version exploits the wave properties of electron

to greatly improve on the resolution, hence providing deep insight on the microstructural properties of samples [79]. Furthermore, due to the wave-particle duality of electrons, the energetic electrons from the source (electron gun) of a TEM can appropriately be focused towards the sample, using series of condenser lenses, at a particular wavelength described by the de Broglie relation as;

$$\boldsymbol{\lambda} = \frac{\boldsymbol{h}}{\boldsymbol{m_e v}}, \qquad (3.20)$$

where $\boldsymbol{h}$ is the Planck's constant while $\boldsymbol{m_e}$ and $\boldsymbol{v}$ are the rest mass and velocity of the particle (electron in this case) respectively.

For a highly energetic electron of charge, $\boldsymbol{e}$ the energy E (in keV) is given as;

$$\boldsymbol{E} = \frac{\boldsymbol{m_e v^2}}{\boldsymbol{2}}, \qquad (3.21)$$

So that:

$$\boldsymbol{\lambda} = \boldsymbol{h}(\boldsymbol{2 m_e E})^{\frac{1}{2}} \qquad (3.22)$$

Equation 3.22 is the non-relativistic electron wavelength equation which takes into account the relativistic correction due to a relatively higher accelerating voltages (above 100 keV) of source electrons, such that

$$\boldsymbol{\lambda} = \boldsymbol{h}\left[\boldsymbol{2 m_e E}\left(\boldsymbol{1} + \frac{\boldsymbol{E}}{\boldsymbol{2 m_e c^2}}\right)\right]^{\frac{1}{2}} \qquad (3.23)$$

where $\boldsymbol{c}$ and $\boldsymbol{m_e}$ are the velocity of light in a vacuum and electronic rest mass respectively.

Equations 3.22 and 3.23 are used to determine both the relativistic and non-relativistic wavelengths associated with the operation of transmission electron microscopes at different accelerating voltages [14]. For a given accelerating voltage, say 100 keV, $\boldsymbol{\lambda}$ was found to be 0.0386 Å and 0.0370 Å respectively. And for the fact that the resolving power of an ideal (non-aberration) transmission electron microscope is slightly less than the Bohr's radius of an atom [229], TEM resolution should then be able to image the individual atoms for a sample under investigation thereby making this technique

more appropriate for the microstructural characterization of crystalline and amorphous materials.

3.3.5.2 Instrumentation

A transmission electron microscope basically comprises of three main parts; an illuminating system (containing an electron gun and the first condenser lenses), objective/stage compartment (housing the second condenser lenses, aperture, specimen holder, etc.), and the imaging system (screen).

Figure 3.12 shows a schematic diagram of a typical transmission electron microscope. The electron gun, at the top of the TEM column and usually made from tungsten or lanthanum hexaboride, supplies highly energetic electrons to the instrument. The electron energy depends largely on the sample nature and the information required from it. The stream of electrons produced gets accelerated down the column and exit through a tiny (< 1 nm) hole just beneath the filament. It is then collected by a system of condenser lenses (first and second) which act as controls by focussing it into a small, thin, and coherent beam (spot size) as well as projecting its demagnified form onto the sample chamber while controlling the spread of illumination. A condenser aperture then collimates the beam to appropriate intensity just before interacting with the sample.

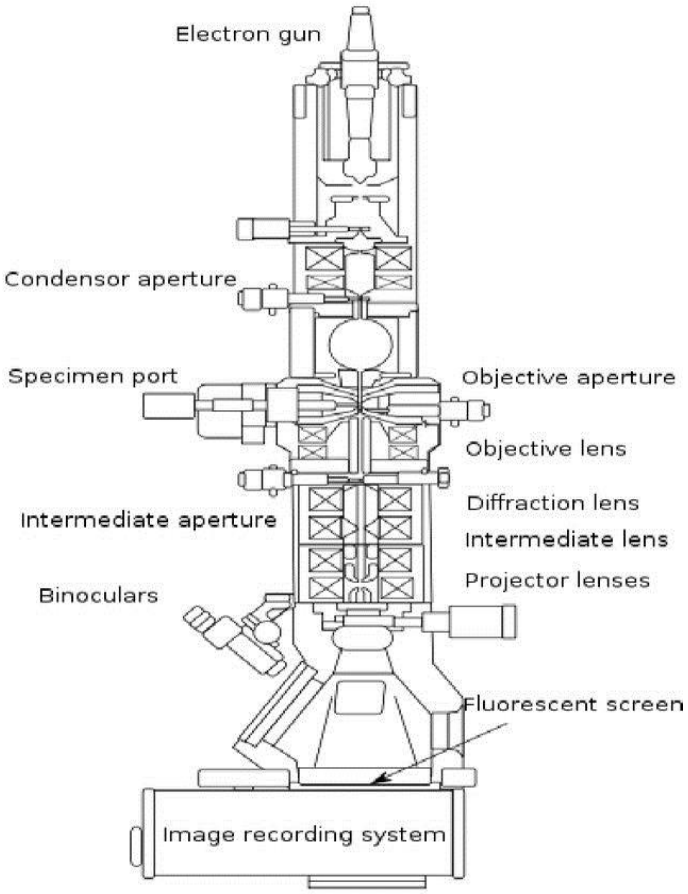


Figure 3.12: Block diagram of a Transmission Electron Microscope [14].

It is worth noting here that the illumination system operates in two modes; the parallel and convergent beam modes. The parallel beam mode is employed mainly for TEM imaging and selected area diffraction (SAD), while the convergent mode is applied in scanning transmission electron microscopy (STEM) imaging coupled with a convergent-beam electron diffraction (CBED) [91].

At the sample or specimen chamber, the beam interacts with the sample in one of the following three ways. It is either transmitted (unscattered), diffracted (elastically scattered), or inelastically scattered [196]. An objective aperture, situated just below the sample holder, filters out high-angle diffracted electrons from the emanating image beam in order to enhance contrast.

The filtered image beam approaches an optical arrangement of intermediate and diffraction lenses where it is magnified and projected towards the imaging system with the aid of a projector lens. The imaging system is basically a phosphor screen

commonly made of fine particulate zinc sulphide (10-100 μm) upon which a magnified light-patterned image is finally produced [231]. It usually contains darker regions representing areas of fewer electron transmission and lighter regions representing areas of more transmission of electrons upon their interaction with the sample under investigation. These two regions of interest form the basis for the classification of images formed by transmission electron microscope.

3.3.5.3 Bright field and dark field images

The electron populations used in the image formation TEM describe the image type; namely bright field and dark field images. Depending on the nature of sample, some areas may scatter or absorb the impinging electrons while other areas transmit the electrons. Areas that absorb or scatter electrons appear darker in the screen while areas that transmit appear brighter. In bright field mode, TEM aperture is used to select the transmitted electron beam such that the absorbed/scattered electrons are blocked. This will cause the sample areas containing crystalline or heavy particles to appear dark. In the dark field mode however, the reverse procedure is utilized so that areas containing the bulk of the material appear bright while the transmitting areas appear dark [231].

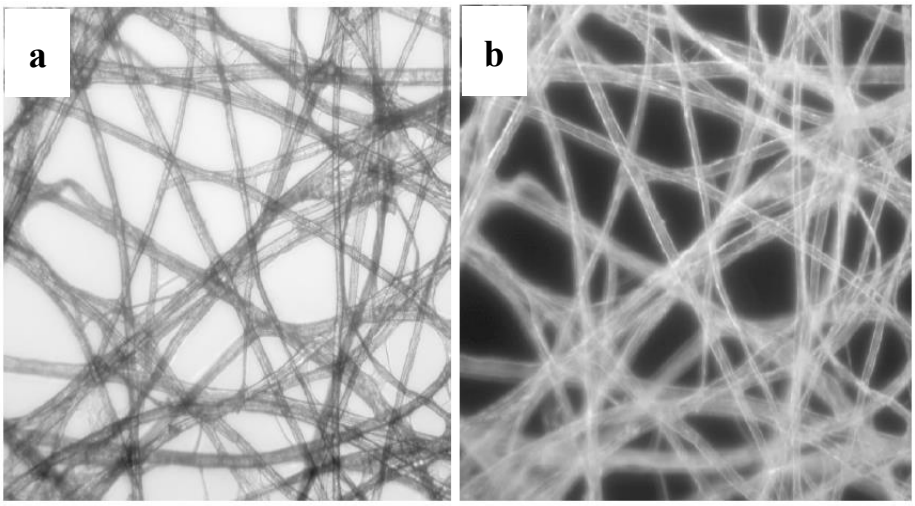


Figure 3.13: Typical TEM images of a tissue paper sample in (a) bright filed mode and (b) in dark field mode [14].

Although both SEM and TEM utilize beam of energetic electrons, the techniques differ largely in the nature of interaction of samples with the electrons in the beam. In SEM, the electron beam scans over the sample surface on an aluminium slab while in TEM

it passes through a thin section of the sample which is supported on a TEM grid. Image produced in SEM is of the surface while TEM produces a two-dimensional projection of the sample providing details of the internal composition. To this effect, sample thickness is insignificant in SEM whereas in TEM only small amount of the sample is cut into thin section for the analysis.

For the purpose of this research, an FEI Tecnai T12 high-contrast/high-resolution transmission electron microscope was used at the MMU of the Wits University. It has accelerating voltage ranging from 20 kV to 120 kV, ideal for the type and nature of samples (C1 to C6) under investigation, with a standard working magnification from 22 to 340000 times. Tiny sections of the nanocomposites were floated off the glass substrates, carefully captured on carbon lacey 200 mesh copper grids, and dried at room temperature.

3.3.6 Energy Dispersive X-ray Spectroscopy

Introduction

The invention, in the early 60's, of the energy dispersive X-ray semiconductor detector has made possible its successful incorporation in virtually all existing electron microscopes for adequate conduction of electron probe microanalysis. This is evident in the wide scientific acceptance of such a detector due to numerous analytical merits such as wide coverage of energy ranges of detected X-rays, characteristic detection efficiency, and cost effectiveness [232]. Energy dispersive X-ray spectroscopy (EDS, or EDX) is a powerful analytical technique that utilizes the generation of characteristic X-rays for elemental (qualitative or quantitative) analysis or chemical characterization of solid samples. The generation of these characteristic X-rays is associated with the transition of electrons, due to vacancy transfer, from one shell to another. At the instance of bombarding a solid sample with an energetic beam of electrons (primary electrons), some of the electrons in the innermost shells of the sample atoms are knocked off from their respective shells (secondary electrons) thereby creating vacancies in the atomic structure. Some electrons from outer electron energy shells of the atoms fall in to fill these created vacancies and, in the process, release certain energy in the form of X-rays which are characteristic of the parent atoms. The difference in energy of between the transition levels (orbits) concerned is equal to the energy of the generated X-rays.

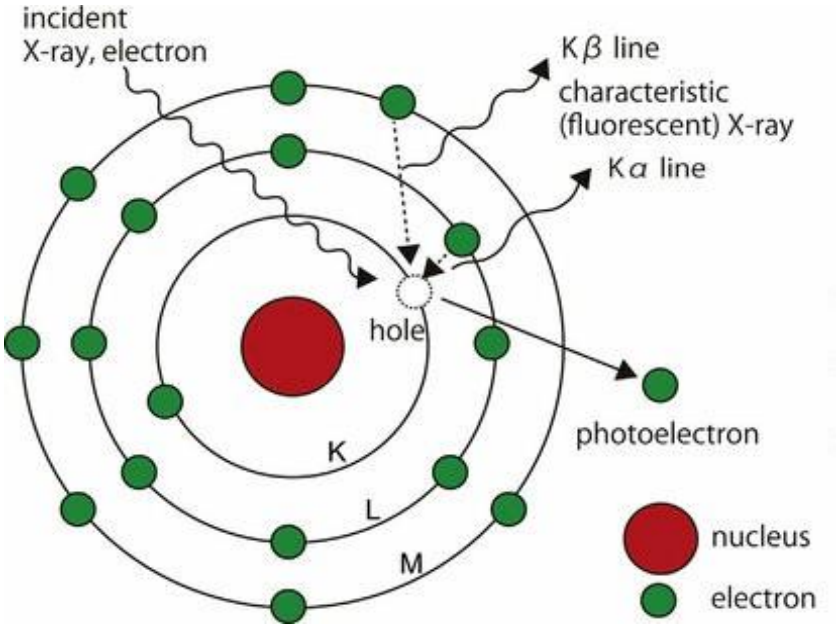


Figure 3.14: Mechanism for X-ray generation [15].

A very important feature of this technique is its detecting power with respect to sample size and or quantity. For most modern EDS spectrometers, detection limits of less than 10^{-12} g and 10^{-19} g for bulk samples and thin sections, respectively, have been featured [233]. In this context, the spectrometer basically utilizes an X-ray spectrum emitted when a beam of electrons bombards a solid sample. The emitted spectrum gives unique information necessary for the chemical analysis of the sample. In principle, elements with atomic numbers > 4 (i.e. from Boron, B) up to 92 (Uranium, U) can be detected using EDS technique but with uncertainties in the detection of light elements (Z < 4). And due to the relative simplicity in handling X-ray spectra, qualitative analysis of the sample under investigation is easily conducted via spectral lines' identification. For quantitative analysis however, the intensities of the respective identified spectral lines are measured in comparison with certain calibrated standards [234].

3.3.6.1 Nomenclature of Characteristic X-rays

The naming of a particular characteristic X-ray line follows from the initial vacancy containing shell and the shell from which an electron falls-in to fill the created vacancy.

For instance, a vacancy filling electron dropping from adjacent (L) shell to K-shell will emit a Kα x-ray. If it however drops from the M-shell (two shells away from K-shell), the emitted x-ray is named a Kβ x-ray. The same naming procedure applies to the M-shell electrons with β denoting two shells away from a vacancy and α denoting a single shell away from the recombining electron's shell [207]. Figure 3.15 illustrates the procedure for nomenclature.

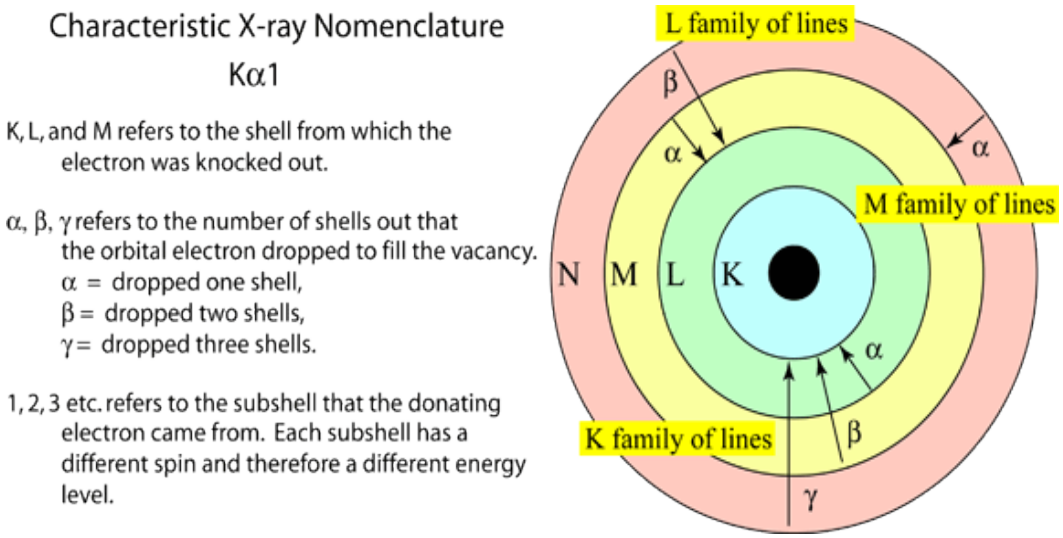


Figure 3.15: Nomenclature procedure for characteristic X-rays classification [235].

Orbital electrons may possess different energies, due to bonding effects, so that the maximum population of such varying electron energy states is given by the number of possible states possessing the relevant principal quantum number [234]. For K-shell, the number is 2, while it is 8 and 18 for L and M shells respectively. The closeness of the two K-shell states, yielding Kα_1 and Kα_2 X-rays, is so significant that it is highly unresolved by an EDS system in such a way that K$\alpha_{1,2}$ doublet is simply regarded as Kα peak with associated energy between the two and a weighted average intensity [236]. Since outer orbits occupying electrons are often not involved directly in this X-ray generation, then it implies that L-K electron transition is most probable than L-M transition due to shell proximity. For this reason, Kα radiation is more intense compared to Kβ radiation and consequently Kβ has higher energy than Kα due to L-M shell separation. It is worthy of note, however, that the closer an electron transition is

to the nucleus of an atom, the higher the energy of its corresponding characteristic X-ray. Thus, the transition energy for Mα radiation is less than that of Lα which in turn is less than that of Kα, i.e. Mα radiation < Lα radiation < Kα radiation.

The minimum energy (so-called critical energy, E_c) required of an incident electron to create a vacancy in the atomic structure of the sample should, preferably, not be more than half of the energy (E_0) of the incident electron in order to attain high excitation efficiency. This energy (E_c) corresponds to the binding energy of electrons in the inner shells and it increases towards the nucleus such that for K, L, and M shells, $E_{c\text{-}K}$ is greater than $E_{c\text{-}L}$ which is, in turn, greater than $E_{c\text{-}M}$. This implies that all incident electron beams of sufficiently enough energies to generate K X-rays will as well excite neighbouring occupied L and M shells to generate L X-rays and M X-rays and, consequently, generating Kα, Kβ, and Kγ lines respectively. It is against this backdrop that some common families of lines for characteristic x-rays are used for spectroscopic peak identification. These lines are often presented in ratios such that for any identified higher energy characteristic X-ray detected in the EDS spectrum, an accompanying nearest possible lower energy characteristic X-ray should exist with counts obtained from the given ratio and depending the shell excited.

Thus

- Kα : Kβ = 10 : 1,
- Lα : Lβ_1 : Lβ_2 : Lγ = 10 : 7 : 2 : 1, and
- Mα : Mβ = 10 : 6 [234].

3.3.6.2 Instrumentation

The EDS system is comprised of three main components; a semiconductor X-ray detector, a pulse processor, and a multiple channel analyzer (MCA). Characteristic X-ray photon, generated via atomic excitation, gets absorbed by the X-ray detector into the semiconductor crystal bulk thereby giving out most of its energy to the process of electron-hole pairs formation [236]. These charge carriers are then swept away by a necessary bias applied between the terminals of the p-i-n (p-type, intrinsic, n-type) Si(Li) crystal to generate a charge pulse and eventually converted into voltage pulse via a preamplifier. The voltage pulse receives further amplification and smoothing by a pulse processor and later transmitted to a multichannel X-ray analyzer. The

multichannel analyzer performs the final data processing and display the spectrum in the form of a histogram of intensity as a function of voltage [2009].

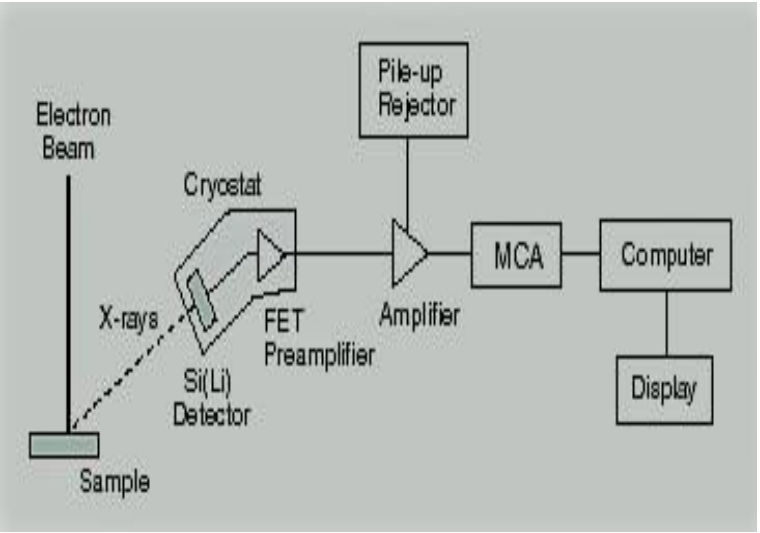


Figure 3.16: Schematic representation of an energy dispersive X-ray spectrometer [226].

Just like most other spectroscopic systems, EDS has some operational constraints. These include amongst others;

1. Energy resolution: Typically, 130 - 150 eV (Full Width Half Maximum) for Mn Kα peak at 5.89 keV,
2. Detection limit: 1000 – 3000 ppm; >10 %. wt,
3. Identifiable elements: Elements heavier than Beryllium up to Uranium (Z = 92),
4. Spatial resolution: For low atomic number elements (up to Z = 35), 1- 5 μm^3 and 0.2 – 1 μm^3 for higher atomic number elements (Z > 35),
5. Precision: Approaching ±1% in close agreement with randomly selected individual measurements,

Accuracy: About ±1 – 2% depending on sample nature and in close agreement between observed and standard reference values [236].

3.3.7 Atomic Force Microscopy

Introduction

Atomic force microscopy (AFM) belongs to a group of imaging techniques, popularly referred to as the scanning probe microscopy, that utilize specially designed microscopes to collect images of a sample surface by moving a probe over the surface in a raster pattern. The images produced are often a measure of the sample's local properties such as height (thickness), friction, magnetism [198], etc. Although, scanning tunnelling microscopy (STM) was the first scanning probe technique developed by G. Binnig and H. Rohrer in 1981, an invention that later earned them a joint Nobel Prize in Physics in 1986 [199], atomic force microscopy is the most commonly used scanning probe technique in the recent. Other techniques in use include the tapping mode atomic force microscopy (TM-AFM), magnetic force microscopy, electric force microscopy (EFM), frictional force microscopy, and near field optical microscopy (NFOM).

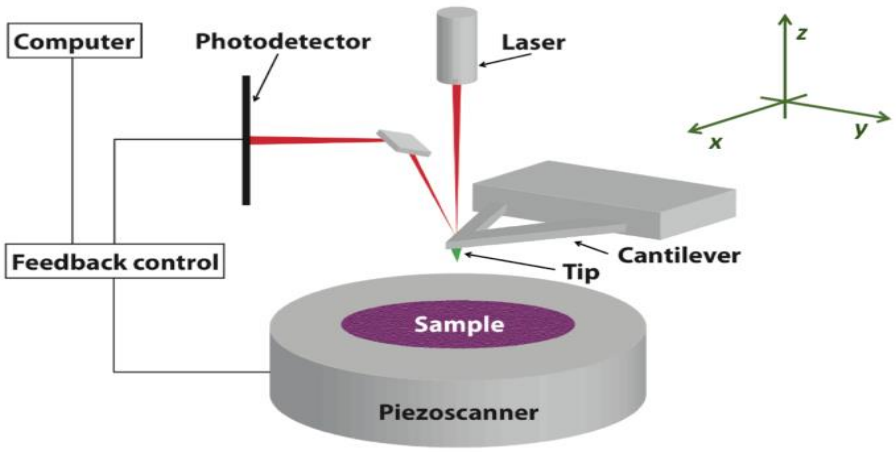


Figure 3.17: Schematic diagram of an atomic force microscope, from [200].

All scanning probe techniques have a small probe, a feedback method or network, and a fine control of the distance between the tip and the sample surface. Various electronic techniques are employed for the feedback loop which, in essence, controls the distance between the tip of the probe and the sample surface. For a very small tip-surface distance, the feedback loop signals a flexible piezo crystal system mounted at the base of the sample holder to contract thereby lowering the sample. The same effect applies for a large tip-surface distance where the sample is raised. An image of the scanned

surface is created by plotting its horizontal and vertical movements as the tip scans across it. The whole process describes how well the feedback loops influences the tip-sample interaction [201].

3.3.7.1 Instrumentation

The atomic force microscope (AFM) uses a silicon or silicon nitride ($\mathbf{Si_3N_4}$) tip mounted on the end of a silicon cantilever spring. It employs a feedback system based on a change in force between the tip and the sample resulting in a shift in the angle of the cantilever as the spring moves. A laser reflecting off over the back of the tip moves up and down the face of a position sensitive photodetector relative to the spring's movement. The feedback loop reacts to any slight change in laser position by sensitively adjusting the height of the sample via the piezo crystal in order to keep the force constant. This process continues until all the sample surface is scanned and the topography image is created from the path of the sample moving up and down while deflection image is produced based on the deflection of the tip. AFM works well for all types of samples utilizing three different modes; contact, non-contact, and dynamic or tapping mode atomic force microscopy. The tapping mode AFM is used for imaging soft samples that could be damaged by the collective effects of the forces present in the AFM procedure and as the name implies, the tip oscillates as the sample is scanned. The change in amplitude of the tip oscillation is utilized as the feedback input signal [241].

In this research, to further probe the surface morphology of the Ag:a-C nanomaterials, a high resolution (sub-nanometer) Veeco Dimension 3100 atomic force microscope situated at the MMU, Wits University, was used to scan the surfaces of the samples.

3.3.8 RF magnetron sputtering

Introduction

This is a deposition process that involves the generation of a gaseous plasma in a vacuum and confining it to a space containing a material (target) to be deposited. The target is positioned at a predetermined distance relative to the substrate such that its

surface is eroded by high-energy ions in the plasma. The resultant liberated atoms travel through the vacuum environment and deposit on the substrate thereby forming a thin film of the target [242].

3.3.8.1 Instrumentation

At the instance of the sputtering process, the working chamber is initially evacuated to high vacuum in order to lessen the effects of partial pressures of all background gases and that of any possible contaminants. Once a suitable base pressure is achieved, a pressure control system is used to flow in a sputtering gas (usually Argon) comprising the plasma into the chamber in order to regulate the total pressure. To initiate the generation of plasma, high voltage is applied between the cathode (behind the sputtering target) and the anode (connected to the chamber as electrical ground). This high voltage will cause electrons in the sputtering gas to be accelerated away from the cathode and triggering collisions with nearby atoms of the sputtering gas. These cascades of collisions cause an electrostatic repulsion that knocks off electrons from the sputtering gas atoms, leading to ionization. Due to the high potential difference, the positive sputter gas atoms get accelerated towards the negatively charged cathode, resulting in high energy collisions with the target surface. Each of these collisions can cause atoms at the surface of the target to be ejected into the vacuum environment with enough kinetic energy to reach the surface of the substrate [243].

It is worthy of note here that sputtering gases with high molecular weight (such as argon or xenon) are chosen in order to facilitate as many high energy collisions in the chamber as possible and to improve deposition rates. Also, in the case of reactive sputtering, where compounds are deposited instead of single atoms, gases such as oxygen or nitrogen are usually introduced into the plasma during film growth. Furthermore, very strong magnets are used in the sputtering source to confine the electrons in the plasma at or near the target surface. This confinement of plasma electrons results in the generation of higher density plasma, increased deposition rates, and prevents any possible damage due to direct impact of the plasma electron with the substrate of growing film. [244]. Magnetron sputter deposition has numerous advantages over other physical vapor deposition techniques. For instance, it allows for the deposition of

nearly all materials regardless of their melting temperatures since it does not require melting or evaporation of the source materials. Also, the deposited films of single atoms, compounds and alloys maintain similar composition as those of the source materials amongst others. Figure 3.18 shows a schematic representation of a typical sputtering system [16].

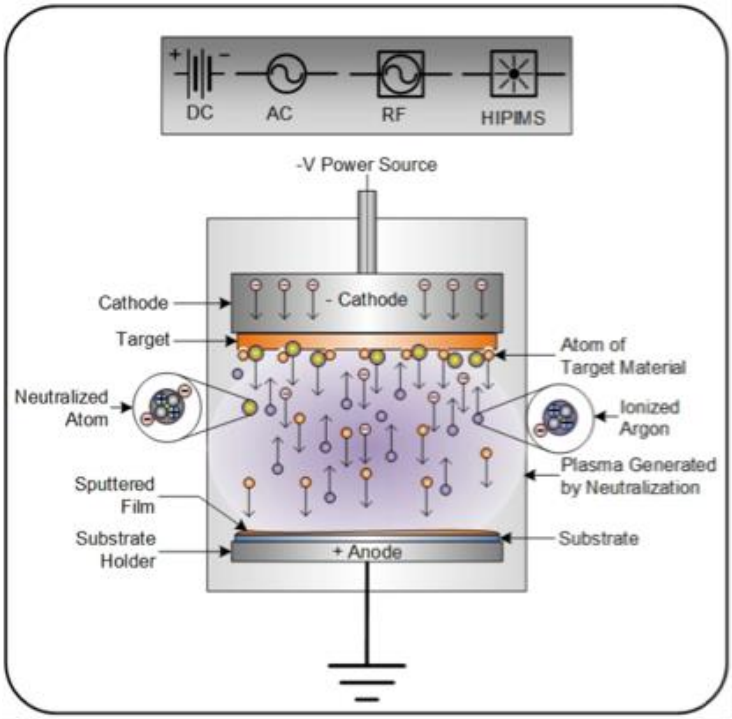


Figure 3.18: Schematic diagram of a typical magnetron sputtering system [16].

A successful magnetron sputtering deposition of thin films and coatings requires the right choice of a power delivery system. Depending on the intended applications, materials can be deposited using DC (direct current), RF (radio frequency), pulsed DC or high power impulse magnetron sputtering (HIPIMS) and the mid frequency (MF) AC sputtering power source. In this research, RF magnetron sputtering technique was utilized due to its wide application in the industry for silicon thin film deposition. It is

extensively used because, compared to other deposition methods, it does not involve chemical interaction between the participating species and can be used to produce good quality silicon thin films [245]. RF magnetron sputtering system alternates the applied electrical potential of the current at radio frequencies in order to avoid possible charge build up. In this way, each phase of the cycle tends to reverse any charge build up when the current flows continuously in one direction thereby increasing the growth rate of the thin film by enhancing the percentage of ionized target atoms [246].

3.3.8.2 Sputtering of silicon (Si) layers

Sections of the Ag:a-C films were carefully floated off the glass substrates (using the same procedure described in sections 3.2.). Each section was captured/mounted on a cleaned indium titanium oxide (ITO) substrate with dimension 2 cm x 1.5 cm and dried at room temperature. Thin layers of Silicon (Si) were deposited directly on each of the Ag:a-C layers using the RF magnetron sputtering set up shown in Figure 3.19.



Figure 3.19: Experimental set up for the RF magnetron sputtering.

The sputtering was made from a pure (99.99%) silicon target (4 inches diameter and 0.25 inches thickness) attached to a balanced magnetron. The samples were mounted on the sample holder attached to the lid of the vacuum chamber. The lid was replaced, and the chamber was evacuated to a pressure ~ 10^{-2} mbar with the aid of an attached rotary pump for about 20 minutes. The vacuum chamber was further evacuated to a

working base pressure of 10^{-5} mbar in order to ensure an oxygen free environment for the plasma to be properly ignited. Argon (Ar) gas was then introduced into the chamber at a flow rate of 25 sccm and the RF power was applied simultaneously which creates a DC voltage between the target and the substrate holder. The silicon target was then pre-sputtered against a blank reference substrate, for about 2 minutes, in order to remove any possible contaminants on its surface. The sputtering process was carried out at room temperature for 138 seconds for each sample in pure argon atmosphere with ~ 13.56 MHz RF power of 175 W. The RF power and Ar source were simultaneously turned off and the system was allowed to cool for about 2 hours and the samples were taken out afterwards.

3.3.9 Photovoltaic potentials of Ag:a-C nanocomposites

The potentials of Ag:a-C nanocomposites for photovoltaic applications were investigated by characterizing their photoconductivity response when incorporated in solar cell systems. This aspect of the research involves two stages;

- A series system with a reference silicon-based photovoltaic cell such that the nanocomposites act as surface antireflection coatings,
- A series system in which the nanocomposites were incorporated as active metallic layers.

3.3.9.1 Ag:a-C nanocomposites as surface antireflection coatings

In this case, a series arrangement of the nanocomposites was made with a silicon-based (non-commercial) photovoltaic cell, whose reference parameters (i.e. short-circuit current, I_{sc} and open-circuit voltage, V_{oc} and efficiency, η) are 0.05 A, 0.55 V and 15.11 respectively. The arrangement was made in such a way that light from the source (radiation) interacts first with the Ag:a-C nanocomposite layers before interacting with the reference device as shown in Figure 3.20.

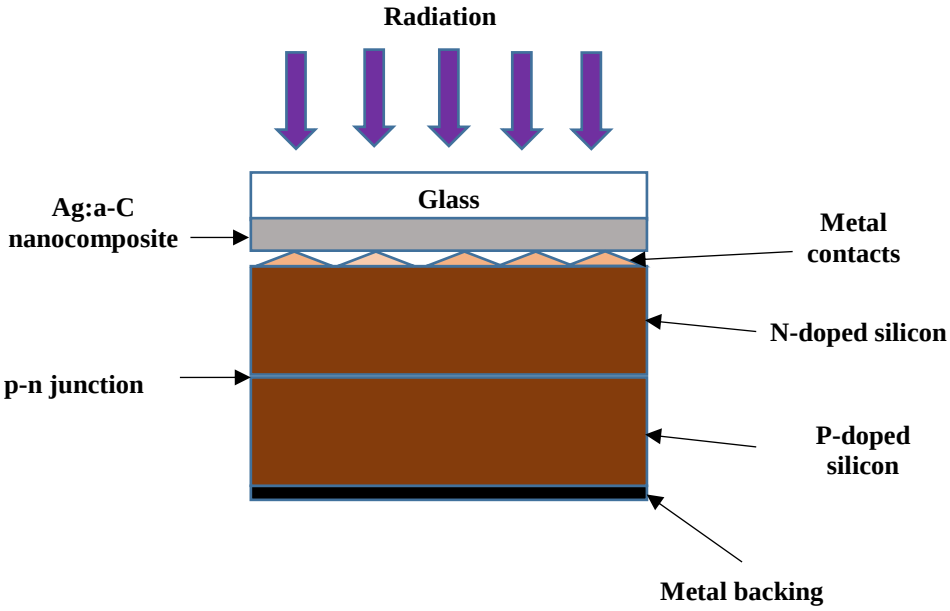


Figure 3.20: Schematic diagram of the Ag:a-C/solar cell system.

Photoconductivity measurements were conducted using a HP 414B Source Measuring Unit (SMU) at the School of Physics, Wits University. The instrument utilizes voltage and current sources with measurement resolutions of ≤ 1 mV and ≤ 1 μA respectively. It is provided with two-point probes that serve as the conducting terminals from the source unit to the processing unit as shown in Figure 3.21.



Figure 3.21: Experimental set up for the photoconductivity measurement.

With the series arrangement mounted in a vertical position, one of the probes was connected to the ITO (cathode) while the other was connected to the metal contact (anode). The system was positioned in line with a convex collimator, using an adjuster, so that light from the source is adequately converged to surface of the nanocomposite carrying glass. Photogenerated signals in form of current (short circuit current, I_{sc}) and voltage (open circuit voltage, V_{oc}) were detected via the probes at the processor unit which was connected to a LabView processing facility. This unit further processes the measured signals and presents them in a graphical representation of short circuit current as a function of open circuit voltage (i.e. I-V characteristic).

3.3.9.2 Ag:a-C nanocomposites as base layers for photovoltaic devices

These Ag:a-C nanocomposites were floated off the glass substrates and captured on clean ITO (Indium titanium oxide) substrates, in a similar procedure described in section 3.2, and allowed to dry at room temperature. 20 nm layers of silicon were sputtered on each sample and subsequently implanted with phosphorous (P^+) to make them n-type materials. Sputtering conditions and procedure for 20 nm Si deposition were highlighted in section 3.4.8 above. 6 keV phosphorous ions (P^+) from a phosphine (PH_3) source at a fluence of 1 x 10^{15} ions/cm^2 were utilized for this implantation. This fluence (1 x 10^{15} ions/cm^2) was selected in order to overpopulate the silicon layer with phosphorous ions. Also due to silicon layer thickness of 20 nm, the P^+ beam energy was chosen to be 6 keV so that the P^+ ions stop within the silicon layer. TRIM simulation of this implantation shows a mean penetration depth of ~ 10 nm (Figure 3.22). For the Si layer of thickness 20 nm, the simulation shows an overwhelming percentage of the P^+ ions stopping within the layer with only a small percentage getting beyond to the Ag:a-C nanocomposite layers. This is a necessary requirement in the fabrication process so that the characteristic properties of the nanocomposite layers are, to larger extent, not distorted.

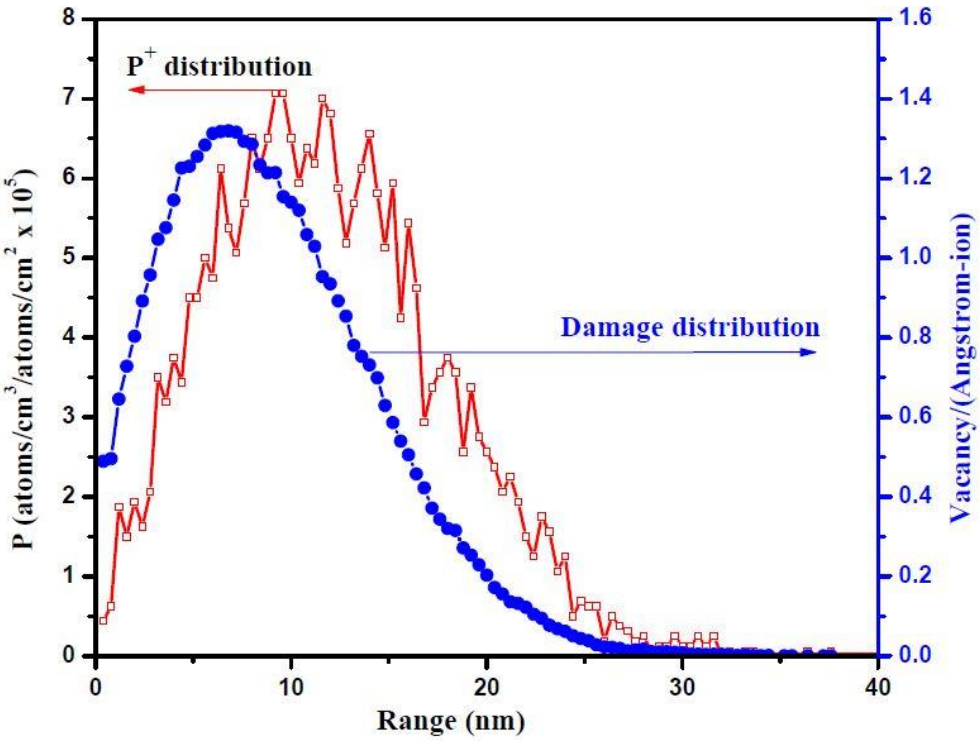


Figure 3.22: TRIM simulation of depth profile and damage distribution for the 6 keV phosphorous ions in a silicon layer.

Hence, a set of metal/semiconductor (n-type silicon) junction devices (Schottky diodes) with Ag:a-C nanocomposites as the base layers were obtained. Metal contacts of appropriate thicknesses were provided on each device by sputtering silver (Ag) on small portions of the silicon layers. This was achieved by masking the silicon containing surfaces with metal sheets provided with appropriate openings of 0.5 cm x 0.5 cm dimensions. A schematic view of these devices is shown in Figure 3.23.

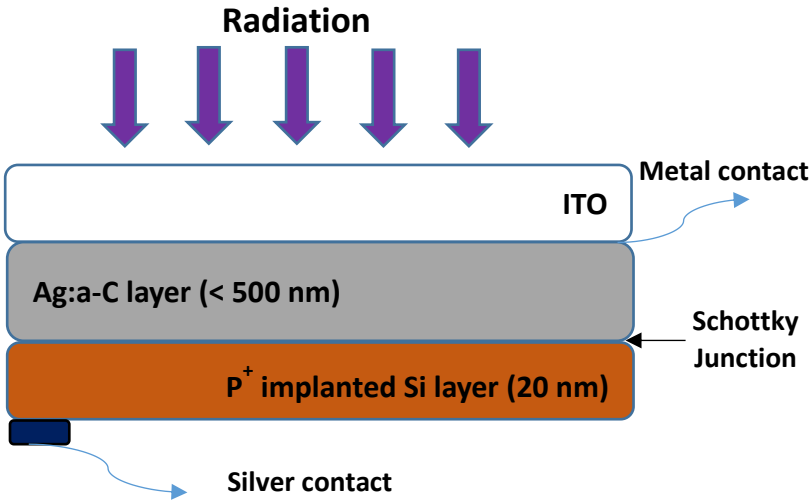


Figure 3.23: Schematic diagram of the Ag-a-C photovoltaic device with the nanocomposite as base (active) layer.

CHAPTER FOUR

4.0 Results and Discussion

4.1 Simulation of ion implantation

Ion-solid interactions are mostly studied in respect of a cascade of collisions that individual energetic implants (ions) undergo while traversing a target material and, more often than not, computer programmes/codes are employed to simulate these interactions with the view to understanding the more likely pattern(s) of interactions prior to the actual implantation procedure. In this research, ion implantation simulations were executed using the SRIM (Stopping and Range of Ions in Matter)-2008 computer package [123]. Implantation parameters given in Table 3.1 were utilized as the essential experimental conditions, governed by predetermined and implantation energy of 25 keV, to simulate the energy loss process. The SRIM simulation package is an extension of TRIM (Transport of Ions in Matter) [79] which is known, as elucidated by Kalish et al. [214], to *"establish a statistical pattern of ionic trajectories as they bombard a material, calculates the collision history of individual ions with the target atoms during the slowing down process and accumulates the created vacancies and interstitials thereby yielding, among others, absolute values of the amount and depth profile of damage caused by the ion implantation to a given dose"* In view of this applicative prowess of SRIM, it then becomes essential to establish adequate pre-implantation insight on the spatial distribution of implants, their final concentration as well as the possible resultant damage incurred by the target material. Room temperature implantation was performed in this research which is applicable with the SRIM simulation package as described by Prawer and Kalish [247]. Figure 4.1 illustrates a SRIM-2008 simulation for detailed calculations with full damage cascades as well as the depth profile due to irradiation of a-C with 25 keV silver ions.

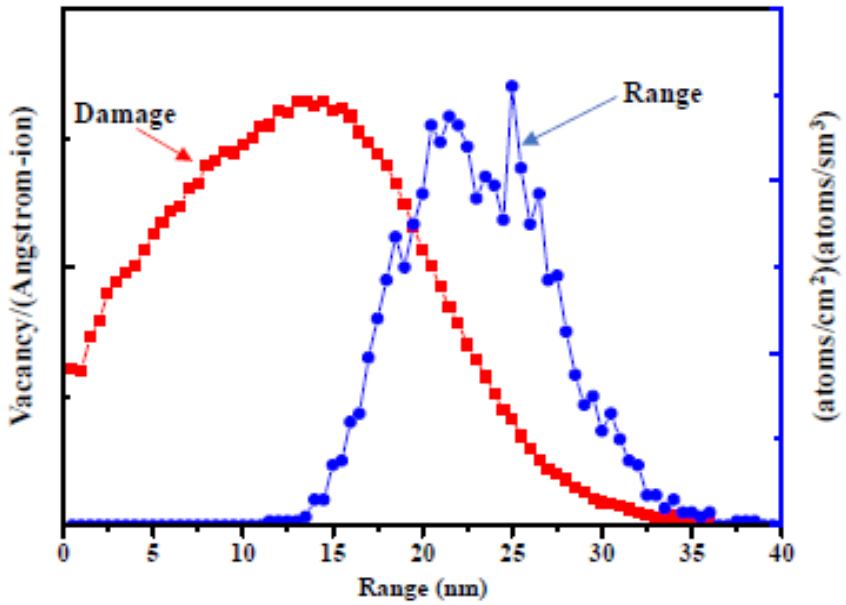


Figure 4.1: Typical SRIM-2008 simulation of depth profile for 25 keV silver ions in a carbon target layer.

The simulation (Figure 4.1) clearly shows a mean penetration depth of ~ 25 nm which is in consonance with the fact that the keV ion implantations used resulted in near-surface phenomena, while MeV implantations lead to damages that are buried well deeper within a few microns thick samples/layers [6]. This is quite attributable to the dependency of ion depth profiles on implantation energies. The electronic (S_e) and nuclear (S_n) energy losses in the carbon matrix for Ag ions at 25 KeV are 2.7 x 10^1 eV/Å and 1.7 x 10^2 eV/Å respectively, as determined from SRIM program [123].

Although the SRIM package is an excellent tool for deriving valuable information on ion-solid interactions, it however overestimates ion concentration and damage while ignoring other important features in the actual implantation process such as; inhomogeneity in atomic distribution of certain materials, channelling effect of ions, recombination of vacancies with interstitials as well as phase formation due to atomic rearrangement [6]. These neglected features, among others, do not influence the interpretation of the results in this study.

4.2 Microstructural studies

In order to gain insight on the microstructural and surface properties of the prepared nanocomposites, Raman spectroscopy, scanning electron microscopy (SEM),

transmission electron microscopy (TEM), atomic force microscopy (AFM) as well as energy dispersive x-ray spectroscopy were employed.

4.3.1 Raman spectroscopy

This characterization technique was employed in order to probe the Raman active vibrational bonding structures present in the Ag:a-C nanocomposites. The technique enables an access to the bond characteristics of the carbon nanocomposites by directly linking the Raman information with sp^2/sp^3 configurations. This is made possible through evaluation of intensity ratios of the D (D for disordered) and G (G for graphite) peaks ($\boldsymbol{I_D/I_G}$), sp^2 cluster size and the full width at half-maximum of the G-peak (FWHM (G)). It also enables the adequate tracing of possible changes in bonding configurations incurred by the pristine carbon films due to Ag irradiation. Figure 4.2 shows the Raman spectra for the pristine amorphous carbon film while Figures 4.3 and 4.4 show the spectra for Ag irradiated amorphous carbon films. The spectra demonstrate such characteristic shapes that are typical of amorphous carbon. The collective scattering responses of the films were deconvoluted to the D-band and G-bands contributions using OriginPro 8.0 "multiple-peaks" Gaussian fits.

The pristine carbon film displayed similar trend of characteristics as those of hydrogen free amorphous carbon materials with D and G peaks around 1360 cm^{-1} and 1554 cm^{-1} respectively. These observed peak positions agree closely with the results obtained by Tuinstra and Koenig [248] in which the 1360 cm^{-1} line was assigned to a scattering, of the first-order by phonon, triggered by disorder as a result of inherent finite crystallite size.

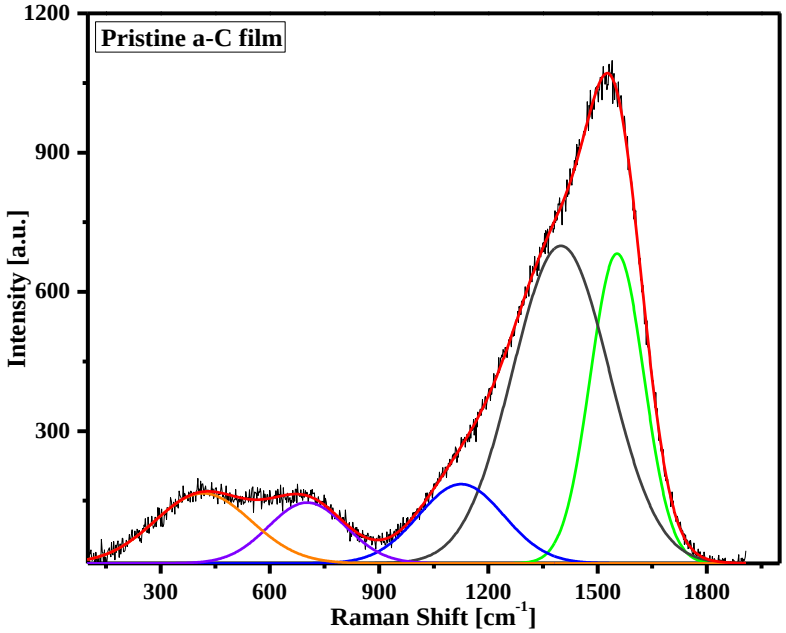


Figure 4.2: Raman fits for the pristine a-C film showing D and G peaks.

Similar Raman studies on a-C material but at different experimental conditions revealed the same trend and referring to the 1360 cm^{-1} mode as the D peak [20 , 233, 244]. The 1573 cm^{-1} line, corresponding to the 1575 cm^{-1} in the work of Tuinstra and Koenig [248], is typically referred to as the G peak commonly attributed to Raman active mode of a graphite-like amorphous carbon [245, 246]. Ferrari and Robertson [253] added that the D peak (~ 1360 cm^{-1}) represents a breathing mode, involving phonons, that is only active in carbon films with relative disorder and which is completely absent in perfect graphite materials. Furthermore, the observed Raman peak at about 1120 cm^{-1} indicates a reasonable presence of sp^3 bonds in the pristine a-C films. This is evident from the observations that UV Raman spectroscopy on some carbon based materials, like fullerene deposited films, describes a strong correlation between the 1100 cm^{-1} band and sp^3-like bonds [254]. Other visible peaks around 400 cm^{-1} and 700 cm^{-1} can be related to oxide shells of silicon resulting from the dominant silicon phase of the supporting glass substrate [253].

Normally, the Raman peaks (D and G) bear distinct information on the microstructural activities in the films such that the D peak arises as a result of the vibration of sp^2 rings while the resonance of the organized sp^2 atoms is due to the G peak. This has empirically revealed useful information about the clustering of sp^2 sites and consequently the relative effect of the cluster size on the optical band gap of the films. In hydrogenated amorphous carbon (a-C:H) films, where the presence of hydrogen widens the optical band gap [248], higher ratios of D and G peak intensities denote a reasonable increase in sp^2 clustering [250]. This is in clear contrast to our preliminary investigation on the Ag irradiated carbon films which shows that increasing fluence of irradiation reduces the overall optical band gap of the materials (details of band gap evaluation are given in section 4.4 under subsection 4.4.1).

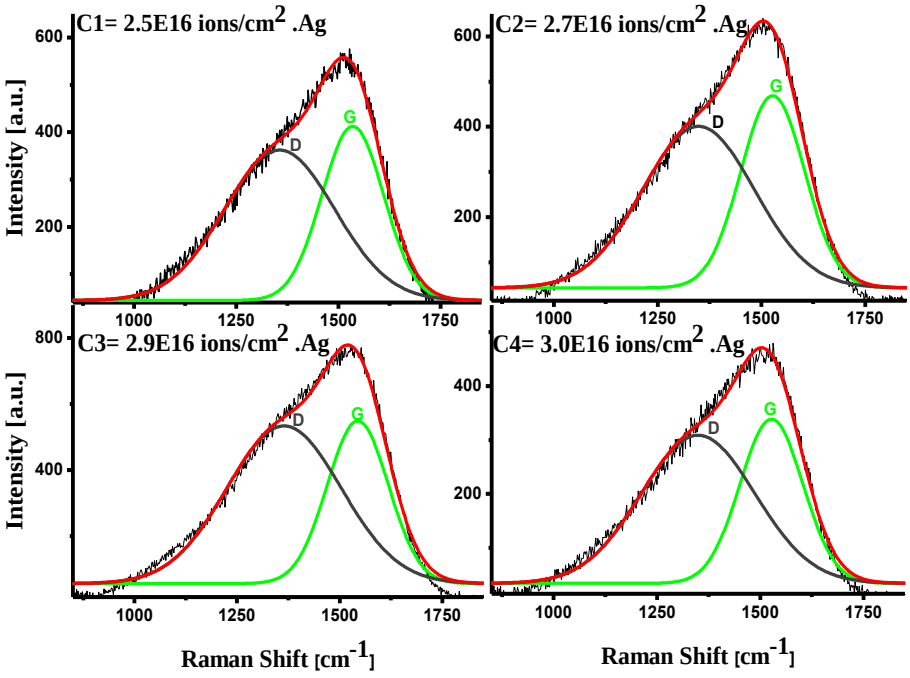


Figure 4.3: Raman fits for lower fluence Ag:a-C nanocomposites (i.e. C1-C4) showing gradual variations in the D and G peaks' positions, intensities and widths with increasing fluence of Ag nanoparticles.

As can be seen from Figure 4.3, the Raman shifts in G peak positions from 1535 cm^{-1} to 1540 cm^{-1} across the lower fluence samples (C1 to C4) as well as the proportionate increase in the peak intensity ratios, indicate higher sp^2 clustering due to aggregation

of Ag nanoparticles. A similar trend of G peak shift, 1550 cm^{-1} to 1557 cm^{-1}, was observed for higher fluence samples (C5 and C6) shown in Figure 4.4.

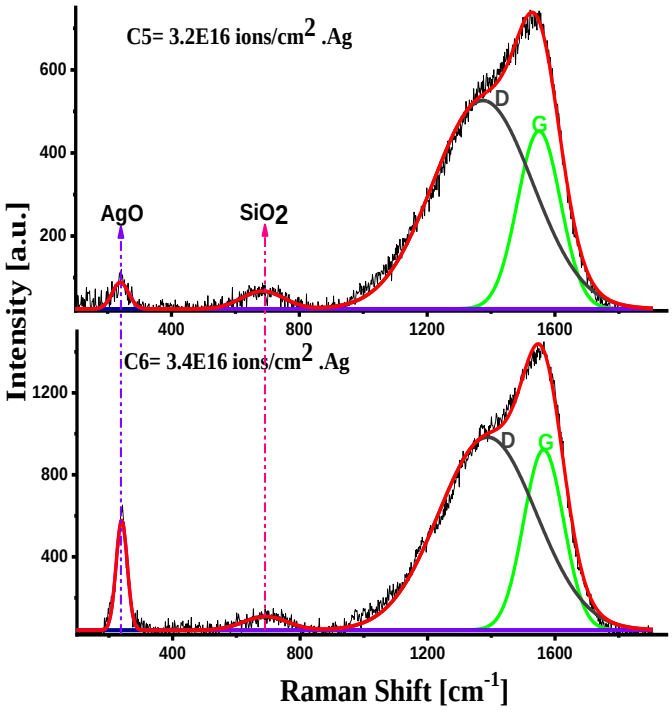


Figure 4.4: Raman fits for higher fluence Ag:a-C nanocomposites (i.e. films containing 3.2 and 3.4 x 10^{16} ions/cm^2 of Ag nanoparticles) showing similar variations with the lower fluence sample but with emerging AgO and SiO_2 phases due to Ag tarnishing and supporting glass substrate respectively.

The FWHM of the G Peak probes structural disorder in the films due to sp^2 clustering with the amorphous structure of the material [247, 249] such that the observed increase in the FWHM(G) values denote gradual modification of the samples by exhibiting less unstrained sp^2 sites clustering. This increase in FWHM (G) with increasing fluence suggests a gradual increase in the structural disorder of the nanocomposites due to Ag introduction as graphitization sets in. Our results quite agree with those obtained by Wu et al. [257] for pristine and Ag containing amorphous carbon at lower fluence up

to 2.9 x 10^{16} ions/cm^{-2} (C1-C3). However, a decrease in FWHM was observed for higher fluence nanocomposites (C4-C6) implying a structural ordering. This may be related to the carbon phase structurally around the larger silver aggregates.

Moreover, the dispersive nature of the D mode in relation to increase in photon excitation energy speaks exclusively well about the crystallite size for a perfect graphite material [251]. This claim is strongly supported by a model proposed by Tuinstra and Koenig [248] relating the ratio of D-G peak intensities to the crystallite size. According to their findings, the intensity ratio varies inversely with the crystallite size $\boldsymbol{L_a}$, determined from x-ray analysis, in such a way that

$$\frac{\boldsymbol{I_D}}{\boldsymbol{I_G}} \propto \frac{\mathbf{1}}{\boldsymbol{L_a}} \qquad (4.1)$$

This relation (4.1) holds well for graphite-like carbon films but its validity for amorphous carbon films has, up to the mid-1990s, not been proven [216]. However, Ferrari and Robertson [256] later related $\boldsymbol{L_a}$ with sp^2 cluster size of amorphous carbon films. In their submission, the intensity ratio was evaluated in terms of cluster size at specific wavelength (λ = 515.5 nm) of the argon ion laser, such that

$$\frac{\boldsymbol{I_D}}{\boldsymbol{I_G}} = \frac{\boldsymbol{C(\lambda)}}{\boldsymbol{L_a}} \qquad (4.2)$$

where C($\boldsymbol{\lambda}$ = 515.5 nm) ≈ 44 Å [258].

Equation 4.2 was used to determine the sp^2 cluster sizes (cluster diameters) for the respective samples in relation to varying fluence of Ag nanoparticles so as to ascertain the possible microstructural modifications due to irradiation. It was observed that sp^2 cluster size increases with increase in the peak intensity ratios at lower fluences of Ag irradiation (up to C4) and decreases afterwards. This can be attributed to the relative ordering influence by the higher fluences of Ag ions. In addition to the calculated cluster size values, other essential measurements relating to G peak position, peak intensity as well as the intensity ratios of D over G peaks ($\boldsymbol{I_D/I_G}$) and FWHM of the G Peak were extracted from respective fittings and the results presented in Table 4.1.

An important point of note here is that the excitation wavelength utilized by Ferrari and Robertson [256] in the model (Equation 4.2) was 515.5 nm as against a wavelength of 514.5 nm in this work. However, enough experimental evidences have shown that there

is minimal effect of excitation wavelength on the peak intensity ratios of carbon films [252, 253].

Table 4.1: Summary of some structural fingerprints of pristine and Ag irradiated amorphous carbon films extracted from Raman spectra.

Samples	**G-peak position (cm^{-1})**	**D-peak intensity I_D (cm^{-1})**	**G-peak intensity I_G (cm^{-1})**	**Peak intensity ratio (I_D/I_G)**	**FWHM(G) (cm^{-1})**	**Cluster size, L_a (nm)**
Pristine	1554	684.20	667.35	1.025	147.26	4.29
C1	1535	317.75	367.56	0.864	151.10	5.09
C2	1531	357.50	404.97	0.883	154.15	4.98
C3	1544	477.73	492.64	0.970	155.10	4.54
C4	1540	298.49	303.92	0.940	157.02	4.48
C5	1550	501.76	428.25	1.712	134.54	2.57
C6	1557	930.12	894.89	1.039	125.93	4.24

Against the back drop of this discussion, we can put forward the following conclusion;

- The unirradiated films had a generally amorphous phase involving a reasonable amount of graphitic micro grains.
- Upon irradiation, a relative disorder was observed in the films as reflected in the growth of D-bands and as shown by the Raman spectra. This characteristic disorder is in agreement with those observed by [212, 247, 249, 254].
- Ag irradiation of the a-C has increased the FWHM of the G band appreciably with increasing fluence up to C4 and decreased thereafter. This trend is correspondingly accompanied by relative decrease in sp^2 cluster size, which is highly pronounced in C5, and then gradually increases at C6.
- At lower fluence of implantation of up to 3.0 x 10^{16} ions/cm^{-2} (i.e. samples C1 to C4), the Ag nanoparticles are well embedded within the amorphous carbon films such that no interactions, due to impurity atoms in the atmosphere or otherwise, are possible other than the ion-solid interaction within the carbon matrix.

- At higher fluence of 3.2 – 3.4 x 10^{16} ions/cm^{-2} (i.e. samples C5 and C6) however, adequate particle aggregation has taken place so that the surface and near surface Ag nanoparticles had possibly form oxides due to exposure to oxygen atoms in the environment. This oxygen effect on exposed silver is called "tarnishing".
- Relating the above claim with the Raman spectra, the observed Raman bands around ~ 230 cm^{-1} and ~ 240 cm^{-1} for samples C5 and C6 (Figure 4.4) are attributed to the vibrational modes of Ag in the surface and near surface silver oxide (AgO) phase of the Ag:a-C nanocomposites. This is in concordance with the findings [255] that prior to dispersing a Rhodamine 6G dye solution on a pure silver oxide film surface, all observed bands between 200 – 400 cm^{-1} for the pristine AgO thin film are due to vibrational modes of silver and oxygen in the silver oxide (AgO) phase of the material. Débarre et al. [263], while reporting on the chemical activity observed on silver colloids synthesized for Surface Enhanced Raman Scattering (SERS), also confirmed the presence of vibrational bands at 230 cm^{-1} in various concentrations of EthyleneDiamineTetraAcetic (EDTA) acid indicating the position of silver oxide mode.

4.2.2 Scanning electron microscopy (SEM)

SEM images were acquired, using the set up described in section 3.3.4, at 14.5 kV energy and at 10 mm working distance for the surfaces of pristine amorphous carbon film and respective Ag:a-C nanocomposites. The images are presented in Figures 4.5 and 4.6 respectively.

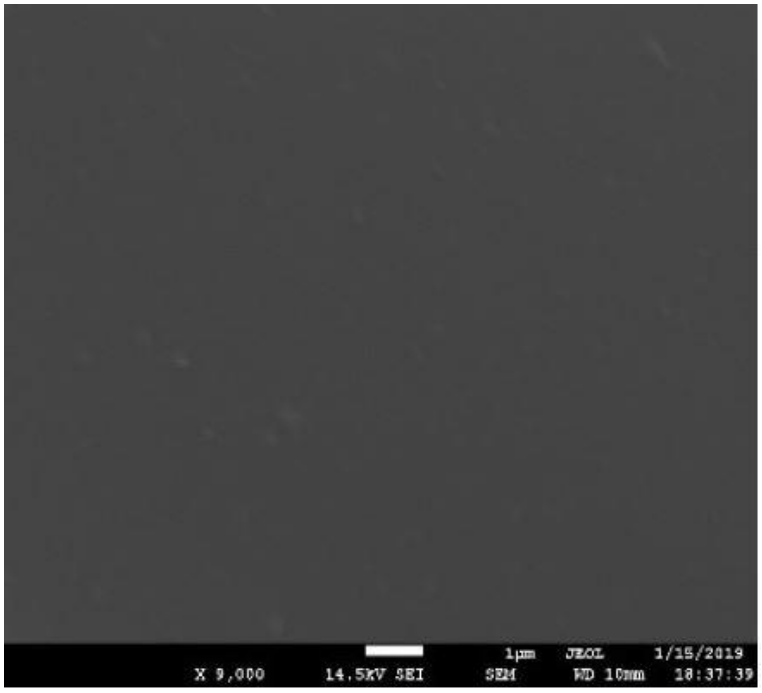


Figure 4.5: SEM image of pristine a-C thin film on glass substrate.

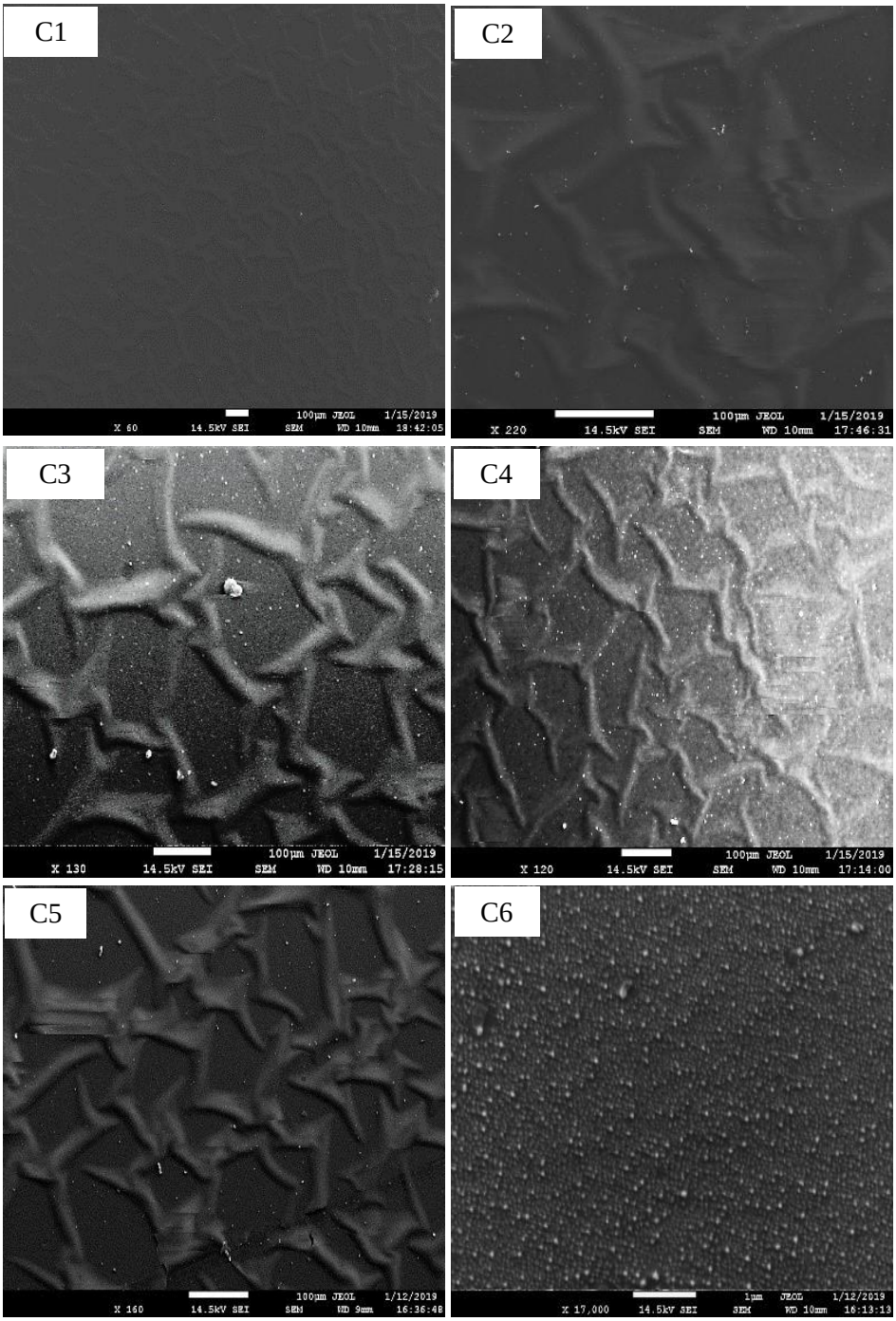


Figure 4.6: SEM images of a-C thin films irradiated with 25 keV Ag with 2.5 to 3.4 × 10^{16} ions/cm^2 fluences.

A smooth and featureless surface was observed for the pristine amorphous carbon thin film (Figure 4.5) at a magnification of 9 000 times. However, films irradiated with fluence (2.5-3.0 x 10^{16} ions/cm^2) of Ag nanoparticles (i.e. C1-C3), observed at varying magnifications (up to 18 000 times), show a change in surface topology. This is

attributed to the fact that the Ag ions are well embedded within the amorphous carbon matrix as shown by Raman analysis. Increased surface roughness becomes evident in films with higher fluence (3.0-3.4 x 10^{16} ions/cm^2) of Ag nanoparticles such that the surface topography is characterized by well patterned hillocks-like structures (i.e. C4-C6). These observed changes in surface topography could be attributed to the increased concentration of Ag nanoparticles (particle agglomeration) and the silver oxide (AgO) phase formed on the films' surfaces, due to silver tarnishing, as evident from Raman analysis. Furthermore, the agglomerated silver nanoparticles form sphere-like shapes which are uniformly distributed within the host amorphous carbon films. The scanned surface images show uniform increase in average particle diameters in the range from ~ 5 nm to ~ 20 nm with increasing fluence which are homogenously dispersed in a similar trend of inter-particle spacings.

4.2.3 Transmission electron microscopy (TEM)

The internal structures of the Ag embedded amorphous carbon films were studied using the TEM set up described in section 3.3.5. TEM micrographs for the respective nanocomposites were acquired at an accelerating voltage of 120 keV and presented in Figure 4.7 below.

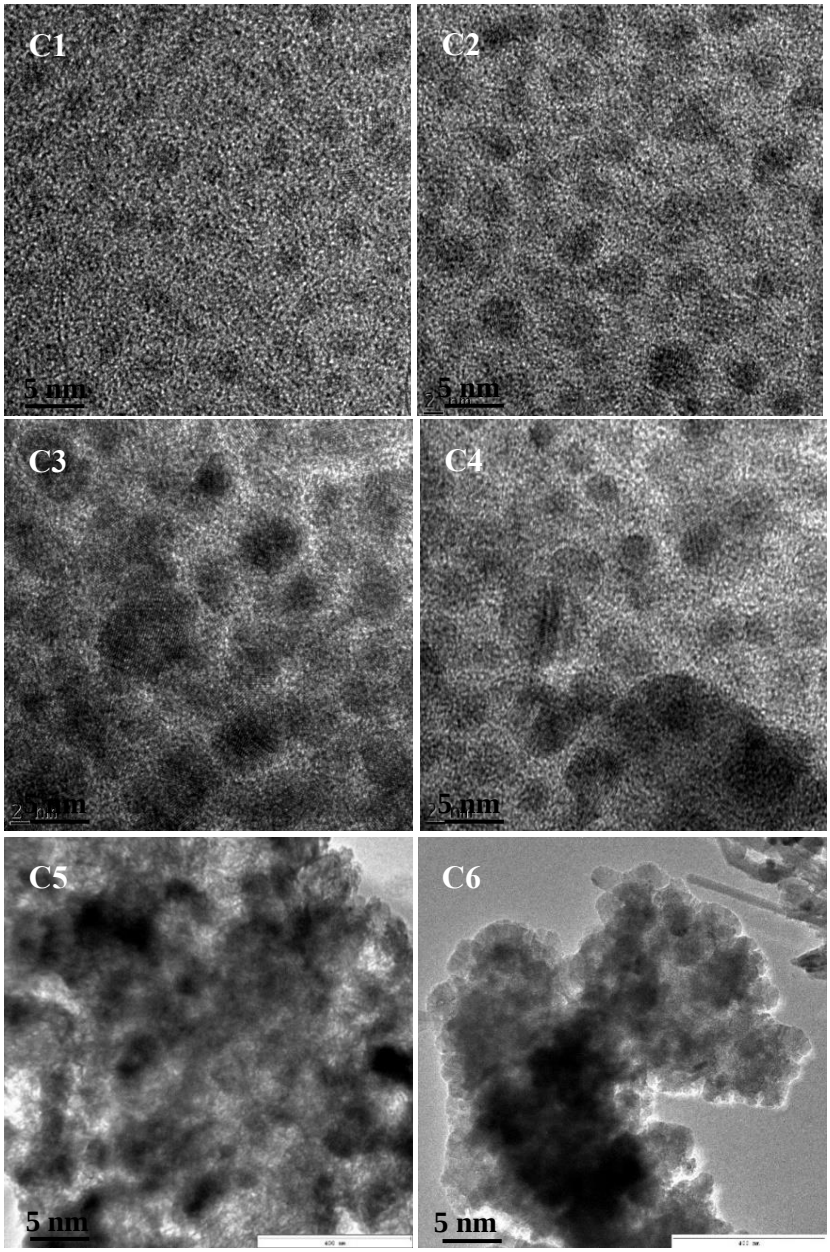


Figure 4.7: Bright mode TEM micrographs of Ag:a-C thin films with varying fluence (2.5 x 10^{16} ions/cm^2 to 3.4 x 10^{16} ions/cm^2) for samples C1 to C6.

The TEM images for the implanted films show increase in particle density and particle size as functions of implantation fluence. For higher Ag fluence (i.e. samples C5 and C6), the Ag nanoparticles agglomerated (particle aggregation). It is further revealed in the TEM micrographs that there are many silver-rich micro grains in the non-reactive phase of the Ag:a-C nanocomposites. It is particularly noted that the Ag grain size area became more pronounced and relatively larger with increasing fluence of irradiation. These silver-rich grains induced graphite-like microstructures as confirmed earlier in

Raman analysis. Furthermore, variations in the images for samples C5 and C6, could be attributed to the surface formation of the silver oxide phase, due to oxidation, also confirmed by Raman analysis.

4.2.4 Atomic force microscopy (AFM)

2D AFM images of the pristine a-C thin film (at 500 nm scan scale) and the 25 keV Ag ion irradiated a-C thin films are shown in Figure 4.8 and Figure 4.9 respectively.

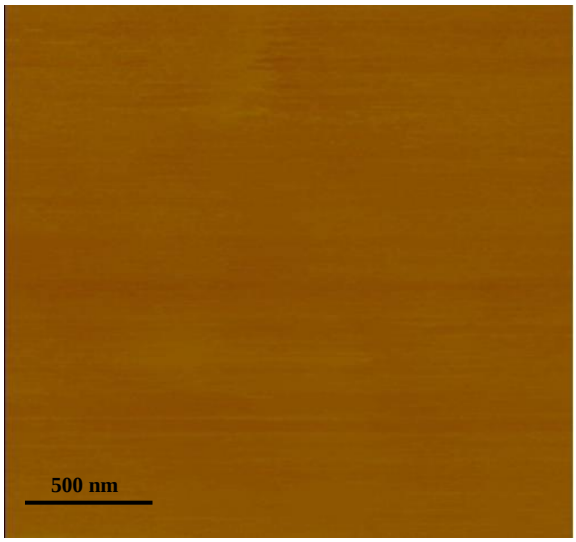


Figure 4.8: 2D AFM image of pristine a-C thin film.

It can clearly be seen from Figure 4.9 (C1 to C6) that grain size and surface roughness of respective samples increase with increasing fluence of irradiation. The gradual increment in roughness is attributed to sputtering effect on the surfaces of the films due to energetic ion bombardment thereby adversely distorting the relative smoothness of the pristine sample surface. Although, surface sputtering due to high fluence leads to increase in roughness, it is observed that for samples irradiated with higher fluence (> 3.0 x 10^{16} ions/cm^2), the roughness is equally influenced by the agglomeration of Ag nanoparticles. This is in good agreement with the observations by Sharma et al. [264].

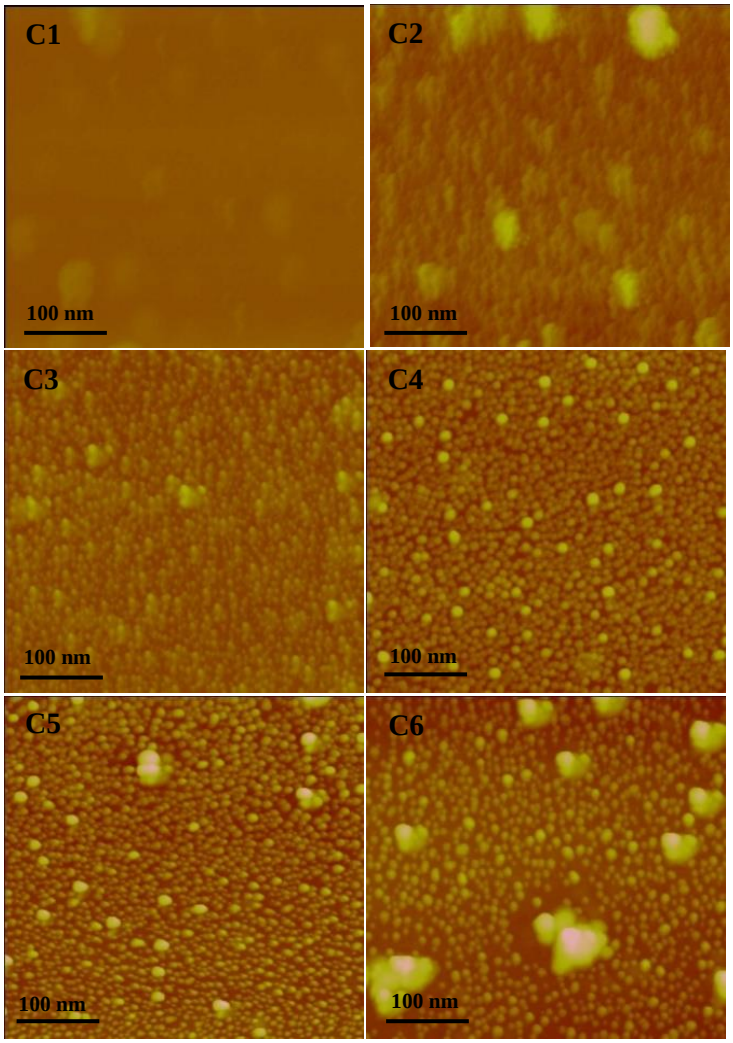


Figure 4.9: 2D AFM image of 25 keV ion irradiated a-C thin films with varying fluence.

Furthermore, the AFM built-in facility was used to conduct sectioning analysis to determine the thickness of the pristine carbon film. This analysis utilizes a cross-sectional probe of the film. Surface image of an already scanned pristine film was considered such that the elevation of the cantilever on the film, with respect to the glass substrate, is recorded. Corresponding thickness values for the film were recorded and an average thickness value ~ 500 nm (499.98 nm) was determined. Irradiation with ions of heavy metals like Ag is prone to cause severe surface sputtering of the target. As such, reduction in the thickness of the amorphous carbon thin film is inevitable. Using the same software, It was also observed that average grain size increases from ~ 5 nm for film with lowest fluence of 2.5×10^{16} ions/cm^2 to ~ 21 nm for the film with highest fluence of 3.4×10^{16} ions/cm^2. This grain size increase is attributed to the

particle agglomeration that has taken place as a result of increased Ag ion concentration in the a-C matrix. Due to the high surface free energy of the smaller grains (high specific surface area) in the non-reactive phase of Ag:a-C nanocomposites, there is much tendency for grain agglomeration forming larger grains with lower surface free energy (low specific surface area) [258-261]. Comparative roughness for pristine and Ag irradiated a-C thin films is shown in Figure 4.10.

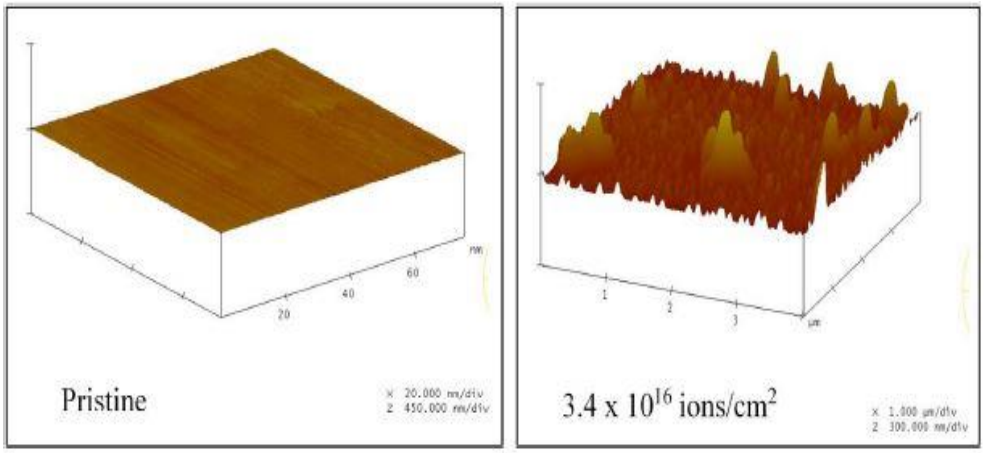


Figure 4.10: Surface roughness for pristine and Ag irradiated a-C thin films.

Surface roughness, average particle diameter as well as average grain size values for the respective samples were deduced and presented in Table 4.2.

Table 4.2: Summary of particle dimensions as determined from SEM and AFM analyses.

Fluence (ions/cm^2)	**Average particle diameter (nm) by SEM analysis**	**Average grain size (nm) by AFM analysis**	**Roughness (nm)**
Pristine	-	-	1.76
2.5 x 10^{16}	6 ± 0.1	5 ± 0.5	2.06
2.7 x 10^{16}	8 ± 0.2	7 ± 0.3	2.15
2.9 x 10^{16}	11 ± 0.2	9 ± 0.1	3.46
3.0 x 10^{16}	12 ± 0.3	12 ± 0.1	3.98
3.2 x 10^{16}	15 ± 0.2	17 ± 0.2	4.57
3.4 x 10^{16}	20 ± 0.5	21 ± 0.7	4.92

4.2.5 Energy dispersive x-ray spectroscopy (EDS)

In order to further confirm the material compositions of the nanocomposites as well as the increased presence of oxygen, energy dispersive X-ray spectroscopy (EDS) was carried out using an Oxford X-act EDS detector on the sample with the highest fluence of Ag ions. The selection was based on the observations, from both Raman analysis and transmission electron microscopy, of some build ups of silver oxide (AgO) phase in the materials with higher fluence (i.e. C5 and C6).

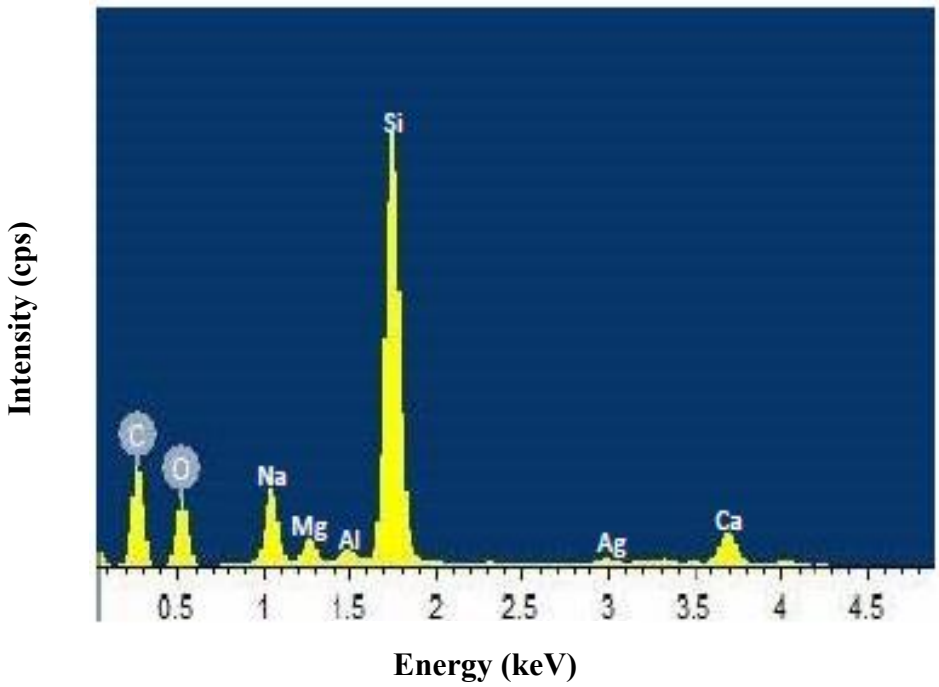


Figure 4.11: EDS spectra for Ag:a-C nanocomposite at a fluence of 3.4 x 10^{16} ions/cm^2 (sample C6).

The EDS spectrum in Figure 4.11 exhibited the presence of oxygen in addition to dominant carbon phase. Traces of sodium (Na), magnesium (Mg), aluminium (Al) and calcium (Ca) were also detected at low atomic percentages, due to electrons' interaction with the SEM metal stub. A significant presence of silicon (Si) was detected which is attributed to dominant SiO_2 phase of the supporting glass substrate. The presence of oxygen is attributed partly to the SiO_2 phase of the substrate and partly to the tarnishing effect of the atmospheric oxygen on silver at the surfaces of Ag:a-C nanocomposites with higher fluence (i.e. AgO phase observed in both Raman and TEM).

4.3 UV-visible absorption spectroscopy

One of the known facts about amorphous materials is the change that occurs, in terms of optical response, when nanoparticles are incorporated in their pure matrix since their environment is neither inert nor isotropic. Thus, exposing these anisotropic materials to electromagnetic radiation leads to resonant coupling between light photons and the collective modes due to electronic transitions/excitations in the material. The interaction of the UV-visible component of the electromagnetic spectrum with such nanomaterials gives rise to polarization in the material in form of variation in the magnitude of absorption or transmission with respect to changes in wavelengths [262].

In this research, absorption spectrum for pristine carbon film shows reasonable transmission of light in the infrared and near infrared regions of the spectrum (~ 27%) but displays outright absorption within the visible region (Figure 4.12). The recorded absorption could be attributed to the film's density (40 μgcm^{-2}) and antireflection property; a major requirement for its candidature in the present context.

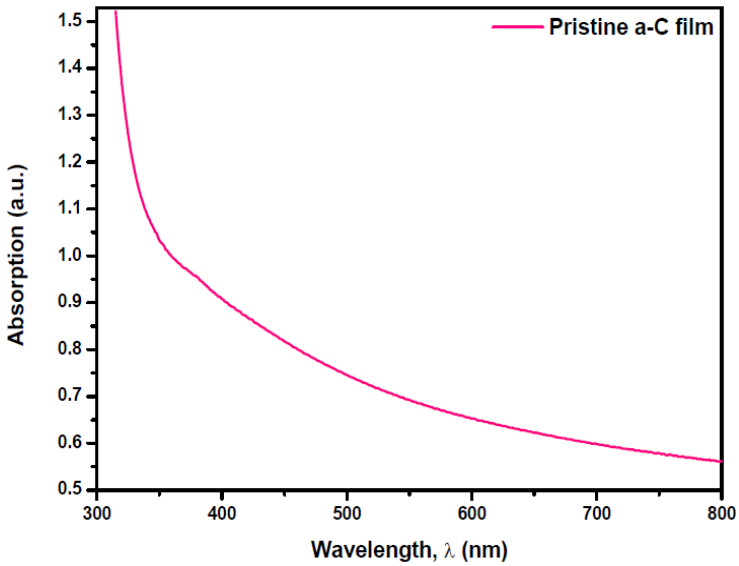


Figure 4.12: Optical absorption spectrum of stand-alone pristine a-C film.

As a matter of reference, Ag ions were implanted on plain glass substrate using the same method described earlier. The spectrum shows appreciable light absorption in the visible and near UV regions with a clear surface plasmon resonance (SPR) peak at a wavelength of about 427.8 nm as shown in Figure 4.13. This is in close agreement with the observation, 428 nm, by Lee et al. [263].

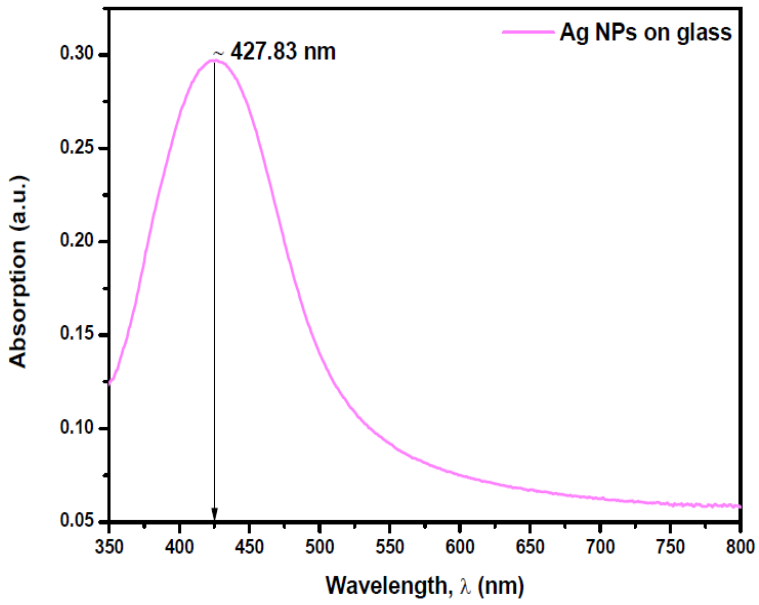


Figure 4.13: Optical absorption of Ag nanoparticles on glass substrate.

The optical absorption of Ag implanted amorphous carbon (Ag:a-C) thin films was observed to proportionately increase in the visible and near infrared regions with increase in the dose of Ag nanoparticles until maximum absorptions were attained in the visible region near the onset of ultraviolet. Figure 4.14 shows the combined absorption spectra for the Ag:a-C nanocomposites analysed as free standing films.

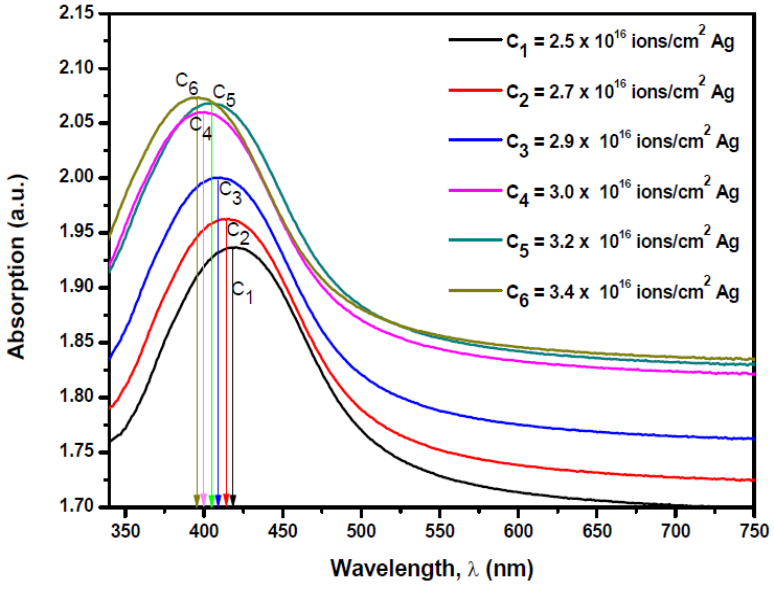


Figure 4.14: Optical absorption spectra of Ag:a-C nanocomposites.

These rapid increases as well as the clearly observed absorption peaks are attributed to the surface plasmon resonance (SPR) of Ag nanoparticles embedded in the amorphous carbon matrix. The intense and sharp plasmonic resonance responses of the carbon nanomaterials occur as a result of the variations in the inherent dielectric properties of amorphous carbon leading to small overlaps between the localized SPR of the Ag NPs and their interband transitions that usually start at a wavelength of about 320 nm [271]. In a related work to study the microstructural modifications of thin films induced by swift heavy ion irradiation, Singhal et al., [9] recorded similar shifts and broadenings of SPR peaks for atom beam sputtered amorphous carbon irradiated with high energy (120 MeV) but low fluence (~ 10^{13} ions/cm^2) of Ag ions. They attributed these to large size distribution (so-called particle aggregation) of the Ag nanoparticles in the amorphous carbon matrix. In addition to particle size effect, the partial absorption of the amorphous carbon films could have been overridden by the metallic SPR peak due to the relatively significant concentration (by fluence) of the Ag ions in the system which, according to McLellan [272], is considerably beyond the solubility limit of Ag in carbon. Also according to Yaremchuk et al. [133], the interaction energy is capable of changing the geometry of the Ag implants leading to a reasonable change in their dielectric properties and consequently the particulate surface plasmon resonance wavelength.

In this study, particle aggregation is mainly due to low energy (25 keV) and high fluence (~ 10^{16} ions/cm^2) of Ag ions. The particles sizes increase with increasing fluence thereby decreasing the inter-particle spacing. This decrease in spacing increases the frequency of the electromagnetic emission and consequently decreasing the wavelength [273]. This phenomenon is termed “blue shifting” in surface plasmon resonance peaks of metallic nanoparticles. Furthermore, the particle size/morphology dependence of the SPR peak positions for Ag nanoparticles have been extensively discussed in some detailed and independent theoretical works on metallic particles’ symmetry [264, 267, 268]. These works have shown that for uniformly distributed particles, sharply pronounced SPR peaks dominated the optical spectra while broadened peaks with less intensity are prevalent for particles with inconsistent symmetry. Here, the observed fluence-influenced SPR peaks for Ag irradiated carbon films are centered within 396 nm to 418 nm wavelengths for the various implantation

fluence. Figure 4.15 depicts a fluence dependence graph of the SPR peaks shifting for the Ag implanted samples and a summary of this dependency is presented in Table 4.3.

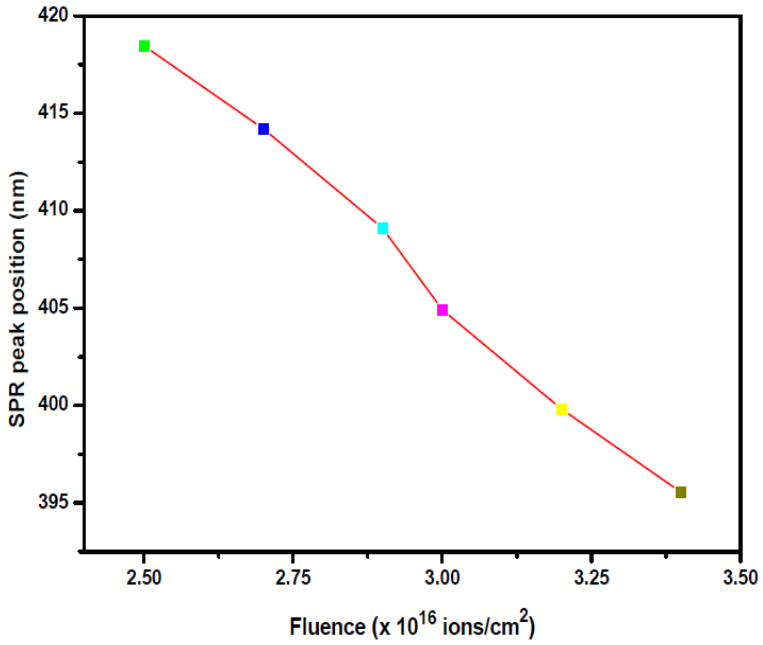


Figure 4.15: Fluence dependence of the SPR peak shifting.

Table 4.3: Variation of SPR peak values with irradiation fluence.

s/n	Sample	Fluence, ϕ (x10^{16} ions/cm^2)	SPR peak position (nm)
1	C1	2.5	418.5
2	C2	2.7	414.2
3	C3	2.9	409.1
4	C4	3.0	399.8
5	C5	3.2	404.9
6	C6	3.4	395.7

4.3.1 Optical band gap

The determination of the optical band gap energy (E_g), as an essential requirement in corroborating the application prospects of the prepared Ag:a-C nanocomposites, was possible via a critical spectral analysis of the material in a region within the vicinity of its fundamental absorption edge. This region, which was identified from a rapid

increase in the magnitude of the absorption coefficient measured as a function of material optical density per unit path length or thickness [180], plays a central role in this analysis as it defines the indirect interband electronic transitions in the materials.

According to Tauc's relation, explained earlier in section 2.6.3 and given by Equation 2.24, the absorption energy ($\boldsymbol{\alpha}$) for both direct and indirect transitions is a function of the incident photon energy ($\boldsymbol{h\upsilon}$). Against the backdrop of this inter-relation, the optical band gaps of the pristine and irradiated amorphous carbon films were determined by extrapolating the linear portions (linear fitting) of $(\boldsymbol{\alpha h\upsilon})^{\frac{1}{2}}$ versus $\boldsymbol{h\upsilon}$ plots to the photon energy axis. Optical band gap energy obtained for the pristine carbon film was 1.79 eV as shown in Figure 4.16.

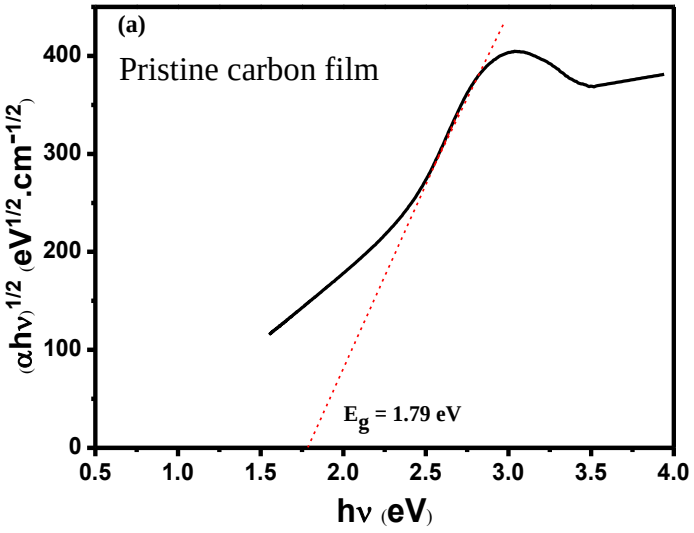


Figure 4.16: Tauc's plot of $(\boldsymbol{\alpha h\upsilon})^{\frac{1}{2}}$ as a function of photon ($\boldsymbol{h\upsilon}$) energy for pristine a-C film.

The Tauc curves for the various samples exemplified those of typical amorphous carbon materials showing evidence of high absorption, due to doping, in the visible region. This is in good agreement with the findings, by Duley [276], that there is absence of hydrogen in the amorphous carbon samples. Extrapolated optical band gap values had evidently confirmed the above findings because one of the major effects of hydrogen is increasing the band gap energy ($\boldsymbol{E_g}$) while reducing optical absorption at lower photon energies [248]. A totally opposite effect was observed in this work.

Figure 4.17 shows the Tauc's plots indicating, clearly, the extrapolated optical band gap values for varying fluence in the respective nanomaterials.

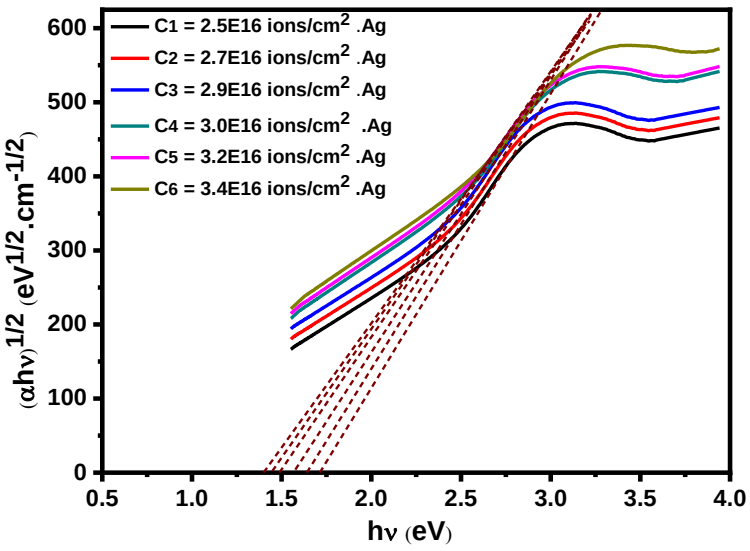


Figure 4.17: Tauc's plot of $(\boldsymbol{\alpha h\nu})^{\frac{1}{2}}$ as function of photon ($\boldsymbol{h\nu}$) energy for the various Ag implanted a-C nanomaterials.

The figures show significant decrease in the optical band gaps from 1.71 eV to 1.41 eV respectively. A similar trend (i.e. red shift of optical band gap) has been previously reported [136] for sp^3-rich amorphous carbon films doped with varying concentrations of Ag nanoparticles during deposition; optical bang gap decreased from 2.55 eV to 1.95 eV. For the fact that silver does not react with carbon (i.e. it is non carbide forming) [30], we do not expect our material to undergo regular ion-exchange interactions similar to those observed in say, oxide films such as zinc oxide (ZnO), where sp-d band electrons of the oxide forming metal undergo exchange interactions with the localized d-electrons of other more electropositive metals during doping [277]. In such above mentioned exchange interactions, the conduction and valence bands of the respective constituents of the films as well as the dopant(s) experience certain negative and positive energy corrections resulting in a decrease in the materials' optical band gap energies [278]. Pertinent to the non-reactivity of carbon with silver, Stroud [132] stated that the implanted Ag ions may be captured in substitutional sites and become bonded chemically with the amorphous target or, if otherwise, the ions may proceed and come

to rest at some interstitial positions and consequently diffusing through the target lattice where they either get released or form bubbles at vacancy clusters.

In this context, the observed decrease in optical band gaps of the Ag:a-C nanomaterials can be attributed to absorption by the Ag NPs and the effect of their sizes at high fluences in the amorphous carbon as previously suggested by Ahmed et al. [272]. This phenomena is best explained based on the carbon sp^2 cluster model by Robertson [9] earlier highlighted in section 2.6.2 of this thesis. According to the model, the bonds in amorphous carbon contain mixtures of sp^2 and sp^3 bonds such that the sp^2 sites form graphitic clusters which are embedded in the sp^3 bonded matrix. Relating this model with the suggestion by Robertson & O'Reilly [182] that the π bonds of amorphous carbon (which are in close proximity with the Fermi energy level ($\boldsymbol{E_F}$) and linked to the sp^2 sites) are much weaker than the σ bonds (which are farther from the Fermi energy level and linked to the sp^3 sites), it would imply that the stopping Ag ions will sit in the vicinity of the of the sp^2 sites of the weaker π bonds than they would in the vicinity of the sp^3 sites of the stronger σ bonds. This is because, even as the local electrons in the π bonds are much less strongly bounded together, they would not react with the silver atoms but would rather intensely vibrate due to collective repulsive effect of the contributing valence electrons of the Ag ions resulting in sp^2 cluster shifting towards the Fermi energy level. In another view, increasing the dose of Ag NPs results into a more pronounced particle aggregation as observed from TEM micrographs of the nanomaterials. The sitting of metal particles occurs on both ends of the energy gap (i.e. the occupied π and unoccupied π^* states) linked to the sp^2 sites [95] so that the collective effect of the sitting Ag NPs on the cluster becomes enormous in terms of cluster shifting or size increase. In either way, the Fermi energy level is distorted (i.e. reduced in size) and consequently reducing the effective optical band gap of the material. Figure 4.18 shows the variation of optical band gap energy with ion fluence in the respective samples.

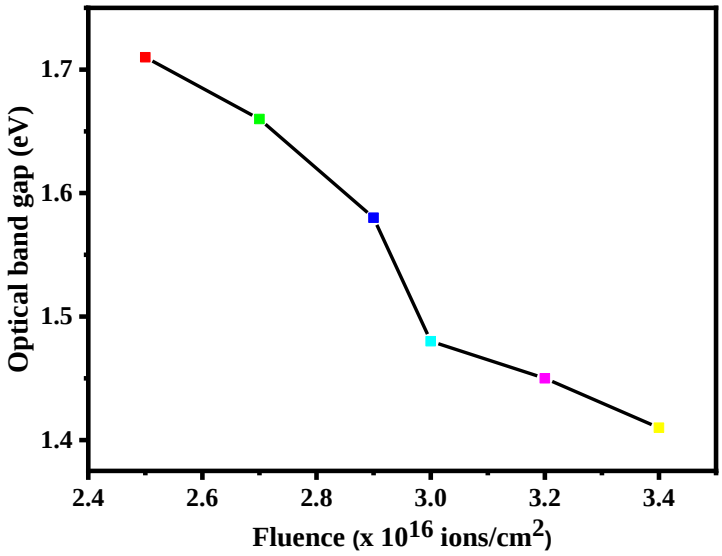


Figure 4.18: Variation of optical band gap energy with fluence.

4.3.2 Urbach energy

A plot of natural logarithm of absorption coefficient ($\ln \alpha$) versus photon energy ($h\upsilon$) in Equation 2.24 was used to determine the Urbach energy, E_u of the respective samples. This is done by determining the inverse of each slope along the linear portions of respective curves. Figures 4.19 and 4.20 show the Urbach plots for pristine a-C film and the various irradiated films in which the respective energies were observed to increase in proportion to increasing fluence of Ag ions.

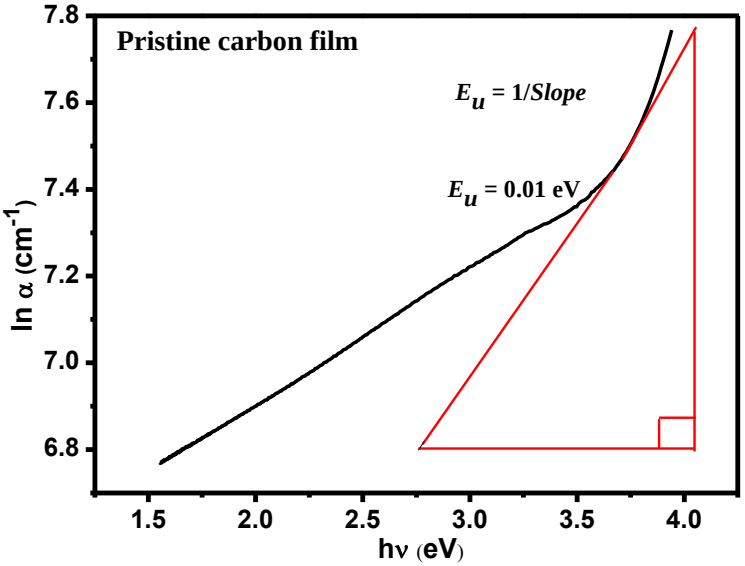


Figure 4.19: Graph of $\boldsymbol{ln\,\alpha}$ as a function of photon energy for pristine a-C film.

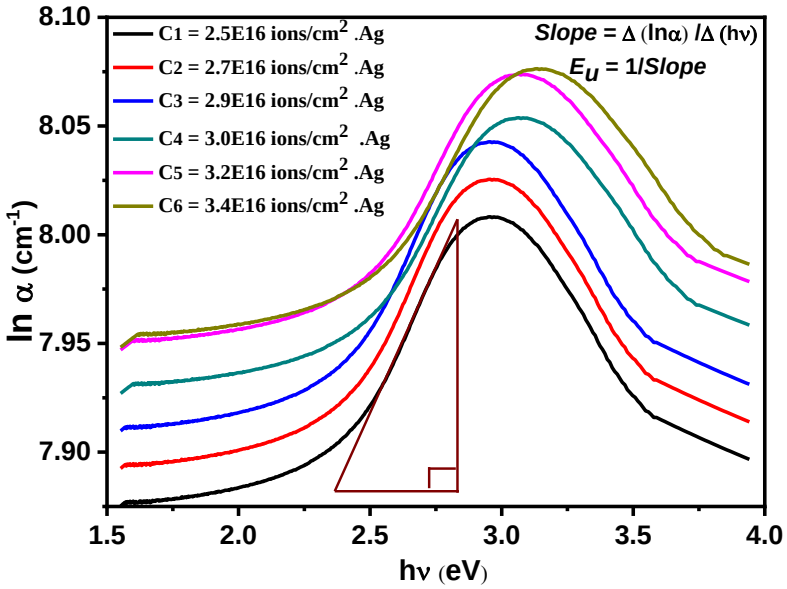


Figure 4.20: Combined graph of $\boldsymbol{ln\,\alpha}$ as a function of photon energy for the Ag:a-C nanocomposites.

The increased Urbach energy, which demonstrated great usefulness in probing disorder [280], is attributed to cluster size distribution which helps in evaluating the optical response (particularly absorption) due to defect states in the amorphous carbon structure [3]. Governed by this structural disorder, imperfection in stoichiometry and passivation at the material surface, the Urbach energy indicates disorder of phonon

states in the a-C films and is generally found below the absorption band edge of the nanomaterials. To this end, absorption edge generation at the extremes of the band gap energy could be attributed to either exciton-phonon or electron-phonon interaction influenced by the Ag ions [281]. The stronger the interaction, the higher the Urbach energy values and more bands' bending leading to favorable reductions in optical band gap. In order words, increasing fluence of Ag ions increases the Urbach energy and, by extension, reduces the optical band gap energy. Figure 4.21 shows the dependence of Urbach parameters on the fluence of irradiation.

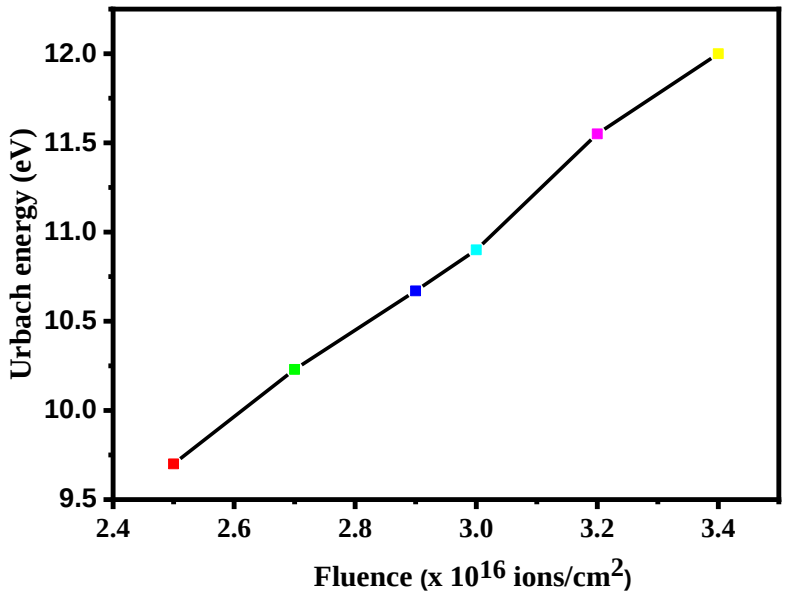


Figure 4.21: Dependence of Urbach parameter on fluence.

4.3.3 Refractive index

Respective optical band gap energy values for the different samples were used in the Lorentz-Lorentz equation (Equation 2.26) in order to determine the refractive index, $\boldsymbol{n}$ of the nanomaterials. Calculated refractive index values were observed to apparently increase with increasing fluence (decrease in band gap energies). This implies that the nanomaterials become appreciably denser with increasing fluence of Ag ions such that the velocity of light ($\boldsymbol{v}$) in the nanomaterials decreases which greatly affects light refraction in addition to increased light absorption. The dependence of the refractive index on fluence of irradiation is shown in Figure 4.22.

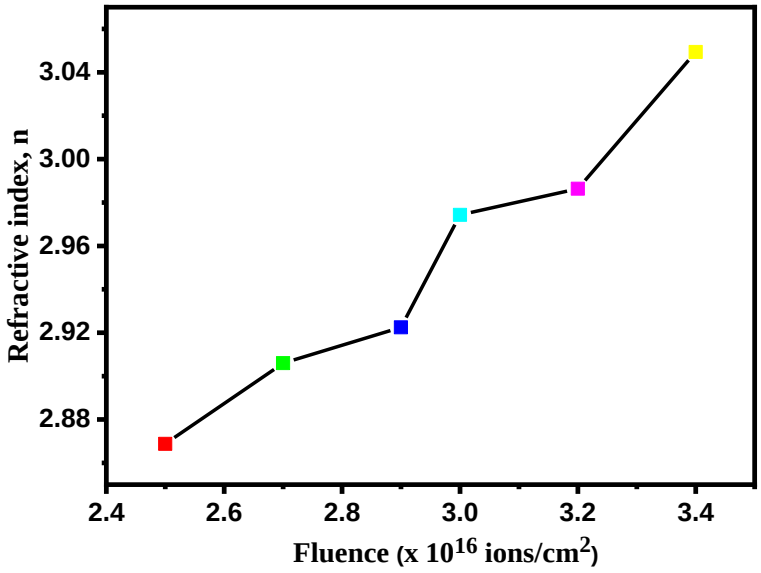


Figure 4.22: Variation of refractive index ($\boldsymbol{n}$) with fluence.

The rapid increase of refractive index of the nanomaterials in the visible region is attributed to the high polarizability and high atomic weight of the Ag ions [275, 276] such that their presence in the amorphous carbon matrix narrows the optical band gap resulting in a higher wavelength dispersion of the refractive index [276].

Furthermore, the refractive index values were used to determine other essential optical parameters of the materials [277] such as the dispersion of light energy, $\boldsymbol{E_d}$ below the interband absorption edge and the oscillator energy of the vibrating atoms due to photon excitation, $\boldsymbol{E_0}$ [277]. This is because, a good understanding of the dispersion of refractive indices in amorphous materials is necessary for a precise modelling and design of optoelectronic devices [285]. Using the Wemple-Di domenico (W-D) model (Equation 2.28), the dispersion energy and, by extension, the oscillator energy were both deduced from the slope ($\frac{\mathbf{1}}{\boldsymbol{E_d E_o}}$) and intercept ($\frac{\boldsymbol{E_d}}{\boldsymbol{E_o}}$) on the vertical axis of the straight line portion of $(\boldsymbol{n^2 - 1})^{-1}$ versus $\boldsymbol{E^2}$ plot as shown in Figure 4.23.

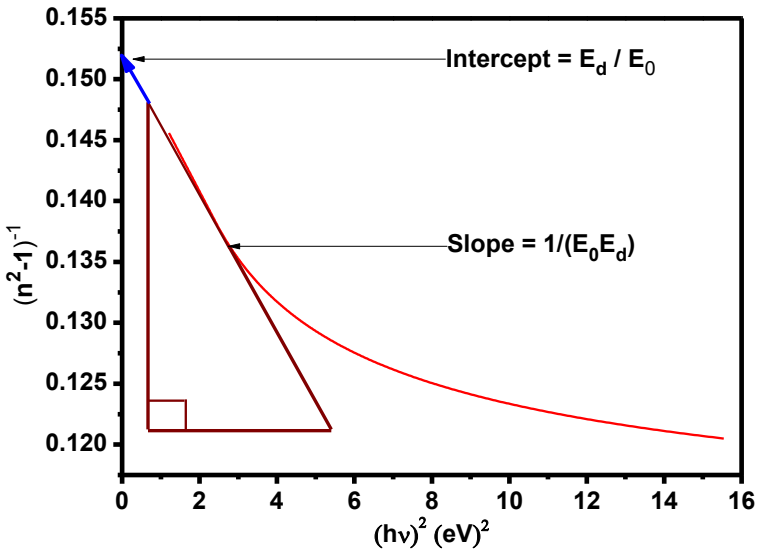


Figure 4.23: Plot of $(\boldsymbol{n^2-1})^{-1}$ versus $\boldsymbol{E^2}$ used in estimating the dispersion and oscillator energies.

The dispersion energy values were observed to appreciably increase with increasing fluence of Ag ions, an indication that there is fluence-enhanced evolution of more ordered phase of aggregated Ag ions within the sp^2 cluster which leads to a lower spectral separation of π-π* states in the amorphous carbon films [286]. This aggregated phase effect brings about a reasonable increase in dispersion for the different samples in relation to their corresponding refractive indices, extinction coefficients and, of course, the optical band gap energies. The oscillator energy, on the other hand, was observed to decrease with increasing fluence. This could be attributed to shifts in the absorption spectra within the short wavelength regions where, as demonstrated in the Tauc's plots, the absorption edges for the respective samples shifted to lower energies [281]. By letting $\boldsymbol{E=0}$ in Equation 2.28, respective values of static refractive index for the material at zero photon energy, $\boldsymbol{n_{(0)}}$ were also deduced. The extinction coefficient, $\boldsymbol{k}$ which gives information on the amount of the incident light that is absorbed by each sample at specified wavelength(s) was also calculated. The calculated values of $\boldsymbol{k}$ were also found to increase with fluence thus bearing a linear relationship with the optical band gaps of the respective nanomaterials. Table 4.4 gives a summary of the various optical parameters for the respective Ag:a-C films.

Table 4.4: Optical parameters of Ag irradiated amorphous carbon films.

Optical parameters	**C1**	**C2**	**C3**	**C4**	**C5**	**C6**
Optical band gap energy, $\boldsymbol{E_g}$ (eV) (±0.03)	1.71	1.66	1.58	1.48	1.45	1.41
Urbach energy, $\boldsymbol{E_u}$ (eV) (±0.26)	9.70	10.23	10.67	10.90	11.55	12.00
Refractive index, $\boldsymbol{n}$ (±0.03)	2.87	2.91	2.92	2.96	2.98	3.06
Static refractive index, $\boldsymbol{n_{(0)}}$	1.01	1.01	1.01	1.02	1.02	1.02
Extinction coefficient, $\boldsymbol{k}$	1.48	1.49	1.50	1.50	1.52	1.54
Dispersion energy, $\boldsymbol{E_d}$ (eV)	12.57	13.23	13.68	14.48	15.05	16.30
Oscillator energy, $\boldsymbol{E_0}$ (eV)	0.53	0.50	0.48	0.46	0.44	0.41

4.4 Application of Ag:a-C nanocomposites in photovoltaic devices

4.4.1 Ag:a-C nanocomposites as antireflectance coatings

Since the magnitude of photocurrent generated in any conventional photovoltaic system depends largely on the intensity of the light source, the expectation is that these nanocomposites would cause continuous attenuation thereby hindering the light-cell interactions due to their recorded fluence enhanced light retention (see Figure 4.14 in section 4.4). However, the observed trend is completely different. The photoconductivity measurements (see set up in Figure 3.21) show that, even with the gradual increase in absorption as a function of irradiation fluence, the nanocomposites coatings have become functional due to collective plasmonic activity of the metallic inclusions. This is evident from the trend of parametric values of the combined Ag:a-C/solar cell systems as recorded from the I-V (current-voltage) characterization. Figure 4.24 shows the combined I-V characteristic curves for the respective systems of pristine and Ag implanted amorphous carbon films. The measured parameters (I_{sc} and V_{oc}), though lower than the reference values, were found to increase appreciably and proportionately towards the references with increasing fluence of Ag ions.

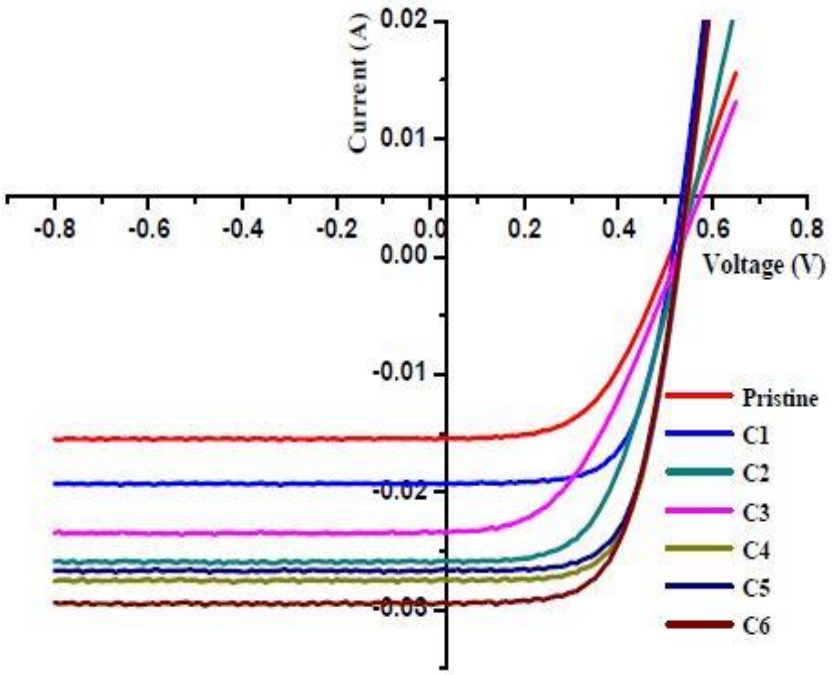


Figure 4.24: Combined I-V characteristic of Ag-a-C/solar cell systems with the nanocomposites as surface coatings.

Another interesting observation is that, in addition to plasmonic activities confirmed from optical characterization, there is an evidence of increasing light retention in the nanocomposite coatings. As such, the presence of Ag nanoparticles can be considered to have induced certain active light absorption and re-emission that causes parameter values of the combined Ag:a-C/solar cell systems to improve appreciably. This is evident from the relatively wide difference, in parameter values, between the pristine and irradiated films as seen in Figure 4.24. The incremental trend of short-circuit current for the respective nanocomposites could infer that at relatively high fluence of Ag implantation, the photocurrent will attain the reference value or even exceed it. This inference is due to the dependence of photocurrent on fluence of irradiation for the respective samples represented and shown in Figure 4.25. Using equations 2.35, 2.37, 2.38 and 2.39, corresponding values of power fill factor (***FF***), efficiency (η), series resistance ($\boldsymbol{R_S}$) and shunt ($\boldsymbol{R_{SH}}$) resistance were respectively evaluated, summarized and presented along with the measured device parameters in Table 4.5.

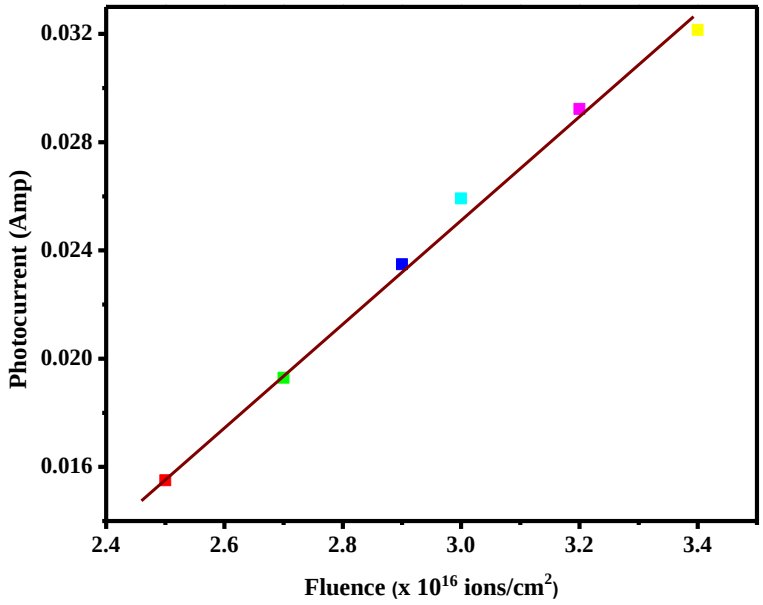


Figure 4.25: Fluence dependence of photocurrent on the combined (series arrangement) of Ag:a-C/solar cell systems.

Table 4.5: Summary of combined systems' parameters (series arrangement).

	Reference solar cell	**Pristine film**	**C1**	**C2**	**C3**	**C4**	**C5**	**C6**
Ag fluence, ϕ (x 10^{16} ions/cm^2)	0	0	2.50	2.70	2.90	3.00	3.20	3.40
Short circuit current, I_{SC} (Ampere)	0.050	0.016	0.019	0.023	0.027	0.027	0.028	0.030
Open circuit voltage, V_{OC} (Volt)	0.550	0.561	0.537	0.568	0.576	0.541	0.545	0.549
Fill Factor, FF (Watt)	0.826	0.828	0.822	0.830	0.831	0.823	0.824	0.825
Efficiency, η	15.106	4.809	5.681	7.381	8.494	7.961	8.289	8.967
Series resistance, R_S (Ωcm^2)	0.091	0.029	0.035	0.041	0.047	0.050	0.051	0.055
Shunt resistance, R_{SH} (Ωcm^2)	18.181	5.704	7.076	8.099	9.375	9.982	10.275	10.929

4.4.2 Ag:a-C nanocomposites as base layers for photovoltaic devices

Having established the above fluence-I_{sc} relation, the results obtained motivated the idea of incorporating the nanocomposites in actual photovoltaic device fabrication as active layers. In order to explore this, a spread of nanocomposites exhibiting the highest and lowest measured open circuit voltages were selected (i.e. C1, C2, C3 and C5).

Each device was characterized for photoconductivity employing the same procedure described in section 4.5.1. I-V characteristics show that the devices exhibit ohmic patterns under illumination with no evidence of rectification. Each system conducts linearly with very high resistances which were observed to depend on the fluence of Ag^{+} irradiation, i.e. decrease in resistance with respect to increase in Ag irradiation fluence. These observed behaviours could be as a result of mismatch at the interface between the metallic Ag:a-C films and the Si layers. The ohmic characteristic could as well be one of the distinguishing property of Schottky junction devices of non-rectification due to high doping in the semiconductor layer. To this effect, the nanocomposites behave as ordinary conducting paths due to non-rectifying effect at the junction (interface) thereby suppressing the n-type silicon layers upon which they were deposited. The implication is that each device has become a single passive system rather than active. Figure 4.26 shows the combined I-V relationship of the devices while Table 4.6 presents the summary of parameters.

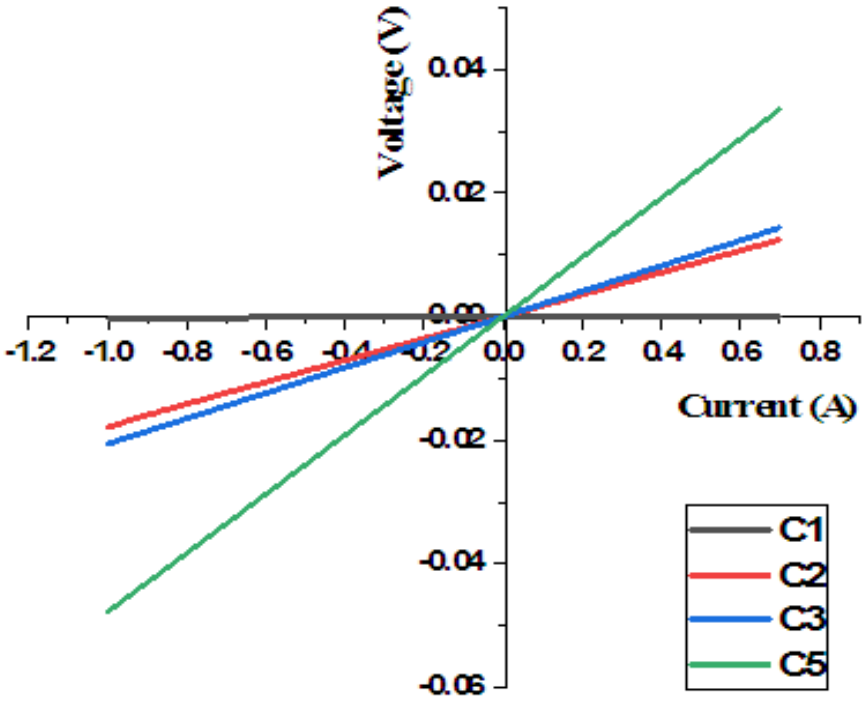


Figure 4.26: Combined I-V relationship for the fabricated devices with the nanocomposites C1, C2, C3 and C5 as base active layers.

Table 4.6: Summary of parameters for the Ag:a-C based devices.

Sample	**Fluence, ϕ (ions/cm^2)**	**n-type layer thickness (nm)**	**Ag:a-C layer thickness (nm)**	**Resistivity, ρ (Ω.cm)**
C1	2.5 x 10^{16}	20	< 500	7.176 x 10^{-11}
C2	2.7 x 10^{16}	20	< 500	7.696 x 10^{-9}
C3	2.9 x 10^{16}	20	< 500	7.800 x 10^{-9}
C5	3.2 x 10^{16}	20	< 500	1.661 x 10^{-8}

CHAPTER FIVE

5.0 Summary and Conclusions

5.1 Summary

The main purpose of these research was to come up with a carbon-based material that can provide good antireflectance property for improved light retention, improved charge carrier concentration due to enhanced light absorbance, and effective quasi-intermediate band property. Preliminary optical absorption measurements were conducted on amorphous carbon films, as free-standing films, in order to evaluate their pristine light absorption. Accelerator-based silver (Ag) ion implantation was carried out on the films forming Ag:a-C nanocomposites at varying fluences to establish responses, due to ion fluence, on the light retention property of the nanocomposites. This optical response investigation was achieved using the UV-visible spectrophotometry. Microstructural properties of the materials were investigated using Raman spectroscopy, scanning electron microscopy (SEM), transmission electron microscopy (TEM), atomic force microscopy (AFM) and energy dispersive x-ray spectroscopy as complimentary analysis.

For the sample preparation, amorphous carbon films originally supplied on 7 cm x 2.5 cm glass slides were carefully cut into seven smaller pieces of 1 cm x 2.5 cm respectively. One was kept as reference and the remaining were implanted with Ag ions at varying fluences in the range 2.5 to 3.4 x 10^{16} ions/cm^2. Sections of the pristine and implanted films were floated, mounted on cleaned/polished copper sheets and analysed for optical response as free standing films. Some portions of the nanocomposites were characterized for microstructural properties on glass substrates and some on indium titanium oxide (ITO) substrates for potential applications in photovoltaic systems.

The results obtained show that the nanocomposites exhibit Raman fingerprints typical of carbon with G- and D-peaks shifting, broadening as well as intensity variations that were dependent upon the fluence of irradiation. A relative increase in structural disorder, sp^2 cluster aggregation and cluster size attenuation were recorded due to increasing fluence of irradiation. SEM analysis showed agglomerated Ag particles in sphere-like shapes with average particle diameters in the range ~ 5 nm to ~ 20 nm respectively while TEM micrographs revealed many

silver-rich micro grains in the non-reactive phase of the Ag:a-C nanocomposites and emerging silver oxide (AgO) phase at higher fluence due to tarnishing. AFM analysis shows grain size increase from ~ 5 nm to ~ 21 nm with surface roughness ~ 1.76 nm for pristine film to ~ 4.92 nm for nanocomposites with the highest irradiation fluence. EDS spectroscopy confirmed a dominant carbon phase and high oxygen presence largely due to oxides of silicon and silver from supporting substrate and surface tarnishing. Optical characterization, via UV-visible spectrophotometry, revealed a clear surface plasmon resonance peak (SPR) of Ag nanoparticles at a wavelength ~ 428 nm with blue shifting in the wavelength range ~ 418 nm to ~ 396 nm for the Ag irradiated films. Optical band gap energy, $\boldsymbol{E_g}$ decreases from 1.71 eV to 1.41 eV while Urbach energy, $\boldsymbol{E_u}$ increases from 9.70 eV to 12.00 eV with increasing fluence. Urbach parameters confirmed the observed relative disorder form Raman studies. Other essential optical parameters such as refractive index ($\boldsymbol{n}$), static refractive index ($\boldsymbol{n_0}$), extinction coefficient ($\boldsymbol{k}$), dispersion energy ($\boldsymbol{E_d}$) and oscillator energy ($\boldsymbol{E_o}$) were all found to vary with fluence and in favour of the material potentials.

In terms of application, a direct (series) incorporation of respective nanocomposites with a reference silicon solar cell revealed interesting coating potentials by improving short-circuit current, $\boldsymbol{I_{SC}}$ from 1.90 mA to 3.00 mA and open-circuit voltage, $\boldsymbol{V_{OC}}$ to as high as 0.576 V respectively. For the series system, efficiencies were well below the reference value (15.11) from as low as 5.68 for the lowest fluence to 8.97 for the highest fluence Ag:a-C nanocomposites. This indicated good potentials for the nanocomposites as surface coatings photovoltaic and other optoelectronic applications. To further explore their potentials, sections of the Ag:a-C nanocomposites were used as base layers in fabricating silicon-based photovoltaic devices. This was achieved via r.f. magnetron sputtering of amorphous silicon thin films on the Ag:a-C nanocomposites and their subsequent implantation with phosphorous (P^+) to form a metal/n-type Schottky barrier diodes. The I-V characteristics of these devices were found to be ohmic possibly due to mismatch at the interface of the two materials and the eventual suppressing of silicon layers by the Ag:a-C nanocomposites thereby rendering them passive rather than active.

5.2 Conclusion

The ability of carbon to exist in different stand-alone allotropes makes it an interesting research material. The use of metal inclusions, particularly noble metals, for property modification of carbon-based materials shows great prospects for research and industrial applications. Accelerator based ion implantation, having an edge over conventional chemical deposition methods, served as an excellent tool in producing carbon nanocomposites with improved properties. This research work provided a detailed optical characterization of Ag implanted amorphous carbon films. The incorporation of Ag into amorphous carbon matrix induced substitutional defects which distorted the materials electronic structure thereby leading to changes in the overall optical transparency and optical band gap. The optical band gap decreased with increasing fluence of Ag irradiation. Urbach parameter increased at higher irradiation fluence to establish an interesting structural ordering of the nanocomposites. This observed tunable band gap, coupled with the plasmonic activities of Ag atoms in the carbon matrix, posed the nanocomposites in great advantages of being used as surface coatings and as functional materials for solar cell efficiency enhancement.

5.3 Recommendation

Although there is relative success in exploring the surface applications of these Ag:a-C nanocomposites, further investigation into their photovoltaic potentials is required. Thinner but floatable carbon films (< 500 nm) initially deposited on ITO substrates may be used with high fluence of Ag irradiation at low implantation energy. These would ensure a uniformly distributed film on ITO and reduce the possible effect of surface sputtering during implantation. On the application of nanocomposites in device fabrication, a sandwich arrangement with Ag:a-C incorporated between two silicon layers may be explored. And in order to minimize or eradicate totally the problem of band gap mismatch, a mild annealing of the nanocomposites prior to or after sputtering of the silicon layers may be employed.

REFERENCES

[1] R. P. Feynman, "There is Plenty of Room at the Bottom," *J. Microeleciromechanical Syst.*, vol. 1, no. 1, pp. 60–66, 1992.

[2] K. E. Drexler, "Molecular Machinery and Manufacturing with Applications to Computation," Massachusetts Institute of Technology, 1991.

[3] L. Dai, D. W. Chang, J.-B. Baek, and W. Lu, "Carbon nanomaterials for advanced energy conversion and storage.," *Small*, vol. 8, no. 8, pp. 1130–66, 2012.

[4] S. L. Candelaria *et al.*, "Nanostructured carbon for energy storage and conversion," *Nano Energy*, vol. 1, no. 2, pp. 195–220, 2012.

[5] A. Luque and A. Martí, "The intermediate band solar cell: Progress toward the realization of an attractive concept," *Adv. Mater.*, vol. 22, no. 2, pp. 160–174, 2010.

[6] M. S. Dresselhaus and R. Kalish, *Ion Implantation in Diamond and Related Materials*. Springer-Verlag, Barlin, 1992.

[7] Z. Zhai, H. Shen, J. Chen, J. Li, and S. Zhang, "Growth of ideal amorphous carbon films at low temperature by e-beam evaporation," *RSC Adv.*, vol. 6, pp. 42353–42360, 2016.

[8] S. G. Romanov and C. M. S. Torres, *Handbook of Nanostructured Materials and Technology*. 1999.

[9] J. Robertson, "Electronic Structure and Bonding of a-C:H," *Mater. Sci. Forum*, vol. 52, no. 53, pp. 125–150, 1990.

[10] R. A. Sinton and A. Cuevas, "Contactless determination of current-voltage characteristics and minority-carrier lifetimes in semiconductors from quasi-steady-state photoconductance data," *Appl. Phys. Lett.*, vol. 69, no. 17, pp. 2510–2512, 1996.

[11] T. Owen, *Fundamentals of modern UV-visible spectroscopy*. Germany: Agilent Technologies, 2000.

[12] https://www.chemguide.co.uk/analysis/uvvisible/spectrometer.html.

[13] W. M. Mpingi, "Structural, Electrical and Electronic Properties of Diamond like Carbon (DLC) and Carbon-Based Materials," 2013.

[14] B. Fultz and J. M. Howe, *Transmission electron microscopy and diffractometry of materials*, 3rd ed., vol. 1. Springer-Verlag, Barlin, 2008.

[15] A. A. Onoprienko and M. I. Danylenko, "Annealing effects in Ag-doped amorphous carbon films deposited by dc magnetron sputtering," *Surf. Coatings Technol.*, vol. 206, no. 16, pp. 3450–3453, 2012.

[16] "http://www.semicore.com/images/photos/diagram-sputtering-process.png." .

[17] P. Ehrenfreund and B. H. Foing, "Fullerenes and cosmic carbon," *Science (80-.).*, vol. 329, no. 5996, pp. 1159–1160, 2010.

[18] J. Robertson, "Diamond-like amorphous carbon," *Mater. Sci. Eng. R Reports*, vol. 37, no. 4–6, pp. 129–281, 2002.

[19] J. Robertson, “Comparison of diamond-like carbon to diamond for applications,” *Phys. Status Solidi Appl. Mater. Sci.*, vol. 205, no. 9, pp. 2233–2244, 2008.

[20] A. Miller, “Ion Implantation Systems,” in *South African Institute of Physics, SAIP2014.*, 2014, pp. 1–10.

[21] S. University, “Global Climate & Energy Project: An Assessment of Solar Energy Conversion Technologies and Research Opportunities,” 2006.

[22] D. J. Cott *et al.*, “Synthesis of large area carbon nanosheets for energy storage applications,” *Carbon N. Y.*, vol. 58, pp. 59–65, 2013.

[23] A. Ismaila, S.R. Naidoo, and F. Cummings, “Effects of irradiation energy and fluence on the optical absorbance of silver implanted amorphous carbon thin films,” in *South African Institute of Physics, SAIP.*, 2017, p. 1.

[24] R. Singhal, J. C. Pivin, R. Chandra, and D. K. Avasthi, “Ion irradiation studies of silver/amorphous carbon nanocomposite thin film,” *Surf. Coatings Technol.*, vol. 229, pp. 50–54, 2013.

[25] M. Rusop, T. Kinugawa, T. Soga, and T. Jimbo, “Preparation and microstructure properties of tetrahedral amorphous carbon films by pulsed laser deposition using camphoric carbon target,” *Diam. Relat. Mater.*, vol. 13, no. 11–12, pp. 2174–2179, 2004.

[26] H. Zhu, J. Wei, K. Wang, and D. Wu, “Applications of carbon materials in photovoltaic solar cells,” *Sol. Energy Mater. Sol. Cells*, vol. 93, no. 9, pp. 1461–1470, 2009.

[27] K. Dayana, A. N. Fadzilah, and M. Rusop, “Optical properties of amorphous carbon thin films deposited by thermal CVD using camphor oil,” *Proc. - 2011 IEEE Student Conf. Res. Dev. SCOReD 2011*, no. Di, pp. 25–29, 2011.

[28] H. Dimigen, H. Hübsch, and R. Memming, “Tribological and electrical properties of metal-containing hydrogenated carbon films,” *Appl. Phys. Lett.*, vol. 50, no. 16, pp. 1056–1058, 1987.

[29] H. Grischke, M.; Bewilogua, K.; Dimigen, “Preparation, properties and structure of metal containing amorphous hydrogenated carbon films,” *Mater. Manufacuring Process*, vol. 8, no. 4–5, pp. 407–417, 2007.

[30] O. Turan, “Energy Dispersive X-Ray, EDX and Wavelength Dispersive X-ray spectroscopy (WDX),” *Chem. Eng.*, 2010.

[31] S. Aisenberg and R. Chabot, “Ion-beam depsition of thin films of Diamond-like carbon,” *J. Appl. Phys.*, vol. 42, no. 7, pp. 2953–2958, 1971.

[32] Y. Lifshitz, “Hydrogen-free amorphous carbon films: correlation between growth conditions and properties,” *Diam. Relat. Mater.*, vol. 5, no. 3–5, pp. 388–400, 1996.

[33] Y. Lifshitz, “Diamond-like carbon — present status,” *Diam. Relat. Mater.*, vol. 8, no. 8–9, pp. 1659–1676, 1999.

[34] J. J. Cuomo, J. P. Doyle, J. Bruley, and J. C. Liu, “Sputter deposition of dense diamond-like carbon films at low temperature,” *Appl. Phys. Lett.*, vol. 58, no. 5, pp. 466–468, 1991.

[35] J. Schwan *et al.*, "Tetrahedral amorphous carbon films prepared by magnetron sputtering and dc ion plating," *J. Appl. Phys.*, vol. 79, no. 3, pp. 1416–1422, 1996.

[36] I. G. Brown, "Cathodic Arc Deposition," no. 5, 1998.

[37] J. Vetter, "60years of DLC coatings: Historical highlights and technical review of cathodic arc processes to synthesize various DLC types, and their evolution for industrial applications," *Surf. Coatings Technol.*, vol. 257, pp. 213–240, 2014.

[38] A. A. Voevodin and M. S. Donley, "Preparation of amorphous diamond-like carbon by pulsed laser deposition: A critical review," *Surf. Coatings Technol.*, vol. 82, no. 3, pp. 199–213, 1996.

[39] P. E. Mota-Santiago, A. Crespo-Sosa, J. L. Jiménez-Hernández, H. G. Silva-Pereyra, J. A. Reyes-Esqueda, and A. Oliver, "Size characterisation of noble-metal nano-crystals formed in sapphire by ion irradiation and subsequent thermal annealing," *Appl. Surf. Sci.*, vol. 259, pp. 574–581, 2012.

[40] A. V. Rode, B. Luther-Davies, and E. G. Gamaly, "Ultrafast ablation with high-pulse-rate lasers. Part II: Experiments on laser deposition of amorphous carbon films," *J. Appl. Phys.*, vol. 85, no. 8, pp. 4222–4230, 1999.

[41] A. Mart and A. Luque, "Intermediate Band Solar Cells," *Sol. Energy Mater. Sol. Cells*, pp. 18–19, 2009.

[42] L. Holland and S. M. Ojha, "Deposition of hard and insulating carbonaceous films on an r.f. target in a butane plasma," *Thin Solid Films*, vol. 38, no. 2, pp. 17–19, 1976.

[43] L. Martinu *et al.*, "Properties and stability of diamond-like carbon films related to bonded and unbonded hydrogen," *Diam. Relat. Mater.*, vol. 2, no. 5–7, pp. 673–677, 1993.

[44] M. N. R. Ashfold, P. W. May, C. A. Rego, and N. M. Everitt, "Thin film diamond by chemical vapour deposition methods," *Chem. Soc. Rev.*, vol. 23, no. 1, p. 21, 1994.

[45] S. S. Shin, B. H. Choi, Y. M. Kim, J. H. Lee, and D. C. Shin, "The effects of atmospheric pressure plasma on the synthesis of carbon nanotubes," *Microelectron. Eng.*, vol. 86, no. 4–6, pp. 925–928, 2009.

[46] Y. X. Liu, J. H. Liu, C. C. Zhu, and W. H. Liu, "Effects of gas pressure and plasma power on the growth of carbon nanostructures," *Appl. Surf. Sci.*, vol. 256, no. 7, pp. 1996–1999, 2010.

[47] T. Yamane and T. Asakura, "The Structural Characteristics of Carbon," Lecture Module, 2002.

[48] S. M. M. Dufrène *et al.*, "Hydrogenated amorphous carbon thin films deposition by pulsed DC plasma enhanced by electrostatic confinement," *Surf. Coatings Technol.*, vol. 258, pp. 219–224, 2014.

[49] P. Kumar and A. Kumar, "Carrier type modulation in current annealed graphene layers," *Appl. Phys. Lett.*, vol. 104, no. 8, 2014.

[50] T. . K. T.A. Rao, "A Survey of Ion Implantation Techniques for Enhanced

Property Modification for Tailored Materials," *Int J Adv Manuf Technol*, no. 14, pp. 153–159, 1997.

[51] A. Bubenzer, B. Dischler, G. Brandt, and P. Koidl, "Rf-plasma deposited amorphous hydrogenated hard carbon thin films: Preparation, properties, and applications," *J. Appl. Phys.*, vol. 54, no. 8, pp. 4590–4595, 1983.

[52] P. D. Townsend, "Optical effects of ion implantation," *Rep. Prog. Phys.*, vol. 50, no. 5, pp. 501–558, 1987.

[53] M. P. Uma, "Doping by Diffusion and Implantation," *J. Mater. Sci.*, vol. 36, no. 2, pp. 1–49, 2001.

[54] M. Siegal, D. Tallant, L. Martinez-Miranda, J. Barbour, R. Simpson, and D. Overmyer, "Nanostructural characterization of amorphous diamondlike carbon films," *Phys. Rev. B*, vol. 61, no. 15, pp. 10451–10462, 2000.

[55] L. Mahmudin, E. Suharyadi, A. Bambang, S. Utomo, and K. Abraha, "Optical Properties of Silver Nanoparticles for Surface Plasmon Resonance (SPR) - Based Biosensor Applications," no. July, pp. 1071–1076, 2015.

[56] G. X. Chen, M. H. Hong, T. C. Chong, H. I. Elim, G. H. Ma, and W. Ji, "Preparation of carbon nanoparticles with strong optical limiting properties by laser ablation in water," *J. Appl. Phys.*, vol. 95, no. 3, pp. 1455–1459, 2004.

[57] C. R. Lin, D. H. Wei, C. K. Chang, and W. H. Liao, "Optical properties of Diamond-like Carbon films for antireflection coating by RF magnetron sputtering method," *Phys. Procedia*, vol. 18, pp. 46–50, 2011.

[58] A. Luque, A. Martí, and C. Stanley, "Understanding intermediate-band solar cells," *Nat. Photonics*, vol. 6, no. 3, pp. 146–152, 2012.

[59] A. Luque and A. Martí, "Increasing the Efficiency of Ideal Solar Cells by Photon Induced Transitions at Intermediate Levels," *Phys. Rev. Lett.*, vol. 78, no. 26, pp. 5014–5017, 1997.

[60] W. Walukiewicz, "Semiconductor Materials for Intermediate Band Solar Cells," *PPTs*, 2004.

[61] Y. Okada *et al.*, "Intermediate band solar cells: Recent progress and future directions," *Appl. Phys. Rev.*, vol. 2, no. 2, 2015.

[62] N. M. S. Marins *et al.*, "Properties of hydrogenated amorphous carbon films deposited by PECVD and modified by SF6 plasma," *Surf. Coatings Technol.*, vol. 206, no. 4, pp. 640–645, 2011.

[63] https://www.boundless.com/chemistry/nonmetallic-elements/carbon/properties-carbon/.

[64] M. Imam and M. Yimamu, *Chemical vapour deposition of boron-carbon thin films from organoboron precursors Mewlude Imam (Maiwulidan Yimamu)*, no. 1741. 2016.

[65] J. Robertson, "Mechanical properties and coordinations of amorphous carbons," *Phys. Rev. Lett.*, vol. 68, no. 2, pp. 220–223, 1992.

[66] J. Robertson, "Electronic structure of diamond-like carbon," *Diam. Relat. Mater.*, vol. 6, pp. 212–218, 1997.

[67] J. Robertson, "Amorphous carbon," *Adv. Phys.*, vol. 60, no. 1, pp. 87–144, 2011.

[68] M. Rubio-roy, C. Corbella, J. Andújar, and E. Bertran, "Tribological Properties of Fluorinated Amorphous Carbon Thin Films," in *New Tribological Ways*, 2011, pp. 47–70.

[69] C. Casiraghi, J. Robertson, and A. C. Ferrari, "Diamond-like carbon for data and beer storage," *Mater. Today*, vol. 10, no. 1–2, pp. 44–53, 2007.

[70] P. L. Walker Jr, J. F. Rakszawski, and a. F. Amington, "Distinguishing Between Graphitic and Amorphous Carbon," *Chemistry*, vol. 46, no. 7. pp. 1620–1624, 1954.

[71] C. Che, Y. Li, G. Zhang, and D. Deng, "Doped Amorphous Carbon Films Prepared by Liquid Phase Electrodeposition," *Open J. Synth. Theory Appl.*, vol. 2014, no. 3, pp. 5–13, 2014.

[72] A. C. Ferrari, J. Robertson, M. G. Beghi, C. E. Bottani, R. Ferulano, and R. Pastorelli, "Elastic constants of tetrahedral amorphous carbon films by surface Brillouin scattering," *Appl. Phys. Lett.*, vol. 75, no. 13, pp. 1893–1895, 1999.

[73] C. Casiraghi, A. C. Ferrari, and J. Robertson, "Raman spectroscopy of hydrogenated amorphous carbons," *Phys. Rev. B - Condens. Matter Mater. Phys.*, vol. 72, no. 8, pp. 1–14, 2005.

[74] M. A. Tamor, W. C. Vassell, and K. R. Carduner, "Atomic constraint in hydrogenated diamond-like carbon," *Appl. Phys. Lett.*, vol. 58, no. 6, pp. 592–594, 1991.

[75] S. F. Yoon, K. H. Tan, Rusli, and J. Ahn, "Modeling and analysis of the electron cyclotron resonance diamond-like carbon deposition process," *J. Appl. Phys.*, vol. 91, no. 3, pp. 1634–1639, 2002.

[76] T. Schwarz-Selinger, A. Von Keudell, and W. Jacob, "Plasma chemical vapor deposition of hydrocarbon films: The influence of hydrocarbon source gas on the film properties," *J. Appl. Phys.*, vol. 86, no. 7, pp. 3988–3996, 1999.

[77] B. Popescu, A. Tagliaferro, F. De Zan, and E. A. Davis, "Hydrogen incorporation and its structural effect on a-C : H films deposited by magnetron sputtering," vol. 269, pp. 803–807, 2000.

[78] O. Durand-Drouhin, M. Lejeune, and M. Benlahsen, "Growth and bonding structure of hard hydrogenated amorphous carbon thin films deposited from an electron cyclotron resonance plasma," *J. Appl. Phys.*, vol. 91, no. 2, pp. 867–873, 2002.

[79] A. C. Ferrari *et al.*, "Density, sp3 fraction, and cross-sectional structure of amorphous carbon films determined by x-ray reflectivity and electron energy-loss spectroscopy," *Phys. Rev. B*, vol. 62, no. 16, pp. 11089–11103, 2000.

[80] N. A. Morrison, S. E. Rodil, A. C. Ferrari, J. Robertson, and W. I. Milne, "High rate deposition of ta-C:H using an electron cyclotron wave resonance plasma source," *Thin Solid Films*, vol. 337, no. 1–2, pp. 71–73, 1999.

[81] M. Weiler, S. Sattel, K. Jung, H. Ehrhardt, V. S. Veerasamy, and J. Robertson, "Highly tetrahedral, diamond-like amorphous hydrogenated carbon prepared from a plasma beam source," *Appl. Phys. Lett.*, vol. 64, no. 21, pp. 2797–2799,

1994.

[82] M. Weiler *et al.*, “Preparation and properties of highly tetrahedral hydrogenated amorphous carbon,” *Phys. Rev. B*, vol. 53, no. 3, pp. 1594–1608, 1996.

[83] M. Weiler, K. Lang, E. Li, and J. Robertson, “Deposition of tetrahedral hydrogenated amorphous carbon using a novel electron cyclotron wave resonance reactor,” *Appl. Phys. Lett.*, vol. 72, no. 11, pp. 1314–1316, 1998.

[84] A. Zeng, V. F. Neto, J. J. Gracio, and Q. H. Fan, “Diamond-like carbon (DLC) films as electrochemical electrodes,” *Diam. Relat. Mater.*, vol. 43, pp. 12–22, 2014.

[85] E. G. Spencer, P. H. Schmidt, D. C. Joy, and F. J. Sansalone, “Ion-beam-deposited polycrystalline diamondlike films,” *Appl. Phys. Lett.*, vol. 29, no. 2, pp. 118–120, 1976.

[86] J. Robertson, “Hard amorphous (diamond-like) carbons,” *Prog. Solid State Chem.*, vol. 21, no. 4, pp. 199–333, 1991.

[87] N. Basman, N. Aslan, O. Uzun, G. Cankaya, and U. Kolemen, “Electrical characterization of metal/diamond-like carbon/inorganic semiconductor MIS Schottky barrier diodes,” *Microelectron. Eng.*, vol. 140, pp. 18–22, 2015.

[88] C. Donnet and A. Erdemir, *Diamond-like carbon films: A historical overview*. 2008.

[89] W. Jacob and W. Möller, “On the structure of thin hydrocarbon films,” *J. Appl. Phys.*, vol. 63, no. 13, pp. 1771–1773, 1993.

[90] N. Cho *et al.*, “Chemical structure and physical properties of diamond-like amorphous carbon films prepared by magnetron sputtering,” *J. Mater. Res.*, vol. 5, no. 11, pp. 2543–2554, 1990.

[91] T. E. Derry, E. K. Nshingabigwi, M. Levitt, J. Neethling, and S. R. Naidoo, “Cross-section transmission electron microscopy of the ion implantation damage in annealed diamond,” *Nucl. Instruments Methods Phys. Res. Sect. B Beam Interact. with Mater. Atoms*, vol. 267, no. 16, pp. 2705–2707, 2009.

[92] A. M. ;Rusetski. M. S. ;Stelmak. V. F. ;d. W. K. ;Frie. T. ;Wandel. K. ;Didy. A. J. ;Lapte. V. A. Varichenko V. S.;Zaitsev, “Scanning tunneling microscopy of diamond irradiated with high energy ions,” *Diam. Relat. Mater.*, vol. 3, p. 711, 1994.

[93] R. E. Franklin, “Crystallite growth in graphitizing and non-graphitizing carbons,” *http://rspa.royalsocietypublishing.org/*, pp. 196–220, 1951.

[94] L. B. Ebert, “Science of fullerenes and carbon nanotubes,” *Carbon N. Y.*, vol. 35, no. 3, pp. 437–438, 1997.

[95] J. Robertson, “Gap states in diamond-like amorphous carbon,” *Philos. Mag. B Phys. Condens. Matter; Stat. Mech. Electron. Opt. Magn. Prop.*, vol. 76, no. 3, pp. 335–350, 1997.

[96] G. M. Pharr *et al.*, “Hardness, elastic modulus, and structure of very hard carbon films produced by cathodic-arc deposition with substrate pulse biasing,” *Appl. Phys. Lett.*, vol. 779, p. 779, 1995.

[97] P. Koidl, C. Wild, B. Dischler, J. Wagner, and M. Ramsteiner, "Plasma Deposition, Properties and Structure of Amorphous Hydrogenated Carbon Films," *Materials Science Forum*, vol. 52–53. pp. 41–70, 1990.

[98] B. Schultrich, H.-J. Scheibe, G. Grandremy, and D. Schneider, "Elastic Modulus of Amorphous Carbon Films," *Phys. Status Solidi*, vol. 145, no. 2, pp. 385–392, 1994.

[99] M. Constantinou, P. Nikolaou, L. Koutsokeras, and A. Avgeropoulos, "Metal (Ag / Ti) -Containing Hydrogenated Amorphous Carbon Nanocomposite Films with Enhanced Nanoscratch Resistance : Hybrid PECVD / PVD System and Microstructural Characteristics," *Nanomaterials*, vol. 8, no. 209, pp. 1–20, 2018.

[100] Y. Zengliang, "Production and acceleration of ions," *Introd. to Ion Beam Biotechnol.*, vol. Book Chapt, pp. 11–30, 2006.

[101] B. a. Weaver and a. J. Westphal, "Energy loss of relativistic heavy ions in matter," *Nucl. Instruments Methods Phys. Res. Sect. B Beam Interact. with Mater. Atoms*, vol. 187, pp. 285–301, 2002.

[102] A. L. Stepanov, "Synthesis of silver nanoparticles in dielectric matrix by ion implantation: A review," *Rev. Adv. Mater. Sci.*, vol. 26, no. 1–2, pp. 1–29, 2010.

[103] G. Dearnaley, "Practical Applications of Ion Implantation," *J. Met.*, no. September, pp. 18–28, 1982.

[104] C. A. Straede, "Practical Applications of Ion Implantation," vol. 30, pp. 113–122, 1989.

[105] M. Iwaki, "Progress in ion implantation technology for metal surface treatments and other related topics," *1998 Int. Conf. Ion Implant. Technol. Proc. (Cat. No.98EX144)*, vol. 2, pp. 824–826, 1998.

[106] V. Muthukumaran, M. S. Kumar, and V. Selladurai, "Improvement of surface properties of AISI 316L SS by oxygen and helium ion implantation," *J. Eng. Des. Technol.*, vol. 11, no. 1, 2013.

[107] M. M. M. Bilek, "Biofunctionalization of surfaces by energetic ion implantation: Review of progress on applications in implantable biomedical devices and antibody microarrays," *Appl. Surf. Sci.*, vol. 310, pp. 3–10, 2014.

[108] F. Salvat, A. Jablonski, and C. J. Powell, "Elsepa - Dirac partial-wave calculation of elastic scattering of electrons and positrons by atoms, positive ions and molecules," *Comput. Phys. Commun.*, vol. 165, no. 2, pp. 157–190, 2005.

[109] A. Jablonski, F. Salvat, and C. J. Powell, "Comparison of electron elastic-scattering cross sections calculated from two commonly used atomic potentials," *J. Phys. Chem. Ref. Data*, vol. 33, no. 2, pp. 409–451, 2004.

[110] D. Bote, F. Salvat, A. Jablonski, and C. J. Powell, "The effect of inelastic absorption on the elastic scattering of electrons and positrons in amorphous solids," *J. Electron Spectros. Relat. Phenomena*, vol. 175, no. 1–3, pp. 41–54, 2009.

[111] K. G. Stephens and I. H. Wilson, "Properties and applications of ion-implanted films," *Thin Solid Films*, vol. 50, no. C, pp. 325–347, 1978.

[112] M. Massoud, B. Canut, P. Newby, L. Frechette, P. O. Chapuis, and J. M. Bluet,

"Swift heavy ion irradiation reduces porous silicon thermal conductivity," *Nucl. Instruments Methods Phys. Res. Sect. B Beam Interact. with Mater. Atoms*, vol. 341, pp. 27–31, 2014.

[113] S. Mishra *et al.*, "Strain buildup in GaAs due to 100 MeV Ag ion irradiation," *Nucl. Instruments Methods Phys. Res. Sect. B Beam Interact. with Mater. Atoms*, vol. 316, pp. 192–197, 2013.

[114] I. B. Khaibullin, "Optical and electrical properties of C+-implanted amorphous diamond-like carbon films," vol. 128, pp. 719–722, 1997.

[115] M. Tanjyo and M. Naito, "History of ion implanter and its future perspective," *SEI Tech. Rev.*, no. 73, pp. 22–30, 2011.

[116] A. Schöner, "Ion Implantation and Diffusion in SiC," 2000, pp. 51–84.

[117] S. Felch, M. Current, and M. Taylor, "Ion Implantation for Semiconductor Devices: The Largest Use of Industrial Accelerators," *Accelconf.Web.Cern.Ch*, pp. 740–744, 2013.

[118] M. O. E.- Ghossain, "Calculations of Stopping Power, and Range of Ions Radiation (Alpha Particles) Interaction with Different Materials and Human Body Parts," *Int. J. Physics, Vol. 5, 2017, Pages 92-98*, vol. 5, no. 3, pp. 92–98, 2017.

[119] W. D. Wilson and L. G. Haggmark, "Calculations of nuclear stopping, ranges, and straggling in the low-energy region," *Phys. Rev. B*, vol. 15, no. 5, pp. 2458–2468, 1977.

[120] J. Lindhard and A. H. Sorensen, "Relativistic theory of stopping for heavy ions," *Phys. Rev. A - At. Mol. Opt. Phys.*, vol. 53, no. 4, pp. 2443–2456, 1996.

[121] M. Dapor, "Penetration of an electron beam in a solid material: A simple model and a numerical simulation," *Phys. Lett. A*, vol. 143, no. 3, pp. 160–164, 1990.

[122] M. O. El-Ghossain, "Calculations Of Stopping Power, And Range Of Electrons Interaction With Different Material And Human Body Parts," *Int. J. Sci. Technol. Res.*, vol. 6, no. 01, pp. 114–118, 2017.

[123] M. Dapor, "Cross-Sections: Basic Aspect," in *Transport of Energetic Electrons in Solids*, vol. 1, 2017, pp. 9–15.

[124] M. Dapor, "Theory of the interaction between an electron beam and a thin solid film," *Surf. Sci.*, vol. 269–270, no. C, pp. 753–762, 1992.

[125] J. F. Ziegler and R. F. Lever, "Channeling of ions near the silicon 〈001〉 axis," *Appl. Phys. Lett.*, vol. 46, no. 4, pp. 358–360, 1985.

[126] J. F. Ziegler, M. D. Ziegler, and J. P. Biersack, "SRIM - The stopping and range of ions in matter (2010)," *Nucl. Instruments Methods Phys. Res. Sect. B Beam Interact. with Mater. Atoms*, vol. 268, no. 11–12, pp. 1818–1823, 2010.

[127] S. R. Naidoo and J. F. Prins, "Electroluminescence from electron injection junctions created by carbon and phosphorus ion implantation," *Diam. Relat. Mater.*, vol. 8, pp. 1502–1507, 1999.

[128] Y. Zhang, "Electronic stopping power of swift heavy ions in carbon," *Nucl. Instruments Methods Phys. Res. Sect. B Beam Interact. with Mater. Atoms*, vol.

190, no. 1–4, pp. 69–73, 2002.

[129] Y.-H. Song and Y.-N. Wang, “Effects of ion-nucleus sizes on the electronic stopping power for heavy ions in solids,” *Nucl. Instruments Methods Phys. Res. Sect. B Beam Interact. with Mater. Atoms*, vol. 135, no. 1–4, pp. 124–127, 1998.

[130] S. R. Bichsel, H.; Groom, D.E.; Klein, “Passage of Particles Through Matter,” in *Passage of Particles Through Matter*, vol. 1, no. 27, Washington, 2006, pp. 1–34.

[131] R. Singhal *et al.*, “Swift heavy ion induced modifications of optical and microstructural properties of silver-fullerene C60 nanocomposite,” *Nucl. Instruments Methods Phys. Res. Sect. B Beam Interact. with Mater. Atoms*, vol. 267, no. 8–9, pp. 1349–1352, 2009.

[132] P. T. Stroud, “Ion bombardment and implantation and their application to thin films,” *Thin Solid Films*, vol. 11, no. 1, pp. 1–26, 1972.

[133] I. Yaremchuk, A. Tamulevičiene, T. Tamulevičius, K. Šlapikas, Z. Balevičius, and S. Tamulevičius, “Modeling of the plasmonic properties of DLC-Ag nanocomposite films,” *Phys. Status Solidi Appl. Mater. Sci.*, vol. 211, no. 2, pp. 329–335, 2014.

[134] Y. Yang *et al.*, “Tailoring the size and distribution of Ag nanoparticles in silica glass by defects,” *Nucl. Instruments Methods Phys. Res. Sect. B Beam Interact. with Mater. Atoms*, vol. 321, pp. 14–18, 2014.

[135] K. Chopra and I. Kaur, *Thin Film Device Applications*, Second., vol. 1. New York: Plenum, 1983.

[136] X. Li and B. Bhushan, “Measurement of fracture toughness of ultra-thin amorphous carbon films,” *Thin Solid Films*, vol. 315, no. 1–2, pp. 214–221, 1998.

[137] G. Dollinger and R. Kru, “Preparation and investigation of thick carbon foils prepared by laser plasma ablation deposition,” vol. 561, pp. 4–10, 2006.

[138] S. F. Ahmed, M. W. Moon, and K. R. Lee, “Effect of silver doping on optical property of diamond like carbon films,” *Thin Solid Films*, vol. 517, no. 14, pp. 4035–4038, 2009.

[139] A. Ishak, A. N. Muhamad, and M. Rusop, “Optical Properties Of As-Deposited Amorphous Carbon Film Fromvarious Substrate Temperaturesvia Custom-Made-CVD,” *Int. J. Sci. Technol. Res.*, vol. 4, no. 01, pp. 257–269, 2015.

[140] R. Singhal *et al.*, “Electronic excitation induced tuning of surface plasmon resonance of Ag nanoparticles in fullerene C_{70} matrix,” *J. Phys. D. Appl. Phys.*, vol. 42, p. 155103, 2009.

[141] V. Ionescu, C. P. Lungu, M. Osiac, and V. Ciupină, “Silver containing carbon amorphous nanocomposite films deposited by termionic vacuum arc technique,” *Rom. Reports Phys.*, vol. 55, no. 1–2, pp. 119–126, 2010.

[142] V. Michael, “Unsaturated Molecules Containing Main Group Metals,” *Angew. Chemie*, vol. 26, no. 1, pp. 1–14, 1987.

[143] E. Huger and K. Osuch, “Making a noble metal of Pd,” *Eur. Lett.*, vol. 71, no. 2, pp. 276–282, 2005.

[144] S. Fuchs, T. Hahn, and H. Lintz, “The oxidation of carbon monoxide by oxygen over platinum , palladium and rhodium catalysts from 10- ‘” to 1 bar,” vol. 33, pp. 363–369, 1994.

[145] T. R. Jensen, M. D. Malinsky, C. L. Haynes, and R. P. Van Duyne, “Nanosphere Lithography: Tunable Localized Surface Plasmon Resonance Spectra of Silver Nanoparticles,” *J. Phys. Chem. B*, vol. 104, no. 4, pp. 10549–10556, 2000.

[146] S. K. Ghosh and T. Pal, “Interparticle coupling effect on the surface plasmon resonance of gold nanoparticles: From theory to applications,” *Chem. Rev.*, vol. 107, no. 11, pp. 4797–4862, 2007.

[147] L. J. Sherry, S. H. Chang, G. C. Schatz, R. P. Van Duyne, B. J. Wiley, and Y. Xia, “Localized surface plasmon resonance spectroscopy of single silver nanocubes,” *Nano Lett.*, vol. 5, no. 10, pp. 2034–2038, 2005.

[148] L. J. Sherry, R. Jin, C. A. Mirkin, G. C. Schatz, and R. P. Van Duyne, “Localized surface plasmon resonance spectroscopy of single silver triangular nanoprisms,” *Nano Lett.*, vol. 6, no. 9, pp. 2060–2065, 2006.

[149] Y. Gong *et al.*, “Systemically tuning the surface plasmon resonance of high-density silver nanoparticle films,” *Eur. Phys. J. D*, vol. 67, no. 4, p. 87, 2013.

[150] C. Corbella, E. Pascual, G. Oncins, C. Canal, J. L. Andújar, and E. Bertran, “Composition and morphology of metal-containing diamond-like carbon films obtained by reactive magnetron sputtering,” *Thin Solid Films*, vol. 482, no. 1–2, pp. 293–298, 2005.

[151] W. Dai, P. Ke, M. Moon, K. Lee, and A. Wang, “Investigation of the microstructure , mechanical properties and tribological behaviors of Ti-containing diamond-like carbon fi lms fabricated by a hybrid ion beam method,” *Thin Solid Films*, vol. 520, no. 19, pp. 6057–6063, 2012.

[152] H. Dimigen and C. Klages, *Microstructure and wear behavior of metal-containing diamond-like coatings*, vol. 49, no. 1991. Elsevier Sequoia S.A., 2000.

[153] Z. Jun, Z. Hui, W. Zhi-hua, and S. Rui-peng, “Structure and mechanical properties of tungsten-containing hydrogenated diamond like carbon coatings for space applications,” *Phys. Procedia*, vol. 18, pp. 245–250, 2011.

[154] J. C. Orlianges *et al.*, “Electrical properties of pure and metal doped pulsed laser deposited carbon films,” *Thin Solid Films*, vol. 453–454, pp. 291–295, 2004.

[155] R. J. Narayan, “Nanostructured diamondlike carbon thin films for medical applications,” *Mater. Sci. Eng. C*, vol. 25, no. 3, pp. 405–416, 2005.

[156] J. L. Endrino *et al.*, “Structure and properties of silver-containing a-C(H) films deposited by plasma immersion ion implantation,” *Surf. Coatings Technol.*, vol. 202, no. 15, pp. 3675–3682, 2008.

[157] K. Baba *et al.*, “Preparation and antibacterial properties of Ag-containing diamond-like carbon films prepared by a combination of magnetron sputtering and plasma source ion implantation,” *Vacuum*, vol. 89, no. 1, pp. 179–184, 2013.

[158] F. R. Marciano, L. F. Bonetti, L. V. Santos, N. S. Da-Silva, E. J. Corat, and V. J. Trava-Airoldi, “Antibacterial activity of DLC and Ag-DLC films produced by

PECVD technique," *Diam. Relat. Mater.*, vol. 18, no. 5–8, pp. 1010–1014, 2009.

[159] T. Juknius *et al.*, "Antimicrobial properties of diamond-like carbon/silver nanocomposite thin films deposited on textiles: Towards smart bandages," *Materials (Basel).*, vol. 9, no. 5, 2016.

[160] H. W. Choi, R. H. Dauskardt, S. C. Lee, K. R. Lee, and K. H. Oh, "Characteristic of silver doped DLC films on surface properties and protein adsorption," *Diam. Relat. Mater.*, vol. 17, no. 3, pp. 252–257, 2008.

[161] S. Tamulevičius, Š. Meškinis, T. Tamulevičius, and H. G. Rubahn, "Diamond like carbon nanocomposites with embedded metallic nanoparticles," *Reports Prog. Phys.*, vol. 81, no. 2, pp. 1–31, 2018.

[162] J. Krauser, A. K. Nix, H. G. Gehrke, H. Hofsäss, C. Trautmann, and A. Weidinger, "Conductivity enhancement of ion tracks in tetrahedral amorphous carbon by doping with N, B, Cu and Fe," *Nucl. Instruments Methods Phys. Res. Sect. B Beam Interact. with Mater. Atoms*, vol. 272, pp. 280–283, 2012.

[163] H. G. Gehrke, A. K. Nix, H. Hofsäss, J. Krauser, C. Trautmann, and A. Weidinger, "Self-aligned nanostructures created by swift heavy ion irradiation," *J. Appl. Phys.*, vol. 107, no. 9, pp. 1–5, 2010.

[164] J. Krauser *et al.*, "Ion track lithography and graphitic nanowires in diamondlike carbon," *J. Vac. Sci. Technol. B Microelectron. Nanom. Struct.*, vol. 26, no. 6, pp. 2468–2472, 2008.

[165] S. Meškinis *et al.*, "Optical properties of diamond like carbon films containing copper, grown by high power pulsed magnetron sputtering and direct current magnetron sputtering: Structure and composition effects," *Thin Solid Films*, vol. 581, pp. 48–53, 2015.

[166] Š. Meškinis *et al.*, "Annealing Effects on Structure and Optical Properties of Diamond-Like Carbon Films Containing Silver.," *Nanoscale Res. Lett.*, vol. 11, no. 1, pp. 146–154, 2016.

[167] D. Batory, J. Gorzedowski, B. Rajchel, W. Szymanski, and L. Kolodziejczyk, "Silver implanted diamond-like carbon coatings," *Vacuum*, vol. 110, pp. 78–86, 2014.

[168] N. Menegazzo, C. Jin, R. J. Narayan, and B. Mizaikoff, "Compositional and electrochemical characterization of noble metal-diamondlike carbon nanocomposite thin films," *Langmuir*, vol. 23, no. 12, pp. 6812–6818, 2007.

[169] S. Kucherik, A; Kutrovskaya, S; Osipov, A; Skryabin, I; Arakelian Stoletovs, "Metal-carbon nanoclusters for SERS," *IOP Conf. Ser.*, no. 784, pp. 1–6, 2017.

[170] I. Gerhards *et al.*, "Ion beam synthesis of amorphous carbon thin films containing metallic nanoclusters," *Surf. Coatings Technol.*, vol. 158–159, pp. 114–119, 2002.

[171] M. Berova, M. Sandulov, T. Tsvetkova, S. Kitova, L. Bischoff, and R. Boettger, "Ion beam induced surface modification of ta-C thin films," *Acta Phys. Pol. A*, vol. 132, no. 2, pp. 299–301, 2017.

[172] K. Panda, J. J. Hyeok, J. Y. Park, K. J. Sankaran, S. Balakrishnan, and I.-N. Lin, "Nanoscale investigation of enhanced electron field emission for silver ion

implanted/post-annealed ultrananocrystalline diamond films," *Sci. Rep.*, vol. 7, no. 1, pp. 1–14, 2017.

[173] E. Bass, Michael; Li, Guifang; Van Stryland, Ed., *Handbook of Optics: Optical Properties of Materials, Nonlinear Optics, and Quantum Optics*, 1st ed., vol. 4, no. 1. America: MacGraw-Hill, Inc., 1995.

[174] D. Harvey, "Spectroscopic Methods," in *Analytical and Bioanalytical Chemistry*, 2011, pp. 543–666.

[175] P. M. Amirtharaj and D. G. Seiler, "Optical Properties of Semiconductors," in *Handbook of Optics: Optical Properties of Materials, Nonlinear Optics, and Quantum Optics*, 1st ed., E. Bass, Michael; Li, Guifang; Van Stryland, Ed. America: MacGraw-Hill, Inc., 1995, pp. 36.1-36.96.

[176] F. Wooten, *Optical Properties of Solids*. New York: Academic Press, 1972.

[177] M. Fox, "Classification of Optical Processes," in *Optical Properties of Solids*, First., New York: Oxford University press, 2001, pp. 1–58.

[178] A. Bedia *et al.*, "Optical, electrical and structural properties of nano-pyramidal ZnO films grown on glass substrate by spray pyrolysis technique," *Opt. Mater. (Amst).*, vol. 36, no. 7, pp. 1123–1130, 2014.

[179] K. Ayadi and N. Haddaoui, "New approach to the determination of optical constants and thickness of thin dielectric transparent films," *J. Mater. Sci. Mater. Electron.*, vol. 11, no. 2, pp. 163–167, 2000.

[180] X. M. Tian *et al.*, "Nitrogen incorporated diamond-like carbon films by microwave surface wave plasma CVD," *Diam. Relat. Mater.*, vol. 14, no. 11–12, pp. 1839–1842, 2005.

[181] D. P. Manage, "Structural and optical characterization of hydrogenated amorphous carbon thin films," 1998.

[182] J. Robertson and E. O'Reilly, "Electronic and atomic structure of amorphous carbon," *Phys. Rev. B*, vol. 35, no. 6, pp. 2946–2957, 1987.

[183] C. W. Chen and J. Robertson, "Nature of disorder and localization in amorphous carbon," *J. Non. Cryst. Solids*, vol. 227–230, no. PART 1, pp. 602–606, 1998.

[184] I. Alexandrou, A. J. Papworth, C. J. Kiely, G. A. J. Amaratunga, and L. M. Brown, "Calculation of the bandgap and of the type of interband transitions in tetrahedral amorphous carbon using electron energy loss spectroscopy," *Diam. Relat. Mater.*, vol. 13, no. 4–8, pp. 1408–1411, 2004.

[185] A. Tauc, J., Grigorovici, R., Vancu, "Optical properties and electronic structures of amorphous germanium," *Phys. Stat. Sol.*, vol. 15. pp. 627–637, 1966.

[186] Franz Urbach, "The Long-Wavelength Edge of Photographic Sensitivity and of the Electronic Absorption of Solids," *Phys. Rev.*, vol. 92, no. 5, pp. 1324–1324, 1953.

[187] I. Studenyak, M. Kranj, and M. Kurik, "Urbach Rule in Solid State Physics," *Int. J. Opt. Appl.*, vol. 4, no. 3, pp. 76–83, 2014.

[188] A. Shaheen, W. Zia, A. Khalid, and M. S. Anwar, "Band Structure and Electrical Conductivity in Semiconductors," *Mater. Eng.*, pp. 1–26, 2011.

[189] J. A. Duffy, “Chemical bonding in the oxides of the elements: A new appraisal,” *J. Solid State Chem.*, vol. 62, no. 2, pp. 145–157, 1986.

[190] V. Dimitrov and S. Sakka, “Linear and nonlinear optical properties of simple oxides. II,” *J. Appl. Phys.*, vol. 79, no. 3, pp. 1741–1745, 1996.

[191] S. H. Wemple, “Refractive-index behavior of amorphous semiconductors and glasses,” *Phys. Rev. B*, vol. 7, no. 8, pp. 3767–3777, 1973.

[192] S. Reynolds, M. Brinza, M. L. Benkhedir, and G. J. Adriaenssens, “Springer Handbook of Electronic and Photonic Materials,” in *Springer Handbook of Electronic and Photonic Materials*, 2017, pp. 151–174.

[193] S. Kasap, C. Koughia, and H. E. Ruda, “Springer Handbook of Electronic and Photonic Materials,” *Springer Handb. Electron. Photonic Mater.*, pp. 19–45, 2017.

[194] W. Monch, “Springer Handbook of Electronic and Photonic Materials,” *Springer Handb. Electron. Photonic Mater.*, pp. 175–192, 2017.

[195] K. S. Hamdan, S. M. Abdullah, K. Sulaiman, and R. Zakaria, “Effects of silver nanoparticles towards the efficiency of organic solar cells,” *Appl. Phys. A Mater. Sci. Process.*, vol. 115, no. 1, pp. 63–68, 2014.

[196] R. A. Sinton, A. Cuevas, and M. Stuckings, “Cell Material and Device Characterization,” *Time*, pp. 457–460, 1996.

[197] F. H. Alharbi and S. Kais, “Theoretical limits of photovoltaics efficiency and possible improvements by intuitive approaches learned from photosynthesis and quantum coherence,” *Renew. Sustain. Energy Rev.*, vol. 43, pp. 1073–1089, 2015.

[198] W. Shockley and H. J. Queisser, “Detailed balance limit of efficiency of p-n junction solar cells,” *J. Appl. Phys.*, vol. 32, no. 3, pp. 510–519, 1961.

[199] J. Zhao, A. Wang, M. A. Green, and F. Ferrazza, “19.8% Efficient ‘Honeycomb’ Textured Multicrystalline and 24.4% Monocrystalline Silicon Solar Cells,” *Appl. Phys. Lett.*, vol. 73, no. 14, pp. 1991–1993, 1998.

[200] M. Y. Levy and C. Honsberg, “Rapid and precise calculations of energy and particle flux for detailed-balance photovoltaic applications,” *Solid. State. Electron.*, vol. 50, no. 7–8, pp. 1400–1405, 2006.

[201] M. A. Green, “Solar cell fill factors: General graph and empirical expressions,” *Solid State Electron.*, vol. 24, no. 8, pp. 788–789, 1981.

[202] A. W. Blakers, A. Wang, A. M. Milne, J. Zhao, and M. A. Green, “22.8% Efficient Silicon Solar Cell,” *Appl. Phys. Lett.*, vol. 55, no. 13, pp. 1363–1365, 1989.

[203] A. Guechi, M. Chegaar, and M. Aillerie, “Environmental effects on the performance of nanocrystalline silicon solar cells,” *Energy Procedia*, vol. 18, no. 1, pp. 1611–1623, 2012.

[204] Y. Rong, L. Liu, A. Mei, X. Li, and H. Han, “Beyond efficiency: The challenge of stability in mesoscopic perovskite solar cells,” *Adv. Energy Mater.*, vol. 5, no. 20, pp. 1–16, 2015.

[205] E. Elibol, Ö. T. Özmen, N. Tutkun, and O. Köysal, "Outdoor performance analysis of different PV panel types," *Renew. Sustain. Energy Rev.*, vol. 67, pp. 651–661, 2017.

[206] O. Shevaleevskiy, "The future of solar photovoltaics : A new challenge for chemical physics *," vol. 80, no. 10, pp. 2079–2089, 2008.

[207] D. M. Chapin, C. S. Fuller, and G. L. Pearson, "A new silicon p-n junction photocell for converting solar radiation into electrical power [3]," *J. Appl. Phys.*, vol. 25, no. 5, pp. 676–677, 1954.

[208] K. V Rao, H. Van Meer, K. Shim, H. Ito, and T. Henry, "Ion Implant Applications to Enable Advances in Semiconductor Technologies," *Ext. Abs. 17th Int. Work. Junction Technol.*, vol. 8, no. 4, pp. 1–6, 2017.

[209] P. Mahtani, "Optical and Structural Characterization of Amorphous Carbon Films Optical and Structural Characterization of Amorphous Carbon Films," *Spectroscopy*, 2010.

[210] J. A. N. T. Soares, "Introduction to Optical Characterization of Materials," in *Practical Materials Characterization*, 2014, pp. 1–237.

[211] F. Stern, "Elementary Theory of the Optical Properties of Solids," *Solid State Phys.*, vol. 15, pp. 299–408, Jan. 1963.

[212] B. Faust, Ed., "Ultraviolet and visible spectroscopy," in *Modern Chemical Techniques*, vol. 3, no. 1, The Royal Society of Chemistry, 1997, pp. 92–115.

[213] M. Moskovits, "Surface-enhanced Raman spectroscopy: A brief retrospective," *J. Raman Spectrosc.*, vol. 36, no. 6–7, pp. 485–496, 2005.

[214] M. S. Jeong, G. Namkoong, C. C. Byeon, J. S. Kim, and H. S. Lee, "Optical characterization of nanomaterials," *J. Nanomater.*, vol. 1, no. 1, pp. 2–4, 2014.

[215] E. Smith and G. Dent, *Modern Raman Spectroscopy – A Practical Approach*. England: John Wiley & Sons Ltd, 2005.

[216] J. Schwan, S. Ulrich, V. Batori, H. Ehrhardt, and S. R. P. Silva, "Raman spectroscopy on amorphous carbon films," *J. Appl. Phys.*, vol. 80, no. 1, pp. 440–447, 1996.

[217] Princeton Instruments, "Raman Spectroscopy Basics - Application Note," *Internet: http://content. piacton. com/Uploads/Princeton/*, 2012. [Online]. Available: http://content.piacton.com/Uploads/Princeton/Documents/Library/UpdatedLibrary/Raman_Spectroscopy_Basics.pdf.

[218] R. Kalish, A. Reznik, S. Prawer, D. Saada, and J. Adler, "Ion-implantation-induced defects in diamond and their annealing: Experiment and simulation," *Phys. Status Solidi Appl. Res.*, vol. 174, no. 1, pp. 83–99, 1999.

[219] A. G. S. Filho, "Stokes and anti-Stokes Raman spectra of small-diameter isolated carbon nanotubes," *Phys. Rev. B*, vol. 69, pp. 1–8, 2004.

[220] R. Janssen, "Optical spectroscopy techniques," in *Polymer*, 2003, pp. 1–18.

[221] "Theory of Raman Scattering," *http://bwtek.com/raman-theory-of-raman-scattering/*, 2016. .

[222] R. Kalish, C. Uzan-Saguy, B. Philosoph, V. Richter, and S. Prawer, “Loss of electrical conductivity in boron-doped diamond due to ion-induced damage,” *Appl. Phys. Lett.*, vol. 70, no. 8, pp. 999–1001, 1997.

[223] D. W. Hahn, “Raman Scattering Theory,” Florida, 2007.

[224] W. Zhou, R. Apkarian, Z. L. Wang, and D. Joy, “Fundamentals of scanning electron microscopy (SEM),” 2007.

[225] R. Abbaschian, L. Abbaschian, and R. E. Reed-Hill, *Physical Metallurgy Principles*, 4th ed. USA: Cengage Learning, 2009.

[226] J. I. Goldstein *et al.*, *Scanning Electron Microscopy and X-ray Microanalysis*, 3rd ed. New York: Springer Nature, 2003.

[227] T. Aslan, “Electronic Transport Properties of Silicon Nanowires Synthesized By Laser Ablation,” 2015.

[228] E. Thune, T. Cabioc’h, P. Guérin, M. F. Denanot, and M. Jaouen, “Nucleation and growth of carbon onions synthesized by ion-implantation: A transmission electron microscopy study,” *Mater. Lett.*, vol. 54, no. 2–3, pp. 222–228, 2002.

[229] D. Brandon and W. D. Kaplan, *Microstructural characterization of Materials*, Second. England: John Wiley & Sons Ltd, 2008.

[230] J. P. Reithmaier, P. Petkov, W. Kulisch, and C. Popov, “Nanostructured Materials for Advanced Technological Applications,” *Chem. Technol.*, no. January 2009, p. 14, 2009.

[231] J. Mayer and H.-J. Penkalla, “Instrumentation: Transmission Electron Microscopy,” 2007.

[232] Bruker-Nano, “Introduction to EDS analysis - Reference Manual,” Berlin, Germany, 2011.

[233] P. Kuisma-Kursula, “Accuracy, Precision and Detection Limits of SEM-WDS, SEM-EDS and PIXE in the Multi-Elemental Analysis of Medieval Glass,” *X-Ray Spectrom.*, vol. 29, no. 1, pp. 111–118, 2000.

[234] S. J. B. Reed, “Introduction to Energy Dispersive X-ray Spectrometry,” *J. Phys. E.*, vol. 5, no. 997, pp. 1–12, 1972.

[235] R. Jenkins, R. Manne, R. Robin, and C. Senemaud, “IUPAC—nomenclature system for x-ray spectroscopy,” *X-Ray Spectrom.*, vol. 20, no. 3, pp. 149–155, 1991.

[236] B. Hafner, “Energy Dispersive Spectroscopy on the SEM: A Primer,” 2006.

[237] G. Binnig, C. F. Quate, and C. Gerber, “Atomic Force Microscope,” *Phys. Rev. Lett.*, vol. 56, no. 9, pp. 930–933, 1986.

[238] G. Binnig and H. Rohrer, “Scanning Tunneling Microscopy—from Birth to Adolescence (Nobel Lecture),” *Angew. Chemie Int. Ed. English*, vol. 26, no. 7, pp. 606–614, 1987.

[239] N. A. Burnham, F. Cruceanu, Q. Dong, and N. P. Thompson, “An Introduction to Atomic Force Microscopy,” no. October. p. 2280, 2002.

[240] G. Binnig and H. Rohrer, “Scanning tunneling microscopy Scanning tunneling microscopy,” *Helv. Phys. Acta*, vol. 55, no. 6, pp. 726–735, 1982.

[241] “Atomic Force Microscopy: General principle,” *http://virtual.itg.uiuc.edu/training/AFM_tutorial/*, 2008. [Online]. Available: http://virtual.itg.uiuc.edu/training/AFM_tutorial/. [Accessed: 11-Dec-2018].

[242] O.-G. Simionescu, C. Romaniţan, O. Tutunaru, V. Ion, O. Buiu, and A. Avram, “RF Magnetron Sputtering Deposition of TiO2 Thin Films in a Small Continuous Oxygen Flow Rate,” *Coatings*, vol. 9, no. 7, p. 442, 2019.

[243] S. B. Hashim, N. H. Mahzan, S. H. Herman, and M. Rusop, “Room-temperature deposition of silicon thin films by RF magnetron sputtering,” *Adv. Mater. Res.*, vol. 576, no. December 2014, pp. 543–547, 2012.

[244] J. W. Hoon, K. Y. Chan, J. Krishnasamy, T. Y. Tou, and D. Knipp, “Direct current magnetron sputter-deposited ZnO thin films,” *Appl. Surf. Sci.*, vol. 257, no. 7, pp. 2508–2515, 2011.

[245] A. Vecchione, S. Pace, and A. Nigro, “Sputtering Technique,” 2017.

[246] K. B. Sundaram and A. Khan, “Characterization and optimization of zinc oxide films by r.f. magnetron sputtering,” *Thin Solid Films*, vol. 295, no. 1–2, pp. 87–91, 1997.

[247] S. Prawer and R. Kalish, “Ion-beam-induced transformation of diamond,” *Phys. Rev. B*, vol. 51, no. 22, pp. 15711–15722, 1995.

[248] F. Tuinstra and J. L. Koenig, “Raman Spectrum of Graphite,” *J. Chem. Phys.*, vol. 153, no. 3, pp. 1126–1130, 1970.

[249] R. J. Nemanich and S. A. Solin, “First- and second-order Raman scattering from finite-size crystals of graphite,” *Phys. Rev. B*, vol. 20, no. 2, pp. 392–401, 1979.

[250] M. Constantinou *et al.*, “Metal (Ag/Ti)-Containing Hydrogenated Amorphous Carbon Nanocomposite Films with Enhanced Nanoscratch Resistance: Hybrid PECVD/PVD System and Microstructural Characteristics,” *Nanomaterials*, vol. 8, no. 4, p. 209, 2018.

[251] R. J. Nemanich and S. A. Solin, “Observation of an anomolously sharp feature in the 2nd order Raman spectrum of graphite,” *Solid State Commun.*, vol. 23, no. 7, pp. 417–420, 1977.

[252] Y. Wang, D. C. Alsmeyer, and R. L. Mccreery, “Raman spectroscopic characterization of some commercially available carbon black materials,” *Carbon N. Y.*, no. 10, pp. 557–563, 1990.

[253] A. C. Ferrari and J. Robertson, “Raman spectroscopy of amorphous, nanostructured, diamond-like carbon, and nanodiamond,” *Philos. Trans. R. Soc. A Math. Phys. Eng. Sci.*, vol. 362, no. 1824, pp. 2477–2512, 2004.

[254] V. Paillard, “On the origin of the 1100cm-1 Raman band in amorphous and nanocrystalline sp3 carbon,” *Europhys. Lett.*, vol. 54, no. 2, pp. 194–198, 2001.

[255] B. Dischler, A. Bubenzer, and P. Koidl, “Hard carbon coatings with low optical absorption,” *Appl. Phys. Lett.*, vol. 42, no. 8, pp. 636–638, 1983.

[256] A. C. Ferrari and J. Robertson, “Interpretation of Raman spectra of disordered and amorphous carbon,” *Phys. Rev. B*, vol. 61, no. 20, pp. 14095–14107, 2000.

[257] Y. Wu, J. Chen, H. Li, L. Ji, Y. Ye, and H. Zhou, “Preparation and properties of

Ag/DLC nanocomposite films fabricated by unbalanced magnetron sputtering," *Appl. Surf. Sci.*, vol. 284, pp. 165–170, 2013.

[258] M. J. Mathews, M. A. Pimenta, G. Dresselhaus, M. S. Dresselhaus, and M. Endo, "Origin of dispersive effects of the raman d band in carbon materials," *Phys. Rev. B - Condens. Matter Mater. Phys.*, vol. 59, no. 10, pp. R6585–R6588, 1999.

[259] A. C. Ferrari and J. Robertson, "Resonant Raman spectroscopy of disordered, amorphous, and diamondlike carbon," *Phys. Rev. B - Condens. Matter Mater. Phys.*, vol. 64, no. 7, pp. 1–13, 2001.

[260] Š. Meškinis *et al.*, "Structure of the silver containing diamond like carbon films: Study by multiwavelength Raman spectroscopy and XRD," *Diam. Relat. Mater.*, vol. 40, pp. 32–37, 2013.

[261] M. A. Tamor and W. C. Vassell, "Raman 'fingerprinting' of amorphous carbon films," *J. Appl. Phys.*, vol. 76, no. 6, pp. 3823–3830, 1994.

[262] N. R. C. Raju, K. J. Kumar, and A. Subrahmanyam, "Silver oxide (AgO) thin films for Surface Enhanced Raman Scattering (SERS) studies," *AIP Conf. Proc.*, vol. 1267, no. February, pp. 1005–1006, 2010.

[263] A. Débarre, R. Jaffiol, C. Julien, P. Tchénio, and M. Mostafavi, "Raman scattering from single Ag aggregates in presence of EDTA," *Chem. Phys. Lett.*, vol. 386, no. 4–6, pp. 244–247, 2004.

[264] P. Sharma *et al.*, "Effect of Ag Ion Implantation on SPR of Cu-C<inf>60</inf>Nanocomposite Thin Film," *Plasmonics*, vol. 13, no. 1, pp. 669–679, 2017.

[265] K. K. Nanda, A. Maisels, F. E. Kruis, H. Fissan, and S. Stappert, "Higher Surface Energy of Free Nanoparticles," *Phys. Rev. Lett.*, vol. 91, no. 10, pp. 1–4, 2003.

[266] H. M. Lu and Q. Jiang, "Size-Dependent Surface Energies of Nanocrystals," *J. Phys. Chem. B*, vol. 108, no. 18, pp. 5617–5619, 2004.

[267] B. Medasani, Y. H. Park, and I. Vasiliev, "Theoretical study of the surface energy, stress, and lattice contraction of silver nanoparticles," *Phys. Rev. B - Condens. Matter Mater. Phys.*, vol. 75, no. 23, 2007.

[268] D. Vollath, F. D. Fischer, and D. Holec, "Surface energy of nanoparticles - influence of particle size and structure," *Beilstein J. Nanotechnol.*, vol. 9, no. 1, pp. 2265–2276, 2018.

[269] A. Ismaila, P. O. Akusu, and T. O. Ahmed, "Structural and Optical Properties of Polymer Blend Nanocomposites Based on Poly (vinyl acetate-co- vinyl alcohol)/ TiO 2 Nanoparticles," *Phys. Sci. Int. J.*, vol. 7, no. 4, pp. 252–261, 2015.

[270] K.-C. Lee, S.-J. Lin, C.-H. Lin, C.-S. Tsai, and Y.-J. Lu, "Size effect of Ag nanoparticles on surface plasmon resonance," *Surf. Coatings Technol.*, vol. 202, no. 22–23, pp. 5339–5342, 2008.

[271] C. Noguez, "Surface plasmons on metal nanoparticles: The influence of shape and physical environment," *J. Phys. Chem. C*, vol. 111, no. 10, pp. 3606–3619, 2007.

[272] R. B. McLellan, "The Solubility of Carbon in Soild Gold, Copper, and Silver," *Scr. Metall.*, vol. 3, no. 1, pp. 389–391, 1969.

[273] S. Eustis and M. A. El-Sayed, "Why gold nanoparticles are more precious than pretty gold: Noble metal surface plasmon resonance and its enhancement of the radiative and nonradiative properties of nanocrystals of different shapes," *Chem. Soc. Rev.*, vol. 35, no. 3, pp. 209–217, 2006.

[274] A. Slistan-Grijalva, R. Herrera-Urbina, J. F. Rivas-Silva, M. Ávalos-Borja, F. F. Castillón-Barraza, and A. Posada-Amarillas, "Classical theoretical characterization of the surface plasmon absorption band for silver spherical nanoparticles suspended in water and ethylene glycol," *Phys. E Low-Dimensional Syst. Nanostructures*, vol. 27, no. 1–2, pp. 104–112, 2005.

[275] A. L. González and C. Noguez, "Influence of Morphology on the Optical Properties of Metal Nanoparticles," *J. Comput. Theor. Nanosci.*, vol. 4, no. 7–8, pp. 1249–1252, 2007.

[276] W. W. Duley, "Refractive Indices for Amorphous Carbon," *Astrophys. J.*, vol. 287, pp. 694–696, 1984.

[277] A. Kaphle and P. Hari, "Variation of index of refraction in cobalt doped ZnO nanostructures," *J. Appl. Phys.*, vol. 122, no. 16, 2017.

[278] K. J. Kim and Y. R. Park, "Spectroscopic ellipsometry study of optical transitions in Zn 1-xCoxO alloys," *Appl. Phys. Lett.*, vol. 81, no. 8, pp. 1420–1422, 2002.

[279] S. F. Ahmed, M. W. Moon, and K. R. Lee, "Enhancement of electron field emission property with silver incorporation into diamondlike carbon matrix," *Appl. Phys. Lett.*, vol. 92, no. 19, pp. 1–4, 2008.

[280] P. Patsalas, "Optical properties of amorphous carbons and their applications and perspectives in photonics," *Thin Solid Films*, vol. 519, no. 12, pp. 3990–3996, 2011.

[281] N. Laidani *et al.*, "Optical absorption parameters of amorphous carbon films from Forouhi – Bloomer and Tauc – Lorentz models : a comparative study To cite this version : HAL Id : hal-00434409," *J. Phys. Condens. Matter*, vol. 20, no. 1, pp. 015216.1-015216.8, 2009.

[282] L. L. Jensen and L. Jensen, "Electrostatic interaction model for the calculation of the polarizability of large noble metal nanoclusters," *J. Phys. Chem. C*, vol. 112, no. 40, pp. 15697–15703, 2008.

[283] M. Pereiro and D. Baldomir, "Structure of small silver clusters and static response to an external electric field," *Phys. Rev. A - At. Mol. Opt. Phys.*, vol. 75, no. 3, 2007.

[284] Y. A. Yamusa, R. Hussin, and W. N. W. Shamsuri, "Effect of Dy3+ on the physical, optical and radiative properties of CaSO4–B2O3–P2O5 glasses," *Indian J. Phys.*, vol. 93, no. January, pp. 15–26, 2018.

[285] K. Lim, M. A. A. Hamid, R. Shamsudin, N. H. Al-Hardan, I. Mansor, and W. Chiu, "Temperature-driven structural and morphological evolution of zinc oxide nano-coalesced microstructures and its defect-related photoluminescence properties," *Materials (Basel).*, vol. 9, no. 4, 2016.

[286] K. B. K. Teo *et al.*, "Highest optical gap tetrahedral amorphous carbon (vol 11, pg 1086, 2002)," *Diam. Relat. Mater.*, vol. 11, no. 8, pp. 1086–1090, 2002.